Development of a Gamow No-Core Shell-Model Framework for Nuclear Resonances

Vom Fachbereich Physik

der Technischen Universität Darmstadt

zur Erlangung des Grades

Doctor rerum naturalium (Dr. rer. nat.)

genehmigte Dissertation von

Julius Müller, M.Sc.

aus Langen (Hessen)

Referent: Prof. Dr. Robert Roth

Korreferent: Prof. Dr. Hans-Werner Hammer

Darmstadt 2023

Development of a Gamow No-Core Shell-Model Framework for Nuclear Resonances
Entwicklung eines Gamow No-Core Schalenmodell Frameworks für Kernresonanzen

Genehmigte Dissertation von Julius Müller, geboren in Langen (Hessen)
Darmstadt, Technische Universität Darmstadt

Referent: Prof. Dr. Robert Roth
Korreferent: Prof. Dr. Hans-Werner Hammer

Tag der Einreichung: 24.01.2023
Tag der Prüfung: 15.02.2023

ABSTRACT

The development of sophisticated *ab initio* methods and the improvement of nuclear inter-actions derived from chiral effective field theory allow a very precise description of nuclear bound-state observables. In recent years, the development of *ab initio* methods that include the continuum degrees of freedom have made significant progress. Those methods allow the description of nuclear resonances.

In this work, we develop an *ab initio* Gamow no-core shell model (GNCSM) framework for the description of nuclear resonances. The GNCSM is an extension of the NCSM, which is a very common *ab initio* method for a precise calculation of bound-state observables. The GNCSM makes use of the Berggren completeness relation, which enables the use of single-particle resonance and scattering continuum states in an orthonormal single-particle basis. As a consequence, the GNCSM Hamilton matrix becomes complex symmetric. The complex eigenvalues are able to describe the decay rate of nuclear resonances. The matrix elements for the GNCSM are calculated using an expansion in harmonic-oscillator matrix elements in order to regulate the infinite single-particle continuum states.

The GNCSM with the Berggren single-particle basis is used to calculate a reference state. For this reference state, we compute a set of optimized Gamow natural orbitals in order to enhance the convergence rate in a subsequent GNCSM calculation. Finally, multiple Gamow natural orbital sets are used to compute a final result with a many-body uncertainty.

The GNCSM framework is applied to resonances of various light nuclei. For some of these nuclei, we present a more precise calculation than the current spread of experimental results. Furthermore, we investigate different realistic interactions derived from chiral effective field theory with respect to their influence on the resonance energy and find that the dependence on the interaction is negligible compared to the many-body uncertainty of our framework. As a final application, we study the tetraneutron and find indications for a low-lying resonance.

ZUSAMMENFASSUNG

Die Entwicklung fortgeschrittener *ab initio* Methoden und die Verbesserung der Wechselwirkung zwischen Nukleonen, die mithilfe der chiralen effektiven Feldtheorie bestimmt wird, hat eine präzise Beschreibung von Observablen von gebundenen Kernzuständen ermöglicht. In den letzten Jahren ist auch die Entwicklung von *ab initio* Methoden, die das Kontinuum mit in Betracht ziehen, signifikant fortgeschritten. Mithilfe dieser Methoden ist es möglich Resonanzzustände in Kernen zu beschreiben.

In dieser Arbeit entwickeln wir ein Gamow No-Core Schalenmodell (GNCSM) Framework für die Beschreibung von Resonanzzuständen. Das GNCSM ist eine Erweiterung des NCSM, welches eine verbreitete *ab initio* Methode zur präzisen Berechnung von Observablen von gebundenen Kernzuständen ist. Dazu nutzt das GNCSM eine von Berggren bewiesene Vollständigkeitsrelation, die es ermöglicht aus Streuzuständen und Resonanzen von Einteilchensystemen eine orthonormale Einteilchenbasis zu erzeugen. Eine Folge dieser Einteilchenbasis ist, dass die Hamiltonmatrix in der Vielteilchenbasis komplex wird. Die resultierenden komplexen Eigenwerte beschreiben die Zerfallszeit von Resonanzzuständen. Um die Hamiltonmatrixelemente zu berechnen, werden die Resonanzen und Streuzustände der Einteilchenbasis in harmonischen Oszillatorfunktionen entwickelt, welche die unendliche Reichweite dieser Kontinuumszustände einschränken.

Der Resonanzzustand aus der GNCSM-Rechnung mit der Berggren-Einteilchenbasis wird als Referenzzustand für die Bestimmung einer optimierten Einteilchenbasis, den natürlichen Orbitalen, verwendet. Diese natürlichen Orbitale beschleunigen die Konvergenz in einer zweiten GNCSM-Rechnung. Diese GNCSM-Rechnung wird für die natürlichen Orbitale von mehreren Referenzzuständen durchgeführt und daraus ein finales Ergebnis mit einer Unsicherheit der Vielteilchenrechnung bestimmt.

Das GNCSM Framework wird für die Berechnung von Resonanzenergien von verschiedenen

leichten Kernen verwendet. Für einige dieser Kerne sind die experimentellen Ergebnisse nicht eindeutig, sodass die Unsicherheiten unserer Rechnung kleiner als die Streuung der experimentellen Ergebnisse ist. In einer weiteren Anwendung untersuchen wir den Einfluss von verschiedenen nuklearen Wechselwirkungen aus der chiralen effektiven Feldtheorie auf die Resonanzenergie eines Kernzustands. Dabei stellt sich heraus, dass die Abhängigkeit der Wechselwirkung im Vergleich zur Ungenauigkeit der Vielteilchenrechnung vernachlässigbar ist. Als finale Anwendung untersuchen wir das Tetraneutron und finden Anzeichen für einen Resonanzzustand bei niedrigen Energien.

CONTENTS

INTRODUCTION

The theory of quantum mechanics emerged at the beginning of the twentieth century and provides the foundation for many of today's physical fields, including nuclear physics. The solution of the quantum many-body problem, i.e., the stationary Schrödinger equation, is one of the main tasks of nuclear structure and reaction theory. As the name already states, nuclear structure theory aims at a fundamental understanding of the structure of the inner most part of an atom, the nucleus. This includes the calculation of binding energies, radii, and electromagnetic observables. Complementary, nuclear reaction theory describes reaction and decay mechanisms. The impact of nuclear structure theory exceeds the microscopic region by far and is also important in astrophysics [HWS21; Nun+20; Gre+20; HK17b].

At the end of the lifecycle of a star, it can explode in a supernova [BV21; Kur+22]. The remnant of such a supernova can be a neutron star, an extremely dense object consisting mostly of neutrons [LP01; Man20]. A system of gravitationally bound neutrons is impossible to create in a laboratory and we rely on correct microscopical theoretical description of neutron matter in order to draw conclusions on the equations of state for a neutron star.

The microscopic description of the interaction between the multi-neutron system inside a neutron star, is part of current research in nuclear structure theory [IÁA19; Due+22; Fos+17; Li+19]. The aforementioned quantum many-body problem is key to achieve this goal. It consists of two main ingredients, a nuclear Hamiltonian and a many-body method to solve the many-body problem.

The derivation of a nuclear Hamiltonian is a very complicated procedure. The interaction between nucleons is governed by a residual force of the quarks and gluons inside the nucleons, which interact via the strong and electromagnetic force. After the nuclear interactions

were constructed phenomenologically for many decades in the past [Mac01; VP11; Pie+01], the development of the effective field theories based on the theory of quantum chromodynamics allowed a more fundamental derivation of the nuclear Hamiltonian [EM03; ME11; Epe+19; Eks+15]. Nuclear interactions are called realistic if they are fitted to nucleon-nucleon scattering data at high precision, typically up to energies of ~ 350 MeV [BNV13].

The second ingredient of the quantum many-body problem is a many-body method that solves the Schrödinger equation. Before we jump into details of different many-body methods, we want to define the term *ab initio*, which translates literally to "from the beginning". We define *ab initio* as the solution of the quantum many-body problem [Nav+16]

I. ... for a realistic nuclear Hamiltonian.

II. ... without any uncontrolled approximation.

III. ... with a quantifiable uncertainty.

We are interested in an *ab initio* description of the spectrum of bound states as well as resonance and scattering states in the low-energy continuum. Especially, the inclusion of the continuum proves to be a very challenging task in the development of *ab initio* methods for the complete energy spectrum.

The development of *ab initio* methods for discrete bound states has been very successful in the past twenty years. In particular, the availability of modern high-performance computers has allowed the application of a multitude of different methods. Some of the most common *ab initio* methods for bound states are the no-core shell model (NCSM) [BNV13; Rot09], the Faddeev-Yakubovsky equations [LHL88; LC20], the coupled cluster (CC) method [DH04], the in-medium similarity renormalization group (IM-SRG)[Her+13; GCR16; Her17] and the Green's function Monte Carlo method [CBN13]. These methods allow precise *ab initio* calculations of bound state observables over a large range of light and medium-mass nuclei. However, the inclusion of the quantum mechanical continuum poses a huge problem for these methods, such that they are only able to extrapolate from the discrete bound-state spectrum towards the continuum [Pie03; LC05].

The inclusion of the continuum enables non-stationary, time-dependent nuclear states, i.e., resonance states or scattering states. The quantum many-body problem including continuum states can be solved using the time-dependent Schrödinger equation [Vol09; OHS14]. Alternatively, we can still use the time-independent, stationary Schrödinger equation for a complex symmetric Hamiltonian, where the imaginary part of the energy parametrizes

the decay time of a resonance. The extension towards the continuum has successfully been applied to the NCSM, e.g., NCSM with resonating group method [QN08; QN09], NCSM with continuum [BNQ13a; BNQ13b], the single-state harmonic oscillator representation of scattering equations [Shi+16b; Shi+16a], and the Gamow NCSM (GNCSM) [Pap+13; Fos+17; Li+19; Li+21].

In this work, we develop a GNCSM framework for the calculation of nuclear resonance states. In this approach, we include the continuum degrees of freedom at the level of the single-particle basis, the so called Berggren basis [Ber68; Lin93]. Berggren was able to prove that it is possible to normalize single-particle resonance states in the continuum, which enables the derivation of an orthonormal single-particle basis. Since all the information of the continuum is already included at the level of the single-particle basis, it can be used in all calculations that are based on a single-particle basis, e.g. the GNCSM [Fos+17; Li+19; Li+21], the Gamow IM-SRG [Hu+19] or the Gamow CC [Hag+07].

Formally, the use of the Berggren basis in the GNCSM only affects the standard NCSM approach for bound states at a few steps. The use of the Berggren single-particle basis results in a complex Hamilton matrix in the GNCSM. Thus, the solution of the complex eigenvalue problem becomes computationally more demanding. In order to minimize the many-body model space dimension, we optimize the Berggren single-particle basis throughout the calculations using a set of Gamow natural orbitals. Natural orbitals (NAT) were already used successfully in the GNCSM [Fos+17; Li+19] and bound-state methods, e.g., the NAT-NCSM [TMR19], the NAT-IM-SRG [Vob20; Hop+21], and the NAT-CC [Nov+20].

This work is structured in three main parts. In part I, we introduce the basics necessary to build and apply the GNCSM framework. We start with the setup of the nuclear Hamiltonian in chapter 1, which includes an introduction to realistic interactions derived from chiral effective field theory. Chapter 2 introduces the NCSM for bound states, which presents the foundation for the development of the GNCSM. The definition and computation of the single-particle Berggren basis, which includes the continuum information, is done in chapters 3 and 4, respectively.

Afterwards, we move on towards the development of the GNCSM framework in part II. The complete single-particle basis is computed in chapter 5 and the necessary matrix elements for the calculation of the Hamilton matrix for the GNCSM are calculated in chapter 6. Finally, we are able to perform and investigate the first GNCSM calculations in chapter 7. In order to optimize our calculations we calculate a set of Gamow natural orbitals and use them for a second GNCSM calculation for our final results in chapter 8.

The final part III contains the first applications of our GNCSM framework. We start our calculations for a set of light nuclei, which have a ground or excited-state resonance, in chapter 9. Afterwards, we analyze a set of realistic nuclear interactions, which are derived from chiral effective field theory, in chapter 10. As a final application, we investigate the tetra-neutron, which has gained increased interest after the very recent detection of a correlated four-neutron system [Due+22], in chapter 11.

PART I.

BASICS

1

NUCLEAR HAMILTONIAN

The main goal in nuclear structure theory is to solve the time-independent many-body Schrödinger equation

$$\hat{H}|\Psi_n\rangle = E_n|\Psi_n\rangle \tag{1.1}$$

with the nuclear Hamiltonian $\hat{H}$, the eigenstates $|\Psi_n\rangle$ and the eigenvalues E_n. In order to solve this many-body problem we need to define a nuclear Hamiltonian and construct a many-body method. The latter will be discussed in the chapter 2. In this chapter, we will focus on the definition and construction of the translationally invariant intrinsic nuclear Hamiltonian [HR09]

$$\hat{H}_{\text{int}} = \hat{T}_{\text{int}} + \hat{V} \tag{1.2}$$

with the intrinsic kinetic energy $\hat{T}_{\text{int}}$ and an intrinsic nuclear interaction $\hat{V}$.

For the intrinsic kinetic energy operator we use the following two representations later on [HR09]

$$\hat{T}_{\text{int}} = \hat{T} - \hat{T}_{\text{cm}} = \frac{1}{2A}\sum_{i<j}\frac{\left(\hat{\mathbf{p}}_i - \hat{\mathbf{p}}_j\right)^2}{m_{\text{N}}} \tag{1.3}$$

$$= \left(1 - \frac{1}{A}\right)\sum_i\frac{\hat{\mathbf{p}}_i^2}{2m_{\text{N}}} - \frac{1}{2Am_{\text{N}}}\sum_{i<j}\hat{\mathbf{p}}_i \cdot \hat{\mathbf{p}}_j \tag{1.4}$$

with the single-particle kinetic energy operator $\hat{\mathbf{p}}$, the mean nucleon mass m_{N} and the particle

number A. The first representation consists of a pure two-body operator whereas the second representation is a sum of a one-body and a two-body operator.

The derivation of the nuclear interaction $\hat{V}$ is more complicated and a major part of current research [EMN17; Hüt+20; Mar+21]. The complications originate from the fact that the building blocks of nucleons are quarks and gluons and their interaction is characterized by the theory of quantum chromodynamics (QCD). Because of the asymptotic freedom of the QCD coupling strength, it is not possible to treat the QCD interaction perturbatively in the low-energy regime of nuclear physics. As a workaround, one uses that quarks and gluons are confined in hadrons and builds a residual interaction of quarks and gluons in order to describe the interaction between nucleons. One type of nuclear interactions are phenomenological or empirical interactions. Prominent representatives for phenomenological interactions are the Argonne V18 [WSS95; VP11] and the CD-Bonn [Mac01] nucleon-nucleon interactions as well as the Illinois three-nucleon interactions [Pie+01]. A more fundamental and systematic way to define a nuclear interaction is to formulate an effective field theory (EFT) of the underlying fundamental theory of QCD. The most popular EFT in nuclear structure physics is the chiral EFT (χEFT) [EM03; ME11; EMN17].

1.1. Chiral Effective Field Theory

The goal of χEFT is to build an effective theory with nucleons and pions as effective degrees of freedom based on QCD. The underlying quark-gluon structure of nucleons and pions cannot be resolved in the energy regime of nuclear structure theory. The range of the nuclear energy regime is characterized in multiple ways and we only mention some of them here [EHM09]. From empirical interactions we know that the long-range part of the nuclear interaction is characterized by the one-pion exchange which corresponds to energies at the order of the pion mass $\sim 140\,\mathrm{MeV}$. Second, we know that the binding energy per nucleon is much smaller than the pion mass at the order of (1 to 8) MeV. Schematically speaking, the χEFT zooms out of the short-distance microphysics of the fundamental quark-gluon interaction of QCD. Compared to phenomenological interactions this approach preserves the symmetries and constrains of the underlying theory of QCD. From a practitioners view, the χEFT has two important characteristics. First, it includes many-body forces systematically and, second, it arranges different contributions to the interaction by their importance. In the context of *ab initio* this means, that it is possible to systematically improve the interaction order by order by including more terms to the interaction. Since we expect the orders to become less important

in a perturbative sense, this allows to estimate an uncertainty for the residual contribution to the interaction. We will discuss the power counting scheme and different families of chiral interactions in more detail in chapter 10. For a formal insight and an in-depth derivation of interactions from χEFT we refer the reader to [ME11; HK17a].

1.2. Similarity Renormalization Group

The nuclear interaction has a strong short-range repulsion which is also described as short-range correlations and it has a strong tensor-force contribution [BFP07]. As a consequence it generates many-body wave functions that are highly correlated. In the subsequent many-body method this results in large model spaces needed in order to obtain converged results (see chapter 2).

The similarity renormalization group (SRG) approach aims to enhance the convergence speed in subsequent many-body calculations by pre-diagonalizing the nuclear Hamiltonian [BFP07; Fur12; RRH08]. Formally, the SRG transformation is a continuous unitary transformation

$$\hat{H}_\alpha = \hat{U}_\alpha^\dagger \hat{H}_0 \hat{U}_\alpha \tag{1.5}$$

with the evolved Hamiltonian $\hat{H}_\alpha$, the unitary transformation operator $\hat{U}_\alpha$ and the flow parameter α. As boundary conditions, we use the initial or bare interaction $\hat{H}_0$ and $\hat{U}_0 = \hat{U}_0^\dagger = \mathbb{1}$ for $\alpha = 0$. Calculating the derivative with respect to α yields the flow equation

$$\frac{d}{d\alpha}\hat{H}_\alpha = [\hat{\eta}_\alpha, \hat{H}_\alpha], \tag{1.6}$$

with the generator $\hat{\eta}_\alpha$

$$\hat{\eta}_\alpha = \left(\frac{d}{d\alpha}\hat{U}_\alpha\right)\hat{U}_\alpha^\dagger = -\hat{\eta}_\alpha^\dagger. \tag{1.7}$$

The choice of the generator will determine the behavior of the flow equation. A common choice for the generator is

$$\hat{\eta}_\alpha = m_{\mathrm{N}}^2 [\hat{T}_{\mathrm{int}}, \hat{H}_\alpha] \tag{1.8}$$

with the mean nucleon mass m_{N}. This generator pre-diagonalizes the Hamiltonian $\hat{H}_\alpha$ in the momentum-space representation.

Figure 1.1 shows the matrix representation of an NN interaction in momentum space for the initial Hamiltonian and a SRG evolved Hamiltonian. During the transformation the
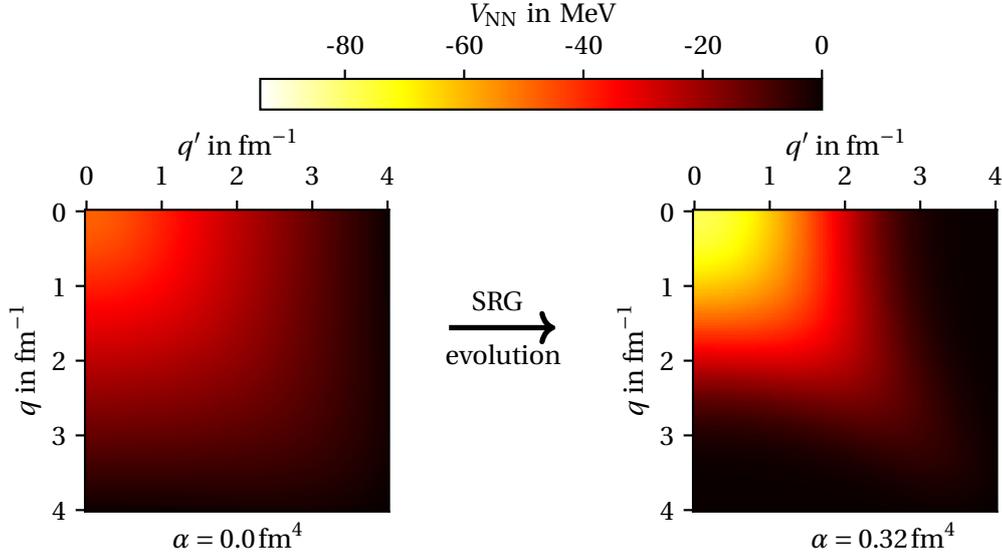
FIGURE 1.1.: Matrix representation of the $^3S_1$ channel of the deuteron partial wave for the bare interaction with $\alpha = 0.0\,\text{fm}^4$ (left) and the SRG evolved interaction for $\alpha = 0.32\,\text{fm}^4$ (right). The SRG evolution is performed in momentum-space representation with relative momenta q and q'. The used interaction is the chiral interaction by Entem, Machleidt and Nosyk at N^{3}LO with a cutoff of $\Lambda = 500\,\text{MeV}$ [EMN17].

off-diagonal matrix elements are suppressed. The kinetic energy stays unchanged throughout the SRG evolution, since it commutes with the generator.

A downside of the SRG evolution are so called induced many-body forces. During the SRG evolution of the Hamiltonian the commutator relation in the flow equation produces contributions of higher particle ranks to the interaction. This can already be seen from the first step $\Delta\alpha$ in the evolution of the flow equation for an initial two-body Hamiltonian

$$\hat{H}_{\Delta\alpha} = \hat{H}_0 + \Delta\alpha \; m_{\text{N}}^2 \big[\big[\hat{T}_{\text{int}}, \hat{H}_0\big], \hat{H}_0\big]. \tag{1.9}$$

The expansion of the commutator contains products of two-body operators which results in higher rank forces. The impact of the induced many-body forces becomes larger for larger flow parameters α. Depending on the application we only use the NN or NN+3N forces in the final interaction and neglect the induced many-body forces with a higher particle rank. This results in an error to the many-body calculation which is traded off for the enhanced convergence speed.

2

NO-CORE SHELL MODEL

The no-core shell model (NCSM) has proven to be a very powerful *ab initio* method in nuclear structure theory [BNV13; Var+09; Nav+09]. In the standard formulation, it is able to calculate numerically exact eigenvalues and eigenvectors of the time-independent Schrödinger equation for bound states of light nuclei in an *ab initio* manner. This means we can use realistic interactions and obtain results with a controlled approximation that allows us to quantify a theoretical uncertainty [Knö+23]. However, the standard NCSM has two limitations. Firstly, the model space dimension grows factorially with the nuclear mass number, setting a computational limit to light nuclei. Secondly, the NCSM is limited to the description of bound states.

In the past decade, there have been different approaches that either optimize the NCSM or combine it with other known many-body methods to build so called hybrid methods in order to partially remedy the limitations. Table 2.1 shows an overview of existing extensions to the NCSM. We will start with a short introduction to methods that extend the NCSM to heavier nuclei, and afterwards focus on the extensions towards many-body resonance and scattering states.

On the side of the extensions towards heavier nuclei, the NCSM with natural orbitals (NAT-NCSM)[TMR19; Con+17; Con17] uses an optimized single-particle basis in order to enhance the convergence speed of the NCSM calculations. An optimization of the many-body model space is achieved by the so called importance-truncated NCSM (IT-NCSM)[Rot09] that uses

	extension beyond light nuclei	extension beyond bound states
basis optimization	NAT-NCSM IT-NCSM	GNCSM
hybrid methods	NCSM-PT IM-NCSM	NCSM/RGM NCSMC

TABLE 2.1.: Classification of NCSM extensions and the respective limitation it lifts. For further information see the text.

an *a priori* estimate for the importance of the many-body basis states. This allows for a restriction of the model space to the most relevant many-body basis states. Since these two optimizations act on separate parts of the method they can be used simultaneously. Considering hybrid methods, we can combine the NCSM with other many-body methods in order to overcome most of their individual restrictions and retain most of their advantages. One of these hybrid methods is the perturbatively-improved NCSM (NCSM-PT)[Tic+18], which combines the advantage of highly correlated eigenstates from the NCSM with the perturbative corrections for very large model spaces. Another method is the in-medium NCSM (IM-NCSM)[Geb+17], which combines the multi-reference in-medium similarity renormalization group with the NCSM.

On the side of hybrid methods extending the NCSM towards resonance and scattering states, the NCSM with the resonating group method (NCSM/RGM) is able to describe the scattering of a binary cluster system [QN08; QN09; NRQ10]. The eigenstates of the clusters are calculated using the NCSM, whereas the relative motion of the two clusters with particle numbers a and $(A - a)$ is described within the RGM. This approach has been successfully applied to nucleon-nucleus scattering, especially if the nucleus is well bound and only a few NCSM eigenstates are needed to obtain converged results. This hints at the problems of the NCSM/RGM if one or even both of the binary clusters are weakly bound and there exist a lot of coupled channels in the reaction which cannot be described by a two cluster system but rather by an A-body nucleus. This functionality was added in the so called NCSM with continuum (NCSMC), which includes eigenstates of the A-body system in addition to the binary cluster states [BNQ13a; BNQ13b; Lan14]. This method has successfully been applied

to weakly bound nucleon-nucleus scattering, e.g., n-^{6}He and n-^{8}Be scattering.

In this thesis, we access many-body resonance states by using an optimized single-particle basis namely, the Berggren basis. This basis already includes information on the continuum on the level of single-particle states. With this basis we can solve the matrix eigenvalue problem of a complex symmetric Hamiltonian obtaining many-body resonance energies and eigenstates. The Berggren basis was already applied in the Gamow shell model (GSM) [Mic+02; Mic+03; Mic+08] as well as first applications in the NCSM with pure nucleon-nucleon interaction called the Gamow NCSM (GNCSM) [Pap+13; Li+19; Li+21]. Since we already include the the continuum in the many-body basis through the single-particle physics, we can naturally calculate the resonance states in the NCSM framework without any additional effort like the RGM. The concept of the NCSM is unchanged as only the single-particle basis is exchanged and the eigenvalue solver is modified in order to solve a complex symmetric eigenvalue problem.

This chapter introduces the basic concepts and the setup of the many-body model space of the NCSM. Afterwards, we show the impact of an alternative single-particle basis to optimize the convergence speed of the NCSM calculation. Even though we introduce the standard NCSM formulation here, the formulas and model space definitions used will still prove to be correct for the extension towards the GNCSM with the inclusion of the Berggren basis. We will discuss the necessary changes in chapter 7 later on.

2.1. Basic Concept

In the NCSM, the basis-independent eigenvalue problem in (1.1) is rewritten into a matrix eigenvalue problem using a complete set of Slater determinants $\{|\Phi_i\rangle\}$

$$\sum_i \langle \Phi_j | \hat{H} | \Phi_i \rangle \langle \Phi_i | \Psi_n \rangle = E_n \langle \Phi_j | \Psi_n \rangle. \tag{2.1}$$

This matrix eigenvalue problem can be solved numerically and yields the eigenvalues E_n and the expansion coefficients of the eigenstates

$$|\Psi_n\rangle = \sum_i C_{ni} |\Phi_i\rangle. \tag{2.2}$$

The Slater determinants are anti-symmetrized product states

$$|\Phi\rangle = |s_1 s_2 s_3 ... s_A\rangle_a = \sqrt{A!}\, \hat{\mathscr{A}} |s_1 s_2 s_3 ... s_A\rangle \tag{2.3}$$

with the antisymmetrizer $\hat{\mathscr{A}}$ [RS80] and single-particle basis states $\{|s\rangle = |n\,l\,j\,m_j\,m_t\rangle\}$. The collective index unites the radial quantum number n, the orbital angular momentum l, the total angular momentum j, its projection m_j and the isospin projection m_t. Since we only consider nucleons with spin $s = {}^1\!/_2$ and isospin $t = {}^1\!/_2$, we omit these quantum numbers in the collective index. The standard choice for the single-particle basis is the harmonic oscillator (HO) single-particle basis which offers two advantages. First, the eigenvalue problem of the single-particle HO Hamiltonian can be solved analytically and has analytic transformations from the spherical momentum basis as well as between single-particle coordinates and relative and center-of-mass coordinates. Second, the eigenstates of the nuclear Hamiltonian can factorize into a relative and a center-of-mass part if we use the so called N_{max} truncation, which is introduced in the next section. The HO potential has a free parameter which characterizes the strength of the potential, and therefore the range of the single-particle wave functions. This free parameter is usually described as the HO frequency Ω or the HO length a, which are related via

$$a = \sqrt{\frac{\hbar}{m_{\mathrm{N}}\Omega}}. \tag{2.4}$$

The range of the wave functions becomes larger for large HO lengths or small HO frequencies, respectively and vice versa. In this thesis, we redefine the HO frequency as $\hbar\Omega$ and use it to characterize the HO single-particle basis.

2.2. Model Space

The full Hilbert space as well as the many-body basis representation of Slater determinants is infinite dimensional, which makes it impossible to calculate an exact solution of the many-body Schrödinger equation numerically. Hence, the matrix eigenvalue problem of the NCSM is solved in a finite model space. The truncation scheme is built in such a way that an increase of the truncation parameter leads to an increase of the model space size. The goal is to reach convergence with respect to the truncation parameter. This means that an increase of the truncation parameter does not lead to a change in the observables. Before taking a closer look at the truncation schemes used later in this thesis, we want to resume to the consequences of the symmetries of the nuclear Hamiltonian, which can be exploited in the setup of the many-body Slater determinant basis.

Symmetries   The nuclear Hamiltonian is rotationally invariant and parity conserving. The first property also implies that the eigenvalues are independent of the total angular momen-

tum projection. We can use these symmetries and fix the desired total angular momentum projection quantum number M_J and parity π for the calculation in order to reduce the model space size. The Slater determinants are eigenstates to the total angular momentum projection operator $\hat{J}_z$ with eigenvalues

$$M(|\Phi\rangle) = \sum_{i=1}^{A} m_i. \tag{2.5}$$

Since we know that the eigenvalues of the nuclear Hamiltonian are independent of the total angular momentum projection, we can restrict the Slater determinant basis to Slater determinants with a fixed value for M_J. Similarly, the Slater determinants are eigenstates of the parity operator $\hat{\pi}$ with eigenvalues

$$\pi(|\Phi\rangle) = \prod_{i=1}^{A} (-1)^{l_i}. \tag{2.6}$$

We can use this property to divide the calculation of the nuclear spectrum in two, one calculation for each parity since it is computationally advantageous to solve the eigenvalue problem in two disjunct subspaces. The reason for that is, that the solution of an eigenvalue problem for a model space dimension d scales with $\mathscr{O}\left(d^3\right)$. Hence, the diagonalization of two subspaces with different parities and smaller basis dimension is computationally advantageous, especially if we are only interested in the results for a single parity.

The symmetries are used for all calculations as they are independent of any truncation scheme. In the following, we discuss two different truncation schemes which will be combined in the GNCSM later on.

Truncation   In case of the standard NCSM we truncate the model space by a maximum number of HO excitation quanta N_{max} allowed in a Slater determinant relative to a reference Slater determinant. Since all nucleons can be excited, they are active degrees of freedom, which is one of the differences to shell-model calculations with a frozen core. We define the number of excitation quanta N of a Slater determinant as

$$N(|\Phi\rangle) = \sum_{i=1}^{A} e_i - \sum_{i=1}^{A} e_i^{\text{ref}} \tag{2.7}$$

with the single-particle energy quantum number $e = 2n + l$. The energy e^{ref} describes the single-particle energies in the reference Slater determinant, which is a Slater determinant with the smallest possible HO energy. This definition of the N_{max} truncation stems from the use of the harmonic oscillator single-particle basis. The complete model space in the
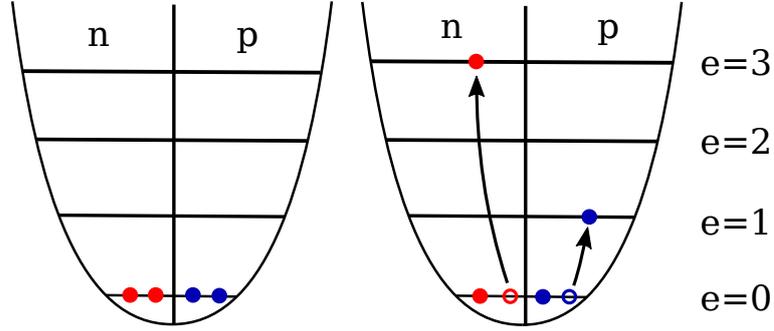
FIGURE 2.1.: Schematic representation of a ^{4}He reference Slater determinant on the left and an excited Slater determinant on the right with a total excitation energy of $N = 4$ or $T = 2$. This Slater determinant is part of the model space for $N_{\max} \geq 4$ or $T_{\max} \geq 2$, respectively.

standard NCSM is defined by

$$\mathcal{M}(N_{\max}, M_J, \pi) = \left\{ |\Phi\rangle \, : \, N(|\Phi\rangle) \leq N_{\max}, \, M(|\Phi\rangle) = M_J, \, \pi(|\Phi\rangle) = \pi \right\}. \qquad (2.8)$$

Figure 2.1 shows a schematic representation of the reference Slater determinant and an excited Slater determinant with $N = 4$ which would be included in the model space for $N_{\max} \geq 4$. Since the full Hilbert space is covered for $N_{\max} \to \infty$, we can study the convergence behavior of the eigenvalues and expect to receive a converged, exact result for sufficiently large $N_{\max}$. This property asserts the *ab initio* behavior of the NCSM where the $N_{\max}$ is the control parameter.

An example for NCSM calculation using SRG evolved and unevolved interactions from χEFT is shown in figure 2.2. In case of ^{4}He, the ground-state energy for the evolved interaction is converged at $N_{\max} = 10$, whereas the ground-state energy for the unevolved interaction does not reach convergence for the calculated $N_{\max}$ sequence. We can already see that the converged ground-state energy for the unevolved interaction is smaller than the result from the evolved interaction because the convergence with respect to $N_{\max}$ is decreasing monotonously. The deviation of the ground state energies for the evolved interaction is a consequence of the induced many-body contributions in the SRG evolution, which we neglect beyond the three-body level.

For ^{4}H, we can see that the ground-state energies for both interactions are not converged. The reason why the SRG works better for the ground-state energy of ^{4}He compared to the ground-state energy of ^{4}H can be explained as follows. The SRG evolution mainly suppresses
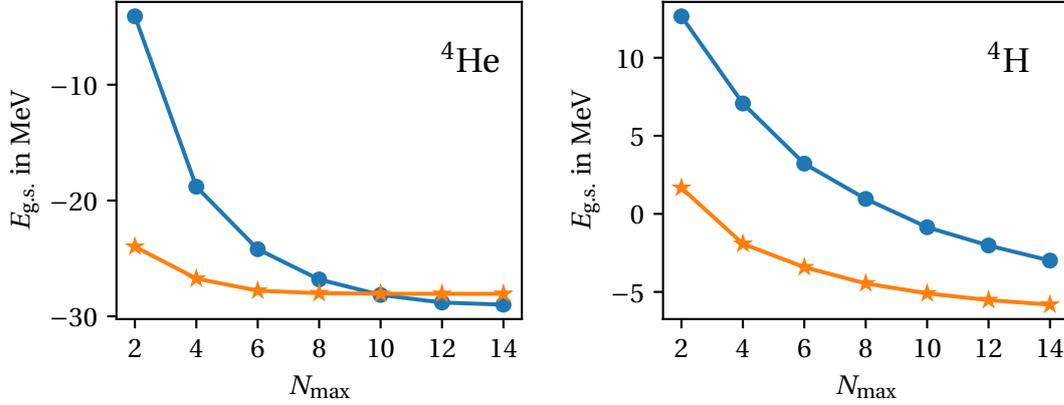
FIGURE 2.2.: Calculation of the ground state energies of ^{4}He and ^{4}H in the NCSM with respect to the model space truncation parameter $N_{\max}$ for an unevolved interaction with $\alpha = 0.0\,\text{fm}^{-4}$ (●) and a SRG evolved interaction with $\alpha = 0.08\,\text{fm}^{-4}$ (★). The interaction used is a chiral NN+3N interaction [EMN17; Hüt+20] at N^{3}LO with a non-local regulator function and a cutoff value of $\Lambda = 500\,\text{MeV}$. The HO basis uses the HO frequencies $\hbar\Omega = 40\,\text{MeV}$ and $20\,\text{MeV}$ for the unevolved and evolved interactions for ^{4}He, respectively, as well as $\hbar\Omega = 20\,\text{MeV}$ and $12\,\text{MeV}$ for the unevolved and evolved interactions for ^{4}H, respectively.

short-range corrections, hence, it has an impact on the short-range part of the wave function. The ground state of ^{4}He is strongly bound and has a small mass radius. On the other side, the ground state of ^{4}H is weekly bound and has a larger mass radius. Consequently, it is necessary to include Slater determinants with large radii in the model space in order to represent the ground state of ^{4}H. This means we have to use large $N_{\max}$ truncations to describe the ^{4}H ground state. This also explains why we use different HO frequencies for the SRG evolved and unevolved interaction in figure 2.2. In the complete Hilbert space, the converged result for an observable is independent of the HO frequency. However, the model-space convergence behavior of every observable depends on the HO frequency such that we can optimize the HO frequency for every calculation in order to get the best converge behavior. For the unevolved interactions, we need a high resolution in the short-range part of the basis states in order to describe the short-range correlations, which means small HO lengths or large HO frequencies, respectively. On the other hand, the SRG evolved interactions do not show strong short-range correlations and we get basis states with a larger HO lengths or smaller HO frequencies,

respectively.

Nevertheless, the SRG evolution still speeds up the convergence of the ground-state energy of ^{4}H. It is even more important to use SRG evolved interaction to describe heavier nuclei for which it is not possible to calculate results for larger N_{max}. In these cases, we rely on the SRG transformation to decrease the many-body uncertainty at the cost of a higher interaction uncertainty caused by the induced many-body contributions.

A different approach to truncate the model space is to truncate the number of particle-hole excitations allowed in a Slater determinant. The T_{max} truncation sets the maximum number of particle-hole excitations beyond the HO single-particle shells that are not occupied in the reference Slater determinant. Additionally, we have to apply a single-particle energy truncation e_{max} parameter in order to obtain finite model spaces. In case of the excitation shown in figure 2.1, the excited Slater determinant on the right-hand side corresponds to $T = 2$ since one neutron and one proton occupy a single-particle shell that is not occupied in the reference Slater determinant on the left. Similar to the N_{max} truncation, the full Hilbert space is covered for $e_{\mathrm{max}} \rightarrow \infty$ and T_{max} equal to the mass number A.

In the GNCSM, we will define a combined truncation consisting of an N_{max} truncation and a slightly adapted version of the T_{max} truncation.

2.3. Center-of-Mass Spuriousity

Physical observables like the energy spectrum or electromagnetic transitions of nuclei are independent of the center-of-mass motion of the nucleus. Hence, the nuclear Hamiltonian is translationally invariant, but the many-body basis in the NCSM which is constructed from Slater determinants is not translationally invariant in general. One exception is a model space spanned by HO Slater determinant basis with an N_{max} truncation [BNV13]. In this case it is possible to ensure that the NCSM eigenstates separate into an intrinsic and a center-of-mass part

$$|\Psi\rangle = |\Psi_{\mathrm{int}}\rangle \otimes |\Psi_{\mathrm{cm}}\rangle. \tag{2.9}$$

In order to shift the eigenstates with center-of-mass excitations out of the energy spectrum, we can add a center-of-mass Hamiltonian to the intrinsic Hamiltonian that only acts on the center-of-mass part of the wave function and keeps the intrinsic part of the wave function unchanged. The center-of-mass Hamiltonian reads

$$\hat{H}_{\mathrm{cm}} = \frac{1}{2m\hat{A}}\hat{\boldsymbol{P}}_{\mathrm{cm}}^2 + \frac{m\hat{A}\Omega^2}{2}\hat{\boldsymbol{X}}_{\mathrm{cm}}^2 - \frac{3}{2}\hbar\Omega \tag{2.10}$$

with the center-of-mass momentum $\hat{\boldsymbol{P}}_{\mathrm{cm}}$ and the center-of-mass coordinate $\hat{\boldsymbol{X}}_{\mathrm{cm}}$ [RGP09]. The center-of-mass Hamiltonian is added as so called Lawson term

$$\hat{H}(\lambda) = \hat{H}_{\mathrm{int}} + \lambda_{\mathrm{cm}}\hat{H}_{\mathrm{cm}}, \tag{2.11}$$

where λ_{cm} controls the strength of the center-of-mass Hamiltonian [RGP09].

For a different single-particle basis, the exact separation of the center-of-mass and the intrinsic part of the eigenstates is only possible in the full Hilbert space. We can still use the center-of-mass Hamiltonian for different single-particle basis sets and truncations in order to shift eigenstates with an excited center-of-mass part upwards in the spectrum. However, by including the center-of-mass Hamiltonian to the intrinsic Hamiltonian, the eigenvalue problem is altered, which can result in wrong results for the intrinsic energies if the eigenstates do not separate exactly.

2.4. Natural Orbitals

At first glance, the choice of the underlying single-particle basis seems to be not very important as for $N_{\mathrm{max}} \to \infty$ the solution of the many-body problem is independent of the underlying Slater determinant basis, i.e., the single-particle basis the Slater determinants are constructed from. However, the model space sizes to obtain converged results differ for different single-particle basis sets.

From a technical point of view the HO basis is advantageous compared to any other single-particle basis because we can use the analytic properties of the wave function and the basis transformations between relative and absolute coordinates. However, the HO single-particle states exhibit a Gaussian falloff, whereas the many-body wave function has an exponential falloff. This can lead to a slow convergence rate, and thus large model spaces are needed to get converged results in the NCSM calculation. In the past years, multiple sets of single-particle basis states have been used to perform NCSM calculations [Con+17; TMR19].

One possible ansatz to obtain a physically motivated single-particle basis is to calculate natural orbitals. Natural orbitals are the eigenstates of an one-body density matrix. The one-body density matrix elements for a many-body state $|\Psi_{\mathrm{ref}}\rangle$ are

$$\rho_{ij} = \langle\Psi_{\mathrm{ref}}|\hat{a}_i^\dagger\hat{a}_j|\Psi_{\mathrm{ref}}\rangle \tag{2.12}$$

with the single-particle creation and annihilation operators $\hat{a}^\dagger$ and $\hat{a}$, respectively. Thus, the natural orbitals depend on the choice of the many-body state $|\Psi_{\mathrm{ref}}\rangle$. In recent years, two
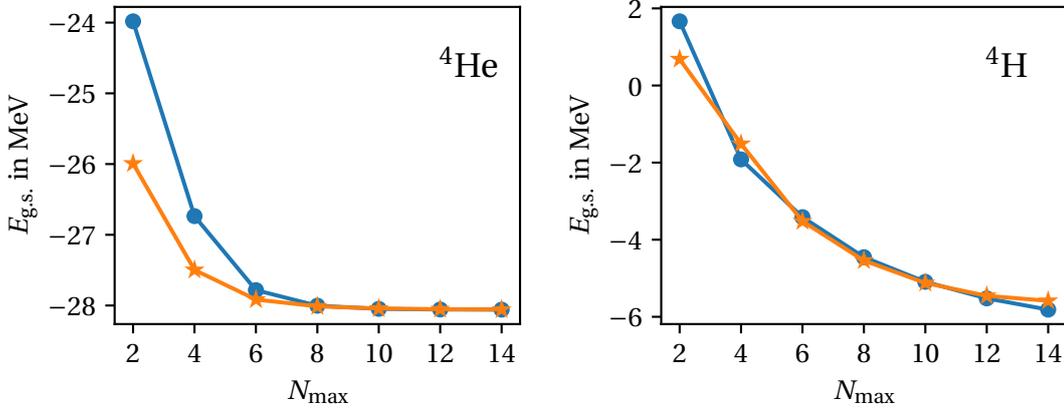
FIGURE 2.3.: Comparison of the HO (●) and NAT (★) single-particle basis on the convergence behavior of the ground-state energy for ^{4}He and ^{4}H. The HO frequencies for the HO calculation are $\hbar\Omega = 20\,\text{MeV}$ and $\hbar\Omega = 12\,\text{MeV}$ for ^{4}He (left) and ^{4}H, respectively. The NAT basis is independent of the HO frequencies and uses $\hbar\Omega = 20\,\text{MeV}$ for the underlying HO basis. The interaction used is the same as in figure 2.2 with a SRG evolution of $\alpha = 0.08\,\text{fm}^{-4}$. The center-of-mass strength parameter is $\lambda_{\text{cm}} = 0.3$ for the NAT basis.

different approaches were used to calculate the many-body state. Both approaches attempt to include physical properties from a large HO model space into the newly formed basis set of natural orbitals.

The first approach uses many-body perturbation theory to calculate a second-order perturbative correction to the Hartree-Fock ground-state Slater determinant which is used as the many-body reference state for the calculation of one-body density matrix [TMR19]. Figure 2.3 shows the impact on the convergence behavior compared to the HO basis. In case of ^{4}He the convergence is sped up by one step in the N_{max} convergence, however, for ^{4}H the convergence does not differ from the HO basis significantly. The natural orbitals perform better for heavier and well bound systems which is not the case for ^{4}H.

The second approach uses a many-body eigenstate from a NCSM calculation for the largest model space accessible in the HO basis [Con+17]. Afterwards, the calculation is repeated using the natural-orbital basis of this eigenstate. We will use a similar ansatz in order to calculate a natural orbitals basis from a GNCSM calculation later on.

3

THE BERGGREN BASIS

The aim of the Berggren basis is to include resonance and scattering states with a complex single-particle energy into the single-particle basis [Ber68]. Including those resonance and scattering states requires a new mathematical framework to work in because the Hilbert space is not able to describe unbound states. The new space we will use is a rigged Hilbert space, which also defines a new inner product. We do not discuss the mathematical framework of rigged Hilbert spaces in detail here, but rather give a short introduction to resonance states and the emerging difficulties, how they are resolved and how this affects our calculations later on. Note, in this section we will only demonstrate that it is formally possible to set up an orthogonal and complete Berggren basis [Ber68]. The actual framework to calculate the basis states will be the R-matrix method discussed in chapter 4.

3.1. Resonant and Capturing States

We start from the time-independent radial Schrödinger equation for a single particle

$$u_l''(k,r) - \frac{l(l+1)}{r^2} u_l(k,r) - \frac{2m}{\hbar^2} v(r) u_l(k,r) = -k^2 u_l(k,r) \tag{3.1}$$

with the orbital angular momentum quantum number l, mass m, Planck's constant $\hbar$, and radial wave functions $u_l(k,r)$. The one-body mean-field potential

$$v(r) = v_{\mathrm{N}}(r) + v_{\mathrm{C}}(r) \tag{3.2}$$

consists of a finite range nuclear potential v_N and a Coulomb potential v_C. Resonant states have a purely outgoing wave behavior for large distances as stated by Siegert [Sie39] and fulfill the boundary conditions

$$u_l(k, 0) = 0, \tag{3.3}$$

$$u_l(k, a)O_l'(ka) - u_l'(k, a)O_l(ka) = 0, \tag{3.4}$$

where a is a finite radius greater than the range of the nuclear part of the potential

$$v_N(r) = 0, \ \ r \geq a. \tag{3.5}$$

The wave function $O_l(kr)$ is the outgoing solution of equation (3.1) for a particle in a Coulomb field which is asymptotically proportional to

$$O_l(kr) \propto \exp\left(i\left(kr - \frac{l}{2}\pi\right)\right). \tag{3.6}$$

An equivalent solution can be defined for capturing states with purely incoming solutions $\tilde{u}(k, r)$ and the boundary conditions

$$\tilde{u}_l(k, 0) = 0, \tag{3.7}$$

$$\tilde{u}_l(k, a)I_l'(\tilde{k}a) - \tilde{u}_l'(k, a)I_l(\tilde{k}a) = 0, \tag{3.8}$$

where $I_l(\tilde{k}r)$ is the incoming solution of equation (3.1) for a particle in a Coulomb field. It is possible to show that the wave functions $u(k, r)$ and $\tilde{u}(k, r)$ as well as the momenta k and $\tilde{k}$ fulfill the following properties

$$\tilde{u}(k, r) = u(k, r)^*, \tag{3.9}$$

$$\tilde{k} = -k^*, \tag{3.10}$$

$$\text{Im}(k) = \text{Im}(-k^*) < 0, \ \ \text{Re}(k) \neq 0. \tag{3.11}$$

Hence, the momentum can be parametrized as

$$k = k_R - i\kappa, \ \ \kappa > 0. \tag{3.12}$$

The energy of a resonance has a negative imaginary part which is commonly parametrized via

$$E = E_R - i\frac{\Gamma}{2}. \tag{3.13}$$

These two parametrizations lead to two more characteristics of resonance states. First, inserting this energy into the time evolution operator acting on a resonance eigenstate $|u(t)\rangle$ yields

$$|u(k,t)\rangle = \exp\left(-\frac{i}{\hbar}\hat{H}t\right)|u(k,0)\rangle = \exp\left(-\frac{i}{\hbar}E_R t\right)\exp\left(-\frac{\Gamma}{2\hbar}t\right)|u(k,0)\rangle \qquad (3.14)$$

with the exponential decay rate depending on the imaginary part of the energy which connects Siegert's definition of resonance states as outgoing wave functions [Sie39] with Gamow states [Gam28].

A problem arises with the second characteristic of resonance states, they are divergent for large distances

$$u_l(k,r) \propto \exp\left(i\left(k_R r - \frac{l}{2}\pi\right)\right)\exp(\kappa r). \qquad (3.15)$$

However, Berggren used a different inner product for a resonance, capturing, and bound states and was able to show that they are orthogonal and normalizable to

$$\langle \tilde{u}(k)_j | u(k)_i \rangle = \delta_{ij}. \qquad (3.16)$$

This inner product is different from the inner product in the traditional Hilbert space. The expanded space which contains resonance and scattering as well as bound states is called the rigged Hilbert space (RHS) [GV64; Mic+08], which consists of a biorthogonal basis, i.e., different single-particle basis sets for the bra and the ket space. Note, that equation (3.9) yields a relation between incoming and outgoing states and it appears that the only obvious difference to the traditional framework of the Hilbert space is that the radial part of the wave function in the dual Hilbert space is equivalent to the radial part in the Hilbert space. The norm of resonance states is

$$N_l^2 = \int_0^\infty \tilde{u}_l(k,r)^* \, u_l(k,r) \, dr = \int_0^\infty u_l(k,r)^2 dr, \qquad (3.17)$$

which looks similar to the norm of bound states in the traditional Hilbert space. There are different ways to regularize the norm integral for resonance states. Berggren used the ansatz of Zel'dovich [Ber68] to prove that it is possible to regularize resonance states. We use the exterior complex scaling method in order to regulate the resonance states in section 4.4 [GV71].

3.2. Completeness Relation

The last ingredient for a complete single-particle basis is a proper completeness relation. A single-particle basis consisting of bound and real energy scattering states was already defined
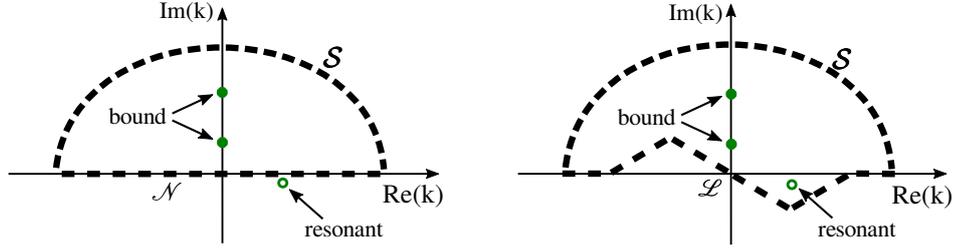
FIGURE 3.1.: Schematic representation of two possible contours in the complex momentum plane. On the left, the Newton contour ($\mathcal{N}$) includes bound states (●) and a real energy continuum. On the right, the Berggren contour ($\mathcal{L}$) additionally includes resonances (○) in the fourth quadrant of the complex momentum plane and includes complex scattering states as well.

by Newton [Lin93] using the contour shown in the left-hand side of figure 3.1. Berggren was able to define a different path $\mathcal{L}$ of the contour departing from the real axis. The contours are evaluated using Cauchy's theorem with the bound and resonance states as poles of the S-matrix. The final Berggren completeness relation is given by

$$\hat{\mathbb{1}} = \sum_{n=b,r} |u_n\rangle\langle\tilde{u}_n| + \frac{1}{\pi} \int_{\mathcal{L}} |u(k)\rangle\langle\tilde{u}(k)| \, dk, \tag{3.18}$$

where we sum over all bound (b) and resonance (r) states and integrate over the scattering continuum along the path of the contour $\mathcal{L}$ shown in figure 3.1. In practical applications the integral is discretized yielding

$$\hat{\mathbb{1}} = \sum_{n=b,r} |u_n\rangle\langle\tilde{u}_n| + \sum_i w_i |u(k_i)\rangle\langle\tilde{u}(k_i)| \tag{3.19}$$

with the discretized momenta k_i and their corresponding weights w_i, which formally results in a discrete completeness relation [Mic+08].

4

R-Matrix Method

With the Berggren completeness relation at hand, the formal ground is set to build a single-particle basis of bound, resonance and scattering states. In this chapter, we introduce the R-matrix method which is a useful tool to calculate the relative interaction of two subsystems or clusters [DB10]. These systems can be single nucleons or nuclei. In case of the NCSM/RGM method mentioned earlier, the R-matrix is successfully used to describe the interaction between a well bound $(A-1)$-particle nucleus and a single nucleon [QN08; QN09; NRQ10].

In our case we intend to use the single-channel R-matrix method to construct a set of single-particle Berggren states. The formal description follows Descouvemont et al. [DB10] who provide a detailed review on the R-matrix method and its applications.

4.1. Basics

In order to obtain a single-particle basis, we use the R-matrix method to describe the relative wave function of a single nucleon and the residual $(A-1)$ particle nucleus. The one-body mean-field potential is split into a nuclear potential V_{N} as the finite range interaction generated by the $(A-1)$-particle nucleus and the Coulomb potential, which is treated explicitly. The Coulomb potential influences the asymptotic wave function, which we calculate analytically. The radial Schrödinger equation for the partial wave l reads

$$H_l u_l(k,r) = \left[\left(\frac{A-1}{A} \right) \left(-\frac{\hbar^2}{2m_{\mathrm{N}}} \frac{d^2}{dr^2} + \frac{\hbar^2 l(l+1)}{2m_{\mathrm{N}} r^2} \right) + V_{\mathrm{C}}(r) + V_{\mathrm{N}}(r) \right] u_l(k,r) = E u_l(k,r). \quad (4.1)$$

The energy is connected to the momentum via

$$E = \left(\frac{A-1}{A}\right) \frac{\hbar^2 k^2}{2 m_N}. \tag{4.2}$$

Note, we do not use a reduced mass in our formulation of the kinetic energy, but rather use the coordinate representation of the one-body part of the intrinsic kinetic energy operator defined in equation (1.4). This specific choice is helpful later on for the calculation of the nuclear matrix elements in chapter 6.

In the R-matrix approach, we split the coordinate space into an internal and an external region. The matching point is called channel radius R_c and it has to be chosen large enough such that

$$V_N(r) = 0, r \geq R_c. \tag{4.3}$$

We perform the calculation of the internal and external solutions of the wave function

$$u_l(k,r) = \begin{cases} u_l^{\text{int}}(k,r), & \text{if } r \leq R_c, \\ u_l^{\text{ext}}(k,r), & \text{if } r > R_c, \end{cases} \tag{4.4}$$

separately and match them at the channel radius

$$u_l^{\text{int}}(k, R_c) = u_l^{\text{ext}}(k, R_c), \tag{4.5}$$

$$u_l^{'\,\text{int}}(k, R_c) = u_l^{'\,\text{ext}}(k, R_c). \tag{4.6}$$

In the external region, the wave functions can be calculated analytically since we assume that the nuclear potential vanishes. Hence, we describe a free neutron or proton in a Coulomb potential of the residual protons ($Z > 1$). In the internal region the solution for $u_l^{\text{int}}(k,r)$ can be approximated over a finite set of basis functions $\varphi_i(r)$

$$u_l^{\text{int}}(k,r) = \sum_{i=1}^N c(k)_i \varphi_i(r) \tag{4.7}$$

with expansion coefficients $c(k)_i$. We use a set of Lagrange functions which have empirically shown to yield converged results for a small number of mesh points N [DB10]. One problem arising with the definition of an internal and an external region is that the Hamiltonian is non-hermitian in the internal region because it is not probability preserving. This can be solved by introducing the so called Bloch operator [Yvo57; DB10]

$$L(B) = \left(\frac{A-1}{A}\right) \frac{\hbar^2}{2 m_N} \delta(r - R_c) \left(\frac{d}{dr} - \frac{B}{r}\right) \tag{4.8}$$

with a real number B as discussed later on. Thus, the radial Schrödinger equation from (4.1) is transformed to the so called Bloch-Schrödinger equation in the internal region

$$(H_l + L(B) - E)\, u_l^{\text{int}} = L(B)\, u_l^{\text{ext}}. \tag{4.9}$$

If we combine this equation with the matching condition from equation (4.5) we find that the Bloch-Schrödinger equation is equivalent to the initial radial Schrödinger equation since the Dirac delta function in the Bloch operator restricts its impact to the channel radius.

With the general approach of the R-matrix method set, we can start calculating bound, resonance and scattering states. Originally, the R-matrix method was used only for wave functions in the continuum [Wig46; WE47; LT58], i.e., resonance and scattering states, but it is possible to extend the approach towards bound states [BD83]. The next sections introduce the procedure to calculate bound, resonance and scattering states.

4.2. Bound States

For the calculation of bound states, we exploit that bound states have a negative real energy, such that the asymptotic wave functions fall off to zero. There are multiple ways to calculate bound states for a given Hamiltonian, e.g., via the solution of an eigenvalue problem, which is essentially done in the R-matrix approach in the internal region. In the external region, the wave functions have an exponential falloff. We start the discussion of bound states in the external region followed by the internal region.

External Region   The radial Schrödinger equation in the external region omits the nuclear potential from equation (4.1) and we can rewrite it to Whittaker's equation [Olv+22] via

$$\left[\left(\frac{A-1}{A} \right) \left(-\frac{\hbar^2}{2m_{\text{N}}} \frac{d^2}{dr^2} + \frac{\hbar^2 l(l+1)}{2m_{\text{N}} r^2} - \frac{\hbar^2 k^2}{2m_{\text{N}}} \right) + \frac{(Z-1)e^2}{r} \right] u_l(k,r) = 0 \tag{4.10}$$

$$\Longleftrightarrow \qquad \left[\frac{d^2}{dr^2} - \frac{l(l+1)}{r^2} - \left(\frac{A}{A-1} \right) \frac{2m_{\text{N}}(Z-1)e^2}{\hbar^2 r} + k^2 \right] u_l(k,r) = 0 \tag{4.11}$$

$$\overset{k \to i\kappa}{\Longleftrightarrow} \qquad \left[\frac{1}{\kappa^2} \frac{d^2}{dr^2} - \frac{l(l+1)}{\kappa^2 r^2} - \left(\frac{A}{A-1} \right) \frac{2m_{\text{N}}(Z-1)e^2}{\hbar^2 \kappa^2 r} - 1 \right] u_l(\kappa,r) = 0 \tag{4.12}$$

$$\overset{r \to \frac{z}{2\kappa}}{\Longleftrightarrow} \qquad \left[\frac{d^2}{dz^2} - \frac{l(l+1)}{z^2} - \left(\frac{A}{A-1} \right) \frac{m_{\text{N}}(Z-1)e^2}{\hbar^2 \kappa z} - \frac{1}{4} \right] u_l(\kappa,z) = 0 \tag{4.13}$$

$$\Longleftrightarrow \qquad \left[\frac{d^2}{dz^2} - \frac{l(l+1)}{z^2} - \frac{\eta_{\text{B}}}{z} - \frac{1}{4} \right] u_l(\kappa,z) = 0. \tag{4.14}$$

In the second step, we use that a bound state has a real negative eigenvalue and can be represented by a positive imaginary momentum and in the third step, we transform the coordinate. The last step simplifies the equations using the real Sommerfeld parameter

$$\eta_{\mathrm{B}} = \left(\frac{A}{A-1}\right)\frac{m_{\mathrm{N}}(Z-1)e^2}{\hbar^2\kappa}. \tag{4.15}$$

The solution to equation (4.14) is the Whittaker function [Olv+22]

$$W(\eta_{\mathrm{B}}, l, z) = \exp\left(-\frac{1}{2}z\right)z^{l+1}U\left(1+l+\eta_{\mathrm{B}}, 2+2l, z\right) \tag{4.16}$$

with Kummer's function U.

Internal Region   In the internal region, we start with the Bloch-Schrödinger equation (4.9) and set the Bloch parameter to

$$B(\kappa_{\mathrm{B}}) = 2\kappa_B a \frac{W'(\eta_{\mathrm{B}}, l, 2\kappa_{\mathrm{B}}R_{\mathrm{c}})}{W(\eta_{\mathrm{B}}, l, 2\kappa_{\mathrm{B}}R_{\mathrm{c}})}, \tag{4.17}$$

which suppresses the right-hand side of the equation. The bound state momentum κ_{B} is connected to the bound state energy E_{B} via

$$E_{\mathrm{B}} = -\left(\frac{A-1}{A}\right)\frac{\hbar^2\kappa^2}{2m_{\mathrm{N}}}. \tag{4.18}$$

Applying the expansion in the Lagrange functions φ_i results in the Bloch-Schrödinger equation

$$\sum_{j=0}^{N} \langle\varphi_i|H_l + L(B(E_{\mathrm{B}}))|\varphi_j\rangle c_j = E_B c_i. \tag{4.19}$$

This equation is similar to a standard eigenvalue problem, but the value for the Bloch parameter B depends on the eigenvalue E_{B}. This problem is numerically solved by an iterative approach, treating the eigenvalue problem for $B = 0$ and updating the Bloch parameter after each matrix eigenvalue solution. However, the iterative process may become unstable if the amplitude of the wave function and its derivative is small at the channel radius. In practice, we do not iterate if the channel radius is chosen large enough, such that the wave functions have already fallen off to zero. Hence, the contribution of the Bloch operator on the left-hand side of equation (4.9) vanishes similar to the Bloch operator on the right-hand side of the equation discussed before.

4.3. Resonance and Scattering States

As discussed for the Berggren single-particle basis, the energy of resonance and scattering states is complex with a positive real part. The wave functions behave like particles in a Coulomb field in the external region, which requires a different approach compared to bound states. An important aspect of scattering theory is to locate the resonance states. We use the so called scattering or S-matrix, which exhibits a pole for a resonance energy. Before we can define the S-matrix in the R-matrix approach it is necessary to calculate the internal and external solutions of the wave functions which are needed to define and derive the S-matrix.

External Region   In case of resonances and scattering states, the wave functions in the external region are given by the solutions of the Coulomb wave equation. We start from the radial Schrödinger equation with a Coulomb potential as in equation (4.11), but with the key difference that the momentum k is a complex number

$$\left[\frac{d^2}{dr^2} - \frac{l(l+1)}{r^2} - \frac{2k\eta}{r} + k^2 \right] u_l(k,r) = 0 \tag{4.20}$$

$$\iff \left[\frac{1}{k^2} \frac{d^2}{dr^2} - \frac{l(l+1)}{k^2 r^2} - \frac{2\eta}{kr} + 1 \right] u_l(k,r) = 0 \tag{4.21}$$

$$\overset{r \to \frac{z}{k}}{\iff} \quad \left[\frac{d^2}{dz^2} - \frac{l(l+1)}{z^2} - \frac{2\eta}{kz} + 1 \right] u_l(z) = 0. \tag{4.22}$$

with the complex Sommerfeld parameter

$$\eta = \left(\frac{A}{A-1} \right) \frac{m_{\mathrm{N}}(Z-1)e^2}{\hbar^2 k}. \tag{4.23}$$

The solutions of the Coulomb wave equation are the regular and irregular Coulomb functions $F_l(\eta, z)$ and $G_l(\eta, z)$, respectively. For our solutions, we will use the conjugate functions

$$H_l^+(\eta, z) = G_l(\eta, z) + i F_l(\eta, z) \tag{4.24}$$

$$H_l^-(\eta, z) = G_l(\eta, z) - i F_l(\eta, z) \tag{4.25}$$

which correspond to incoming (-) and outgoing (+) waves in the asymptotic region. The external solution of the Schrödinger equation will be a linear superposition of these conjugate functions

$$u_l^{\mathrm{ext}}(\eta, z) = C^+ H_l^+(\eta, z) + C^- H_l^-(\eta, z) \tag{4.26}$$

$$= C_l \left(H_l^-(\eta, z) - S_l H_l^+(\eta, z) \right) \tag{4.27}$$

with the normalization constants C^+, C^- and C_l. The S-matrix S_l of partial wave l appears for the first time and will be calculated in the internal region. The normalization C_l is given by

$$C^+ C^- = \frac{1}{2\pi}, \tag{4.28}$$

$$C_l = C^- = \sqrt{-\frac{1}{2\pi S_l}}, \tag{4.29}$$

which originates from the normalization to the Dirac delta function for scattering states [Mic+08]. As discussed before, resonance states have a purely outgoing wave function in the asymptotic region, which corresponds to a pole in the S-matrix at the resonance energy

$$S_l \to \infty, \tag{4.30}$$

$$C_l \to 0. \tag{4.31}$$

Internal Region For the calculation of the internal part, it is possible to show that the results of the R-matrix calculation do not depend on the Bloch parameter B. Thus, in order to simplify the equations we set it to zero and neglect it in the following formulas. We define the R-matrix at an energy E as

$$R_l(E) = \frac{u_l(k, R_c)}{u_l'(k, R_c)}, \tag{4.32}$$

which is the inverse logarithmic derivative at the channel radius. The definition of the R-matrix is needed to calculate the S-matrix later on. Now, we can start from the Bloch-Schrödinger equation (4.9) again and use the Lagrange basis expansion (4.7) to get

$$\sum_{i=1}^{N} \langle \varphi_i | H_l + L(0) - E | \varphi_j \rangle c_j = \left(\frac{A-1}{A} \right) \frac{\hbar^2}{2m_N} \varphi_i(R_c) u_l'^{\,\text{ext}}(k, R_c), \tag{4.33}$$

where we projected the equation on $\varphi_i(r)$. We define the left-hand side matrix element as the so called C-matrix for partial wave l

$$[C_l(E)]_{ij} = \langle \varphi_i | H_l + L(0) - E | \varphi_j \rangle. \tag{4.34}$$

The solution of the Bloch-Schrödinger equation yields the coefficients c_i, which can be inserted into the basis expansion (4.7). This allows the calculation of the R-matrix for a given energy

$$R_l(E) = \left(\frac{A-1}{A} \right) \frac{\hbar^2}{2m_N R_c} \sum_{i,j=1}^{N} \varphi_i(R_c) [C_l(E)]_{ij}^{-1} \varphi_j(R_c). \tag{4.35}$$

The internal wave function is then given by

$$u_l^{\text{int}}(k,r) = \left(\frac{A-1}{A}\right) \frac{\hbar^2}{2m_{\text{N}} R_l(E)} u_l^{\text{ext}}(k, R_{\text{c}}) \sum_{j=1}^{N} \varphi_j(r) \sum_{i=1}^{N} [C_l(E)]_{ij}^{-1} \varphi_i. \tag{4.36}$$

Up to now, the Bloch-Schrödinger equation has to be solved for every energy E explicitly. Since we are using an orthonormal set of basis functions, it is possible to reduce the computational cost of the R-matrix calculation. We start from an eigenvalue problem of the C-matrix for $E = 0$

$$[C_l(0)]\,\boldsymbol{v}_{nl} = E_{nl}\boldsymbol{v}_{nl} \tag{4.37}$$

with eigenvalues E_{nl} and eigenstates $\boldsymbol{v}_{nl}$. The spectral decomposition yields

$$[C_l(E)]^{-1} = \sum_{n=1}^{N} \frac{\boldsymbol{v}_{nl}\boldsymbol{v}_{nl}^{\text{T}}}{E_{nl} - E} \tag{4.38}$$

with the number of mesh points N. This equation can be inserted into equation (4.35) for the R-matrix to get

$$R_l(E) = \sum_{n=1}^{N} \frac{\gamma_{nl}^2}{E_{nl} - E} \tag{4.39}$$

with the reduced width amplitude

$$\gamma_{nl} = \left(\left(\frac{A-1}{A}\right) \frac{\hbar^2}{2m_{\text{N}} R_{\text{c}}}\right)^{\frac{1}{2}} \sum_{i=1}^{N} \boldsymbol{v}_{nl,i}\varphi_i(R_{\text{c}}). \tag{4.40}$$

This approach only needs one matrix eigenvalue solution of the C-matrix at zero energy and we are able to calculate the R-matrix for every energy E afterwards.

S-Matrix The S-matrix plays an important role in the location of the resonance states. As we have seen in equation (4.30) the poles of the S-matrix correspond to resonance states. In the R-matrix approach, the S-matrix of partial wave l is determined by

$$S_l(k) = \exp\big(2i\phi_l\big) \frac{1 - L_l^* R_l(E)}{1 - L_l R_l(E)} \tag{4.41}$$

with the logarithmic derivative of the outgoing wave function H_l^+

$$L_l(k) = ka \frac{H_l^{\prime +}(\eta, kR_{\text{c}})}{H_l^+(\eta, kR_{\text{c}})} \tag{4.42}$$

and the phase shift

$$\phi_l(k) = \arg(H_l^-(\eta, kR_{\text{c}})) \tag{4.43}$$

at the channel radius.

4.4. Normalization

The norm of the total wave function of the bound state is given by the traditional norm in the Hilbert space. Since we calculate the norm numerically, we use a cutoff value R for the norm integral

$$N^2 = \int_0^R (u_l(k,r))^2 \, dr. \tag{4.44}$$

The cutoff value R is chosen large enough such that

$$u_l(r) \simeq 0 \ \text{ if } r \geq R. \tag{4.45}$$

For scattering states, it is possible to normalize the external wave function to the Dirac delta function as shown in equation (4.28). Since the internal wave function is connected to the external wave function via the matching conditions it is normalized accordingly.

In case of resonance states, Berggren has shown that it is possible to normalize a resonance wave function using the ansatz of Zel'dovich [Ber68]. Since this regularization scheme is numerically unstable, we make use of a different approach known as exterior complex scaling (ECS) [GV71]. The ECS is a rotation of the coordinate axis into the complex energy plane in the asymptotic region of the wave function. The unitary transformation of the coordinate reads

$$\boldsymbol{r} \rightarrow \boldsymbol{r} e^{i\theta} \tag{4.46}$$

with the rotation angle θ. The rotation angle has to be chosen large enough such that

$$2\theta > |\arg(E_\mathrm{r})| \tag{4.47}$$

with the energy of the resonance state E_r. The transformed states

$$U(\theta) u_l(k,r) = \begin{cases} u_l(k,r), & \text{if } r \leq a, \\ u_l\left(k, a + |r-a| e^{i\theta}\right) & \text{if } r > a \end{cases} \tag{4.48}$$

become square integrable under two conditions: First, the potential has to have a finite range smaller than a or has to fall of faster or equal to r^{-1}, which includes the Coulomb interaction. Second, they have to be purely incoming or outgoing waves, which is the case for resonance states, but not for scattering states. A schematic illustration of the coordinate transformation is shown in figure 4.1.

Using the ECS to calculate the norm defined in equation (3.17) we find

$$N_l^2 = \int_0^\infty u_l(k,r)^2 dr = \int_0^a u_l(k,r)^2 dr + \int_a^\infty u_l(k, a + |r-a| e^{i\theta})^2 e^{i\theta} dr. \tag{4.49}$$
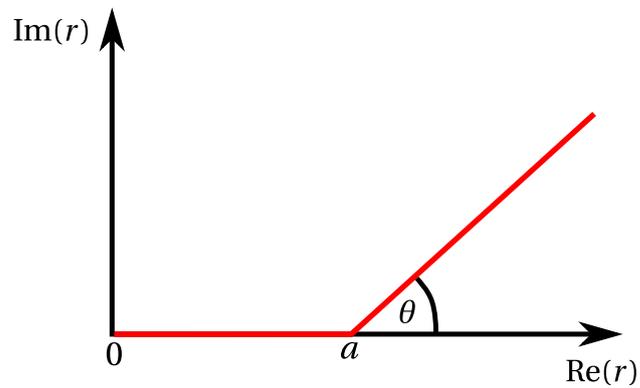
FIGURE 4.1.: Illustration of the coordinate transformation in the exterior complex scaling with scaling radius a and scaling angle θ.

It is also possible to calculate matrix elements of resonance states for a localized interaction using the ECS. However, this does not work for scattering states and the realistic interactions we are interested in. The former consists of ingoing and outgoing wave functions and the exterior complex scaling is only able to suppress one contribution of these two. This only works for resonance states, which have a purely outgoing wave function. In case of realistic interactions, we are unable to calculate the coordinate representation of realistic interactions except for a basis expansion, which results in a non-local representation for resonance and scattering states. In this case, we cannot use the exterior complex scaling as well. In the next chapter, we will discuss a different approach to calculate interaction matrix elements in the Berggren basis.

PART II.

GAMOW NO-CORE

SHELL MODEL

FRAMEWORK

INTRODUCTION TO PART II

In the first part of this thesis, we introduced the fundamental elements necessary to develop the Gamow NCSM (GNCSM) framework. All of these fundamental tools will be used in the following part, which covers the entire development of the GNCSM framework. In figure II.A, we show a schematic representation of the relevant steps towards a final many-body result. We start with the setup of the single-particle Gamow basis using the Berggren completeness relation. For the calculation of the single-particle basis we use the R-matrix method. From the R-matrix we obtain a coordinate representation of the single-particle Berggen wave functions, which we use to calculate the interaction matrix elements. These matrix elements are the relevant input for the first GNCSM calculation. However, after the approximation of the scattering and resonance wave functions, the single-particle basis is non-orthonormal, which induces problems for the solution of the eigenvalue problem. Thus, we setup a new single-particle basis constructed from the one-body density matrix of the first GNCSM states, namely the Gamow natural orbitals. This basis set is orthonormal and we are able to calculate the matrix elements using a basis expansion. With these new Gamow natural orbitals, we perform our final natural orbital GNCSM (NAT-GNCSM) calculations.

In order to keep track of the important steps for the application of the GNCSM for future applications we will summarize the relevant steps of the calculation in form of a small "cheat sheet" in every chapter in this part of the thesis. Additionally, we include all relevant parameters and truncation that occur during the development. The parameters characterize and define the structure of the single-particle basis, e.g., the potential parameters. An analogous parameter in the standard NCSM with the HO single-particle basis is the HO frequency. In the complete Hilbert space, the many-body results are independent of the single-particle basis,

GNCSM framework

Gamow basis
(chapter 5)

↓

Matrix elements
(chapter 6)

↓

GNCSM
(chapter 7)

↓

NAT-GNCSM
(chapter 8)
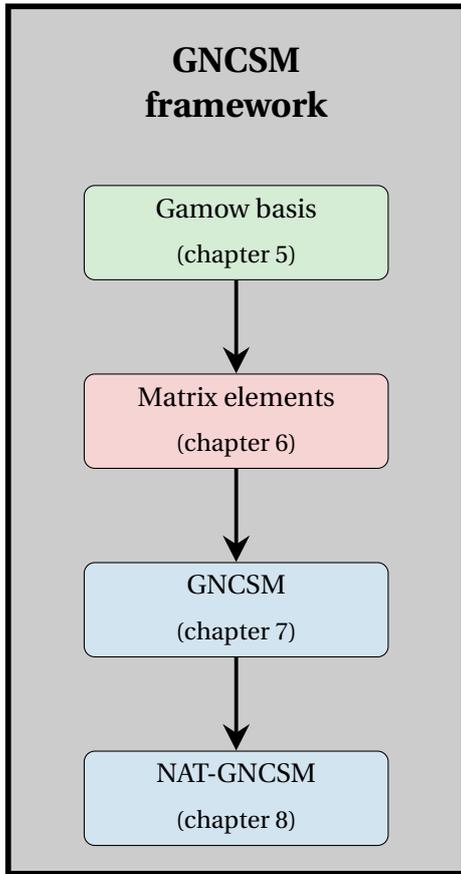
FIGURE II.A.: Illustration of the individual steps in the calculation of many-body resonance states in the GNCSM framework. They are discussed in detail in the following chapters.

i.e., the HO frequency. But the convergence behavior with increasing model space dimension differs for different HO frequencies. The truncations truncate the single-particle Gamow basis and the many-body model space. If we are able to converge truncations universally, we show the converged values as well. The convergence behavior with respect to the remaining truncations depends on the specific nucleus and needs to be analyzed individually.

5

SETUP GAMOW BASIS

The first step in the development of a GNCSM framework is the setup of a suitable single-particle basis. For the calculation of the Berggren basis, we have to define a single-particle potential $V_N(r)$ and identify bound and resonance states. Since it is computationally not feasible to use all partial waves in a Berggren basis in a NCSM type calculation, we have to determine which partial waves are important to have the continuum degrees of freedom included. All other partial waves will be described in the single-particle HO basis. We call the newly formed single-particle basis Gamow basis.

5.1. One-Body Potential

As we have seen in the introduction of the R-matrix method in chapter 4, the one-body potential is split into a finite nuclear part $\hat{V}_N(\hat{r})$, which falls off faster than r^{-1} in the asymptotic region, and a Coulomb potential, which can be solved analytically in the external region. If not stated otherwise, we use a Woods-Saxon potential combined with a spin-orbit potential

$$\hat{V}_N(\hat{r}) = \frac{V_{WS}}{1 + \exp\left(\frac{(\hat{r} - R_{WS})}{a_{WS}}\right)} + V_{LS} \frac{\exp\left(\frac{(\hat{r} - R_{WS})}{a_{WS}}\right)\hat{\vec{l}} \cdot \hat{\vec{s}}}{\hat{r}\, a_{WS}\left[1 + \exp\left(\frac{(\hat{r} - R_{WS})}{a_{WS}}\right)\right]^2} \tag{5.1}$$

with the potential depths V_{WS} and V_{LS}, the width of the potential R_{WS}, and the surface parameter a_{WS}. In case of the Coulomb potential, we use the electrostatic potential of a

homogenous sphere

$$\hat{V}_{\mathrm{C}}(\hat{r}) = \begin{cases} \frac{3(Z-1)e^2}{2R_{\mathrm{WS}}}\left(1 - \frac{\hat{r}^2}{3R_{\mathrm{WS}}^2}\right), & \text{if } r \leq R_{\mathrm{WS}}, \\ \frac{(Z-1)e^2}{\hat{r}}, & \text{if } r > R_{\mathrm{WS}}, \end{cases} \tag{5.2}$$

where Z is the proton number of the system and e is the elementary charge.

The modification of the parameter values for the nuclear potential can change the structure of the single-particle basis, and thus can influence the final results for the many-body energies in the GNCSM calculation. A suitable choice for these values becomes important later on.

5.2. Locate Single-Particle Resonance States

After the potential is defined, we need to locate the single-particle resonance states, i.e., poles in the S-matrix. The S-matrix is calculated within the R-matrix method using equation (4.41). In order to search for poles in the S-matrix, we calculate the S-matrix values on a coarse energy grid for an energy range between $0\,\mathrm{MeV}$ and $(10 - 10\mathrm{i})\,\mathrm{MeV}$ with 100 mesh points in the real and imaginary direction. In a first iteration, we search for local maxima on this grid. Afterwards, the precise location of each local maximum is searched for on a finer grid. The procedure is depicted in figure 5.1. In order to benchmark the procedure, we use a known toy potential that reproduces the p+^{12}C scattering energy approximately. It is a Gaussian potential with a point-like Coulomb source [DB10]

$$\hat{V}_{\mathrm{N}}(\hat{r}) = -73.8\,\mathrm{MeV} \cdot \exp\left(-\left(\frac{\hat{r}}{2.7\,\mathrm{fm}}\right)^2\right), \tag{5.3}$$

$$\hat{V}_{\mathrm{C}}(\hat{r}) = 6e^2/\hat{r}. \tag{5.4}$$

For the channel radius we used $R_{\mathrm{c}} = 12\,\mathrm{fm}$ and the mesh size in the internal region is $N = 30$ which lead to converged results. In the next section, we discuss the dependence on these two parameters in more detail. The iterative approach to calculate the resonance energy converges at

$$E \approx (0.414\,63 - 0.018\,19\mathrm{i})\,\mathrm{MeV}. \tag{5.5}$$

The experimental value for the resonance of the p+^{12}C system is

$$E_{\mathrm{exp}} \approx (0.42 - 0.0185\mathrm{i})\,\mathrm{MeV} \tag{5.6}$$

in the $l = 0$ partial wave [Ajz91; DB10]. Note, the difference of the two values may result from an inaccurate parametrization of the potential. The aim of this example is to present the method which is used to locate the resonances and calculate their energy.
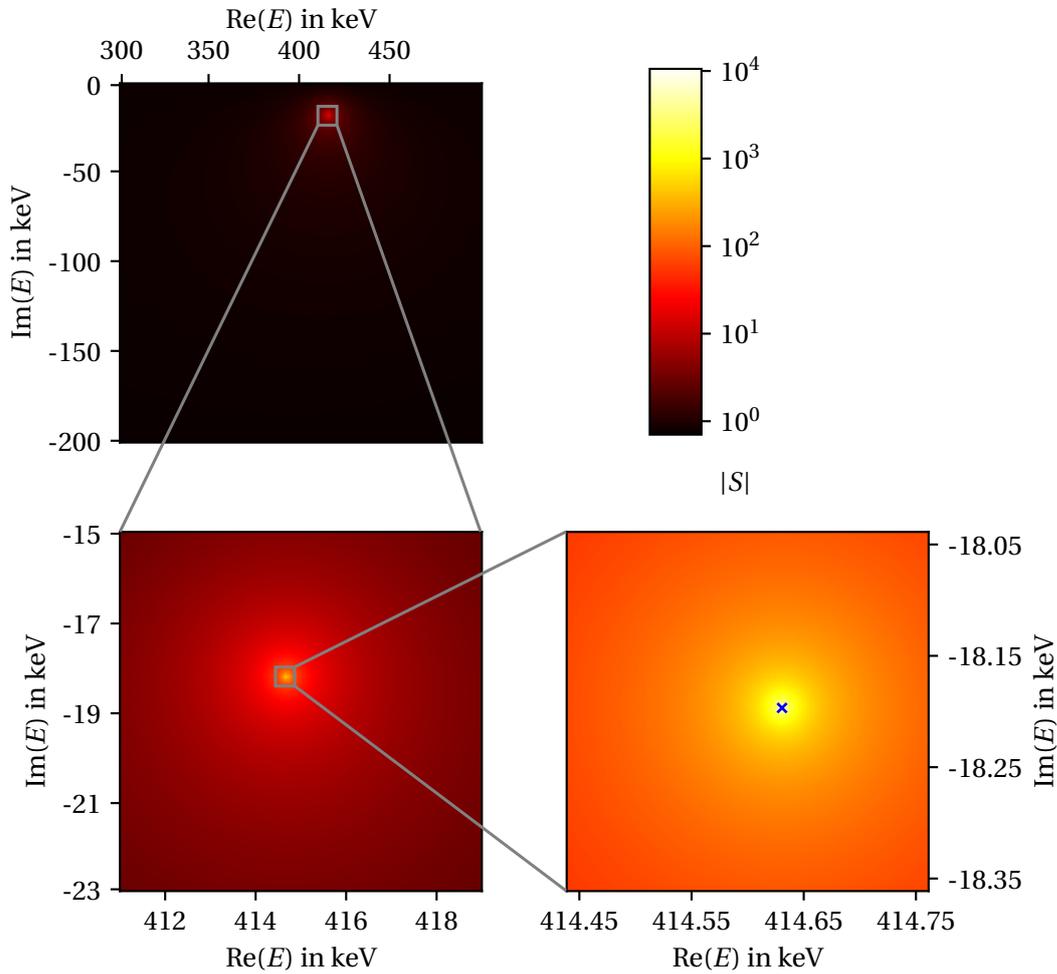
FIGURE 5.1.: Scheme of the pole search in the absolute value of the S-matrix for the
^{12}C+p scattering toy potential in equation (5.3). The picture in the upper
left shows the pole serach on a coarse energy grid. The region around
the pole is iterated up to an uncertainty of $|\Delta E| < 0.1$ keV is reached. The
blue cross in the lower right picture shows the final value of the resonance
energy at $E = (414.63 - 18.19i)$ keV.

5.3. Partial-Wave Selection

As a final step towards the Gamow basis it is necessary to decide which partial waves are
represented in the Berggren basis and which in the HO basis. The notation for the partial

waves in the Berggren basis specifies the orbital angular momentum, total angular momentum and isospin projection quantum numbers in the form $l_j^{m_t}$, e.g., the s-wave partial wave of neutrons is denoted via $s_{1/2}^{\mathrm{n}}$, where m_t describes protons (p) and neutrons (n). The radial quantum number in Gamow basis is denoted by ν and the maximum radial number in the Berggren partial waves is given by

$$\nu_{\max} = \nu_{\mathrm{b}} + \nu_{\mathrm{r}} + \nu_{\mathrm{s}} \tag{5.7}$$

with the total number of bound states ν_{b}, resonance states ν_{r}, and scattering states ν_{s}. All partial waves that are not denoted to use the Berggren single-particle basis use the HO single-particle basis. The HO single-particle basis is truncated by a maximum energy quantum number $e_{\max}$ and a maximum orbital angular momentum $l_{\max}$. The structure of the Gamow basis is highly dependent on the selection of Berggren and HO partial waves. Its effect on the results for the many-body resonance energy has to be investigated later on. Since the final many-body resonance state is highly correlated, it is not always possible to determine an optimal single-particle Gamow basis *a priori*.

In order to get an idea of how to partition the Berggren and HO partial waves, we consider an example. From experimental observations we know that the many-body resonance ground state of ^{4}H has the quantum numbers $J^\pi = 2^-$, which allows the assumption that it is primarily composed of a ^{3}H core and a loosely bound neutron in the $p_{3/2}$ shell. Therefore, we expect that the $p_{3/2}^{\mathrm{n}}$ partial wave is the most relevant partial wave for the inclusion of the continuum in the Berggren basis. We can parametrize the one-body potential such that it generates a single-particle resonance in the $p_{3/2}^{\mathrm{n}}$ partial wave. The nuclear potential given in equation (5.1) produces a single-particle resonance state at

$$E_{\mathrm{r}} = (1.05 - 0.99\mathrm{i})\,\mathrm{MeV}, \tag{5.8}$$

$$k_{\mathrm{r}} = (0.28 - 0.11\mathrm{i})\,\mathrm{fm}^{-1} \tag{5.9}$$

for the parameter values $V_{WS} = -20\,\mathrm{MeV}$, $V_{LS} = -25\,\mathrm{MeV}$, $a_{\mathrm{WS}} = 0.67\,\mathrm{fm}$ and $R_{\mathrm{WS}} = 2.02\,\mathrm{fm}$. The position of the resonance is depicted in figure 5.2.

Furthermore, we have to set a contour path for the partial waves using the Berggren basis. In case there exist only bound states in the partial wave, we use a contour along the real axis up to the cutoff $k_{\max}$ and use an equidistant grid for the discretized scattering states. For the
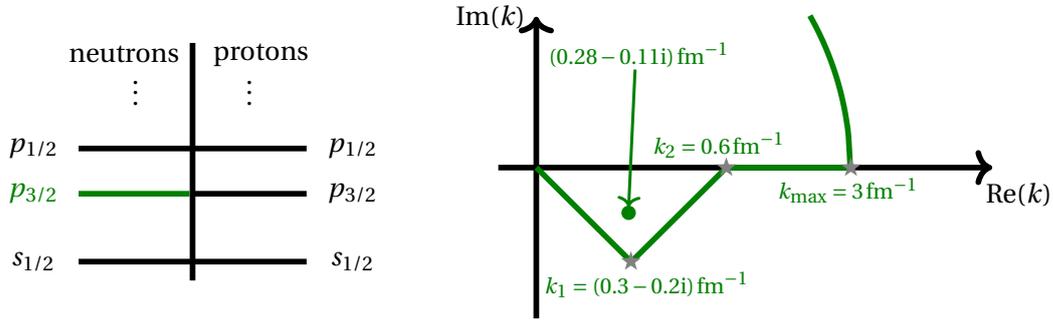
FIGURE 5.2.: Schematic selection of the HO and Berggren partial waves in case of an example for the description of the ground state of ^{4}H. The left side of the figure shows the first partial waves for protons and neutrons. Colored partial waves represent the use of the Berggren basis and black partial waves represent HO partial waves. The plot on the right side shows the single-particle resonance energy (●) and the chosen contour with its anchor points (★).

partial waves including resonance states, we choose the contour by the approximate rule

$$\text{Re}(k_1) \approx \text{Re}(k_r), \tag{5.10}$$

$$\text{Im}(k_1) \approx 2\text{Im}(k_r), \tag{5.11}$$

$$k_2 \approx 2\text{Re}(k_r). \tag{5.12}$$

where k_1 is the complex momentum in the fourth quadrant of the complex momentum plane, k_2 is the real momentum at which the contour becomes the real momentum axis again. We discretize each part of the path with a third of the total number of scattering states. For the example we use the following contour parameters

$$k_1 = (0.3 - 0.2\text{i})\,\text{fm}^{-1}, \tag{5.13}$$

$$k_2 = 0.6\,\text{fm}^{-1}, \tag{5.14}$$

$$k_{\max} = 3\,\text{fm}^{-1} \tag{5.15}$$

for the $p_{3/2}^n$ partial wave. For the number of discretized scattering states for each path we use

$$
\left.
\begin{aligned}
(0+0\mathrm{i})\,\mathrm{fm}^{-1} &\rightarrow k_1 \\
k_1 &\rightarrow k_2 \\
k_2 &\rightarrow k_{\max}
\end{aligned}
\right\} \frac{\nu_s}{3}. \tag{5.16}
$$

In order to fulfill this discretization procedure, we choose suitable values for ν_s in the following.

5.4. Radial Wave Functions

The next step to the Gamow basis is the calculation of the respective wave functions, more precisely the radial wave functions. As previously stated we use the R-matrix method introduced in chapter 4 to calculate the wave functions. In this section we take a closer look at the characteristics of bound, resonance and scattering wave functions. Furthermore, we investigate two parameters which emerge in the R-matrix approach, namely the channel radius R_c and the mesh size N in the internal region.

In figure 5.3, we show the wave functions of a single-particle bound, resonance and scattering state calculated for the neutrons of ^{4}H with the potential parameters from the example given in the previous section. In the $s_{1/2}^n$ partial wave the one-body potential has a bound state at an energy of $E = -3.35\,\mathrm{MeV}$. The normalized radial wave function $u(r)$ has a large amplitude for short distances and falls off towards zero at a finite range of $\sim 8\,\mathrm{fm}$. For a channel radius of $R_c = 8\,\mathrm{fm}$ the wave function has a small discontinuity in the derivative at the channel radius. This is a consequence of the fact that we do not solve the Bloch-Schrödinger equation (4.9) iteratively, but rather choose values for the channel radius that are large enough such that the wave function has fallen off towards zero at the channel radius as discussed in section 4.2. For a larger channel radius of $R_c = 10\,\mathrm{fm}$ this problem is eliminated. The scattering state for $\nu = 4$ in the same partial wave with an energy of $E = 2.98\,\mathrm{MeV}$ has an oscillating wave function with a constant amplitude in the external region. The weights of the scattering wave function are characterized by the number of scattering states $\nu_s = 24$. The resonance state in the $p_{3/2}^n$ partial wave is located at an energy of $E = (1.05 - 0.99\mathrm{i})\,\mathrm{MeV}$, which is a very broad resonance. It shows a large amplitude at distances between $5\,\mathrm{fm}$ and $10\,\mathrm{fm}$ and starts to oscillate afterwards.

All radial wave functions are converged for a channel radius of $R_c = 10\,\mathrm{fm}$ and a mesh size of $N = 100$ and we use these parameter values in all following calculations. The dependence
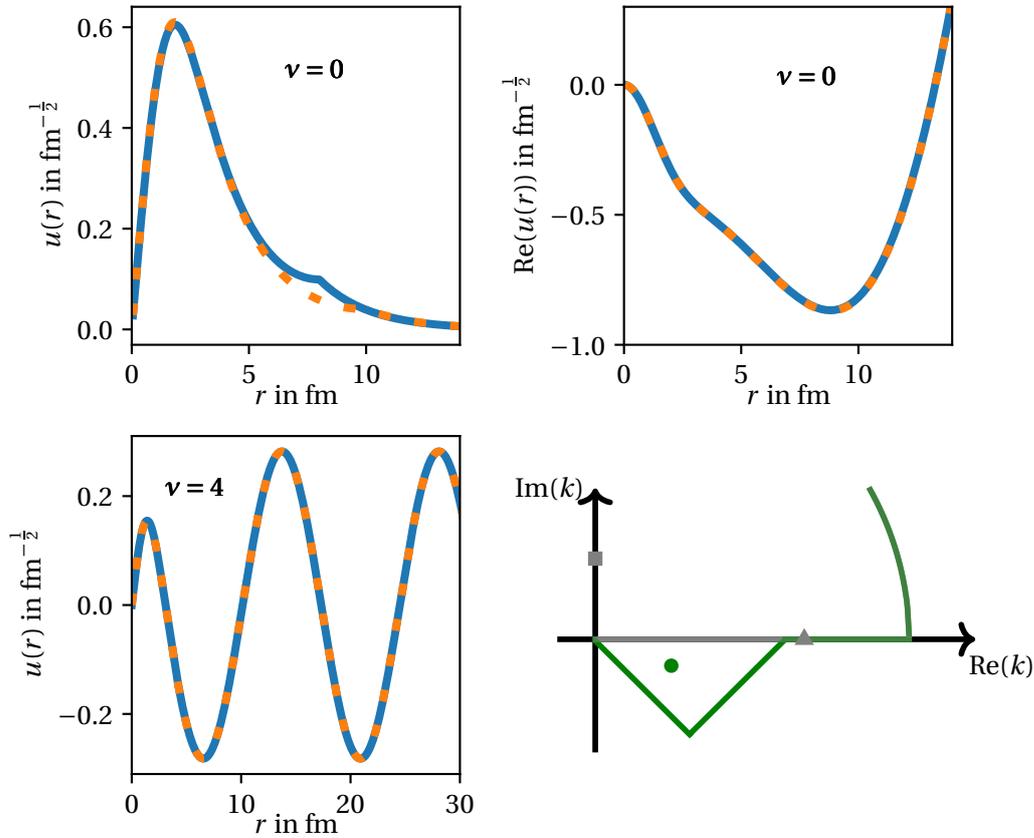
FIGURE 5.3.: Analysis of the dependence of the wave function of a bound (upper left), resonance (upper right) and scattering (lower left) wave function for N mesh points and the channel radius R_c using the R-matrix approach. The lines correspond to $N = 50$, $R_c = 8\,\mathrm{fm}$ (——) and $N = 100$, $R_c = 10\,\mathrm{fm}$ (– –). The scheme in the lower right shows a possible choice for the contours for the $s^n_{1/2}$ partial wave (——) containing the bound (■) and the scattering state (▲) and the $p^n_{3/2}$ partial wave (——) containing the resonance state (●). The potential parameters are given in section 5.3. The scattering contour is discretized with $\nu_s = 24$ points and the momentum cutoff is at $k_{\max} = 3\,\mathrm{fm}^{-1}$.

of the final results in the GNCSM calculation on the number contour discretization points of $\nu_s = 24$ and the momentum cutoff for the contour at $k_{\max} = 3\,\mathrm{fm}^{-1}$ needs to be checked later, since both parameters influence the structure of the single-particle basis.

5.5. Cheat Sheet: Gamow Basis Setup

The first part of the GNCSM framework development is finished. Many of the existing parameters and truncations in the GNCSM framework already appeared at the setup of the Gamow basis. For some truncations we were already able to determine converged values. The convergence of the remaining truncations and the impact of the parameters that vary the structure of the Gamow basis will be discussed for the first GNCSM calculations later on. All truncations that appear in this chapter can be systematically increased in order to obtain converged results.

Gamow basis	Parameters	Truncations
1.) Define one-body potential	V_{WS}, V_{ls}, a_{WS}, R_{WS}	
2.) Choose BG/HO partial waves		$l_j^{m_t}$, e_{max}, l_{max}
3.) Set contour path	k_1, k_2	k_{max}, ν_{s}
4.) R-matrix calculation		$N = 100$, $R_{\mathrm{c}} = 10\,\mathrm{fm}$

6

CALCULATION OF MATRIX ELEMENTS

Matrix elements represent the relevant input to the GNCSM as they are needed to calculate the matrix representation of the nuclear Hamiltonian. Thus, the information on the single-particle basis is encoded in the nuclear matrix elements. In the standard NCSM using the HO basis, the matrix elements of the kinetic energy can be calculated analytically in the HO basis. The matrix elements of realistic interactions derived from χEFT are calculated in a relative momentum basis and the transformation coefficients to the relative HO basis as well as the m-scheme HO basis are known analytically. If we use a different orthonormal single-particle basis, e.g., the natural-orbital basis, we can calculate a finite number of transformation coefficients numerically and transform the matrix elements into the new single-particle basis.

The main problem arising with the inclusion of Berggren partial waves is that we cannot calculate nuclear matrix elements containing resonance and scattering states directly due to their infinite range. However, it is possible to calculate the nuclear matrix elements using the basis expansion in HO single-particle states. This induces additional effort which we discuss in the following. We start with the calculation of the HO expansion coefficients for bound, resonance, and scattering states in the Berggren basis. With these HO coefficients we can define two procedures to calculate the matrix elements of the interaction and the kinetic energy of the complete Gamow basis, respectively.

6.1. Wave Function Expansion

The HO expansion coefficients of the Berggren states are calculated in coordinate space using the overlap of the HO single-particle states with the Berggren states given by

$$\left\langle u^{\mathrm{HO}}_{nljm_jm_t} \middle| u^{\mathrm{BG}}_{vl'j'm_{j'}m_{t'}} \right\rangle \approx \delta_{ll'}\delta_{jj'}\delta_{m_jm_{j'}}\delta_{m_tm_{t'}} \int_0^{R_{\mathrm{cut}}} u^{\mathrm{HO}}_{nljm_jm_t}(r) u^{\mathrm{BG}}_{vljm_jm_t}(r)\,dr = C^{(ljm_jm_t)}_{vn}.$$

(6.1)

For the radial integral, we use a cutoff R_{cut}, which is necessary to ensure the numerical stability as we discuss in the next section. The superscripts of the HO coefficients C indicate the diagonal quantum numbers, i.e., l, j, m_j and m_t. The Kronecker deltas originate from the symmetries of the one-body potentials for both basis sets. The potentials are diagonal in the spin and isospin parts and are spherical symmetric, which translates to diagonal j and m_j quantum numbers in a j-coupled basis set. For simplicity, we omit the diagonal quantum numbers in the following derivations. The subscripts indicate the non-diagonal quantum numbers, i.e., the radial quantum number n in the HO basis and the quantum number v in the Berggren partial waves of the Gamow basis. The complete set of HO coefficients for the Gamow basis are given by

$$C_{vn} = \begin{cases} \left\langle u^{HO}_n \middle| u^{HO}_v \right\rangle = \delta_{vn} & \text{HO partial wave,} \\ \left\langle u^{HO}_n \middle| u^{BG}_v \right\rangle & \text{BG partial wave.} \end{cases}$$

(6.2)

First, we take a look at the HO expansion coefficients and the corresponding wave function in figure 6.1. The left column shows the expansion coefficients of a bound, a resonance and a scattering state for different HO frequencies. The coefficients of the bound state are converged to zero at $n \approx 12$. In case of resonance and scattering states the expansion coefficients behave differently. Even though the coefficients for smaller HO radial quantum numbers are larger, the expansion coefficients do not converge towards zero, hence, their contribution to the expansion wave function and the norm is not negligible. In this case, we need to take a closer look at the convergence of the respective matrix elements containing resonance or scattering states and need to ensure that the matrix element transformation is converged for a maximum number of HO coefficients n_{max}.

If we take a look at the right-hand side of the figure 6.1, we show the expanded wave functions for $e_{\mathrm{max}} = 24$. This is the maximum single-particle quantum number that we can use for the expansion of the matrix elements of the nuclear interaction later. In case of the bound state, the original wave function from the R-matrix method is described very well
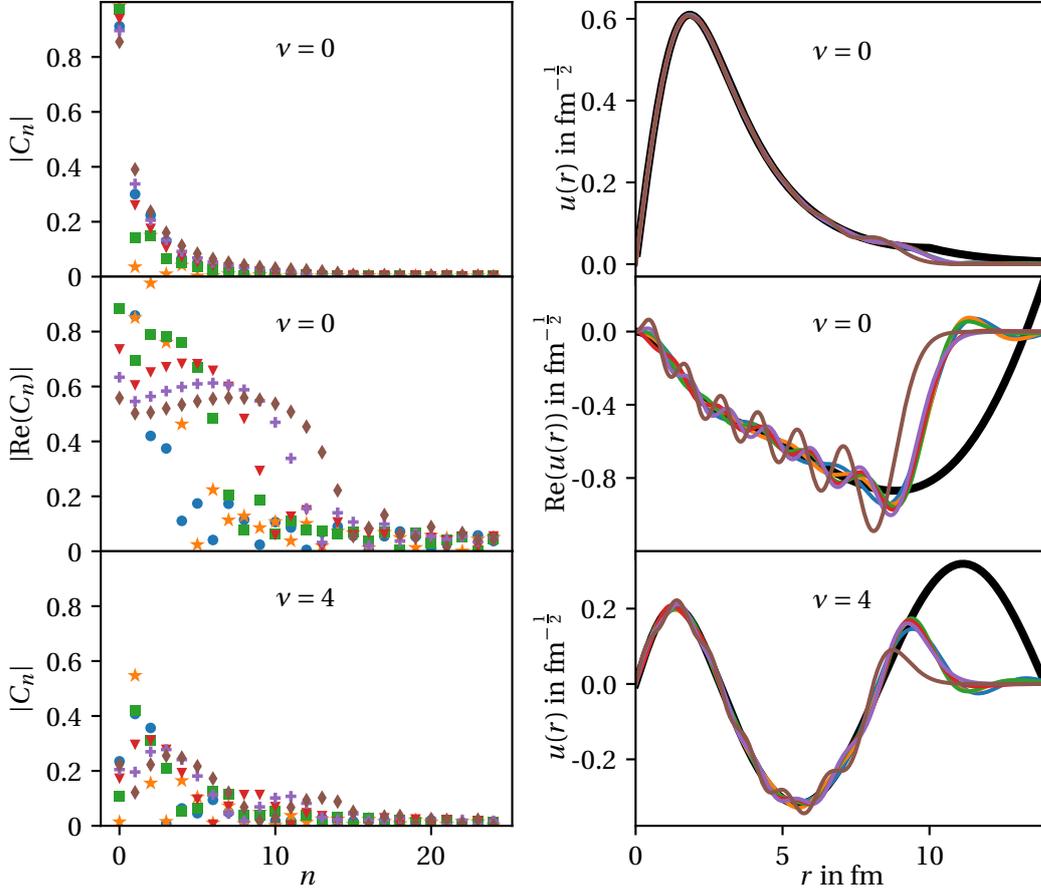
FIGURE 6.1.: The left column shows the expansion coefficients in the HO basis depending on the HO radial quantum number n and the HO frequencies 4 MeV (●), 8 MeV (★), 12 MeV (■), 16 MeV (▼), 20 MeV (✚) and 24 MeV (◆) for the same bound, resonance and scattering state as in figure 5.3. The right column shows the exact wave function from the R-matrix method (▬) and the expanded wave functions for the HO frequencies 4 MeV (▬), 8 MeV (▬), 12 MeV (▬), 16 MeV (▬), 20 MeV (▬) and 24 MeV (▬). The wave functions correspond to $e_{max} = 24$, i.e., $n_{max} = 12$ for the bound and scattering wave function and $n_{max} = 11$ for the resonance wave function. The cutoff is set to $R_{cut} = 10$ fm.
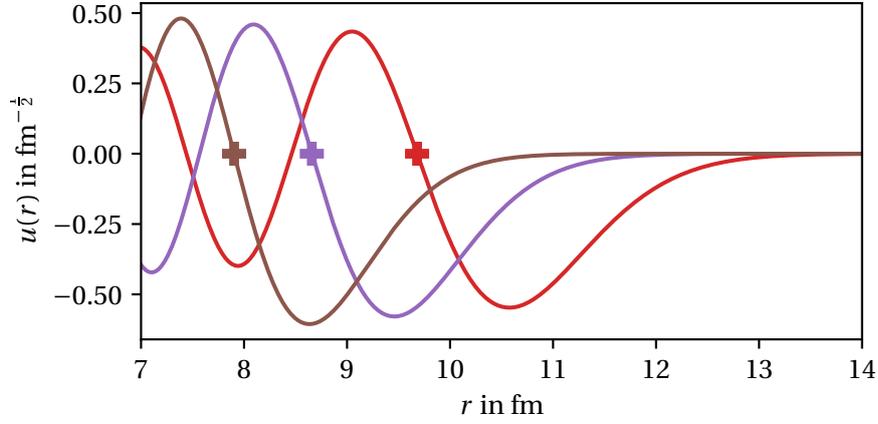
FIGURE 6.2.: Representation of the HO wave functions with $n = 11$ and $l = 1$ for the HO frequencies 16 MeV (━━), 20 MeV (━━) and 24 MeV (━━). The last node of the wave functions is marked (✚).

for the short-range part. The tail of the bound wave function is regulated by the HO wave functions implicitly. For the resonance and the scattering state, the overall agreement up to $R_{\text{cut}} = 10\,\text{fm}$ is good as well, however, the oscillation artifacts from the HO wave functions are still visible. The effect of the radial cutoff is visible for the resonance wave functions. For all HO frequencies except for the HO frequency of 24 MeV, the wave functions fall off towards zero at the same distance, i.e. the value of the radial cutoff. In case of the HO frequency of 24 MeV, the range of the wave function is shorter than the radial cutoff, hence the HO wave functions regulate the expanded wave function implicitly. We can explain this behavior if we take a look at figure 6.2. It shows the HO wave function for $n = 11$ and $l = 1$ which is the broadest wave function we can use for the expansion of interaction matrix elements. Thus, the range of the expanded wave function is limited by the broadest HO wave function and, additionally, the expansion becomes unstable for short distances if

$$\max\left[x_0\left(n_{\max}\right)\right] < R_{\text{cut}} \tag{6.3}$$

where $x_0\left(n_{\max}\right)$ is the set of node positions for the broadest HO wave function. The positions of the nodes are important because they characterize the maximum range of the expanded wave function. The range and quality of the HO expansion can be increased with contributions of waves with higher radial quantum numbers, but as already mentioned, for the calculation of interaction matrix elements we are limited to single-particle energy quantum
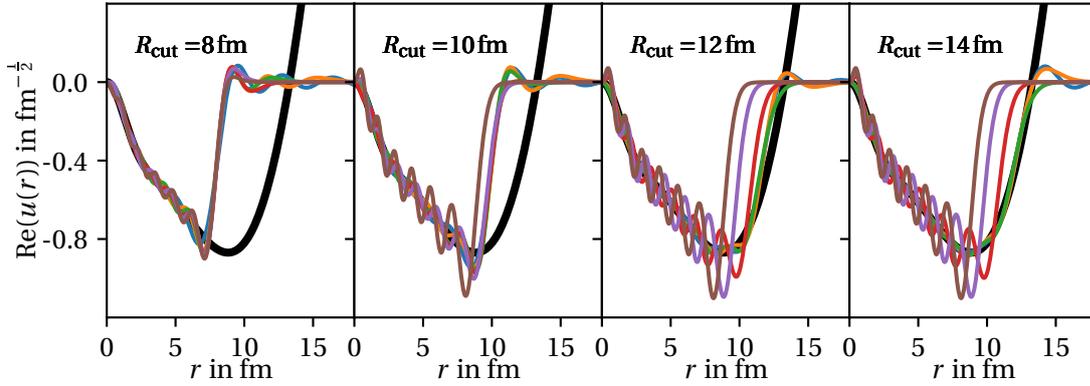
FIGURE 6.3.: Dependence of the expanded wave function on the cutoff value R_{cut} for the real part of the resonance wave function from figure 5.3. The plots show the initial wave function from the R-matrix method (—) and the expanded wave functions for the HO frequencies 4 MeV (—), 8 MeV (—), 12 MeV (—), 16 MeV (—), 20 MeV (—) and 24 MeV (—). The wave functions correspond to $n_{\text{max}} = 11$.

numbers of $e_{\text{max}} = 24$ which translates to the radial quantum numbers $n_{\text{max}} = 11, 12$ for p- and s-wave orbits, respectively.

The influence of R_{cut} on the real part of the previous resonance wave function is depicted in figure 6.3. The quality of the expansion using a HO basis decreases significantly if the value of the cutoff parameter exceeds the range of the HO wave functions and equation 6.3 is not fulfilled. For the HO frequency of 16 MeV and $n = 11$ the wave functions fall off to zero at about 13 fm and the last node has a value of about 10 fm. The expansion is unable to describe the complete wave function properly beyond the last node and the overall quality of the expansion is decreased because the expansion becomes numerically unstable. The dependence of the values for the matrix elements on the cutoff R_{cut} is investigated in the next section.

6.2. Interaction Matrix Elements

As we have seen in the previous section, the expansion in the HO basis is only able to represent the short-range part of resonance and scattering wave functions. In case of interaction matrix elements this is not too problematic, because we can make use of the finite range R of a

nuclear potential. This means that the expansion of the wave function using a finite number of HO wave functions can be sufficient because the potential ultimately regulates the matrix elements [HHM06; Mic+08; Pap+13]. A schematic representation of the radial part of a matrix element of a local two-body interaction $V(r)$ shows

$$
\begin{aligned}
\langle u_1 u_2 | \hat{V}_{\mathrm{NN}} | u_3 u_4 \rangle \propto \int_0^R & u_1(r_1) u_2(r_2) V(r) u_3(r_3) u_4(r_4) \\
& \times \delta(r - (r_4 - r_3)) \delta(r - (r_2 - r_1)) dr_1 dr_2 dr_3 dr_4.
\end{aligned}
\tag{6.4}
$$

We do not have to expand the entire wave function but only the part of the wave functions where the potential does not vanish. Note, this is only a schematic illustration and motivation to use a HO expansion for the calculation of the interaction matrix elements. This illustration has two weaknesses: First, we are not able to derive a local coordinate representation of the realistic interactions derived from χEFT that we use in this thesis. The radial dependence of the interaction matrix elements is represented in a non-trivial way in the HO single-particle states. Second, it is possible to have two large absolute coordinates r_1 and r_2 with a small relative coordinate $r = r_1 - r_2$, where the potential does not vanish. When we calculate the matrix elements in the Gamow basis we have to make sure that the expanded matrix elements are converged with respect to the cutoff R_{cut} for the HO expansion of the single-particle states and the maximum single-particle energy e_{max}.

The expansion of a J-coupled two-body matrix element in the Gamow basis in matrix elements of the HO basis reads

$$
\langle (\alpha\beta) J M_J | \hat{V}_{\mathrm{NN}} | (\gamma\delta) J M_J \rangle \approx \sum_{\substack{n_a, n_b, \\ n_c, n_d = 0}}^{n_{\mathrm{max}}} C_{\nu_\alpha n_a} C_{\nu_\beta n_b} C_{\nu_\gamma n_c} C_{\nu_\delta n_d} \langle (ab) J M_J | \hat{V}_{\mathrm{NN}} | (cd) J M_J \rangle, \quad (6.5)
$$

where the greek letters correspond to the set of Gamow single-particle quantum numbers, i.e., $\alpha = \{ \nu_\alpha l_\alpha j_\alpha m_{t_\alpha} \}$ and the latin letters correspond to a set of HO single-particle quantum numbers, i.e., $a = \{ n_a l_a j_a m_{t_a} \}$. The expansion only affects the radial quantum number, which is truncated by the maximum radial quantum number n_{max}. The expansion coefficients are given by equation (6.2).

Before we analyze the convergence of the expanded interaction matrix elements on a small set of matrix elements, we need to fix an interaction for our calculations. For the remaining part of the development of the GNCSM we use the same chiral interaction that was used in chapter 2. It is a two-body interaction by Entem, Machleidt and Nosyk at fourth order with a regulator cutoff of $\Lambda = 500\,\mathrm{MeV}$ [EMN17]. The interaction is SRG evolved with a flow parameter of $\alpha = 0.08\,\mathrm{fm}^4$ [BFP07; RRH08].
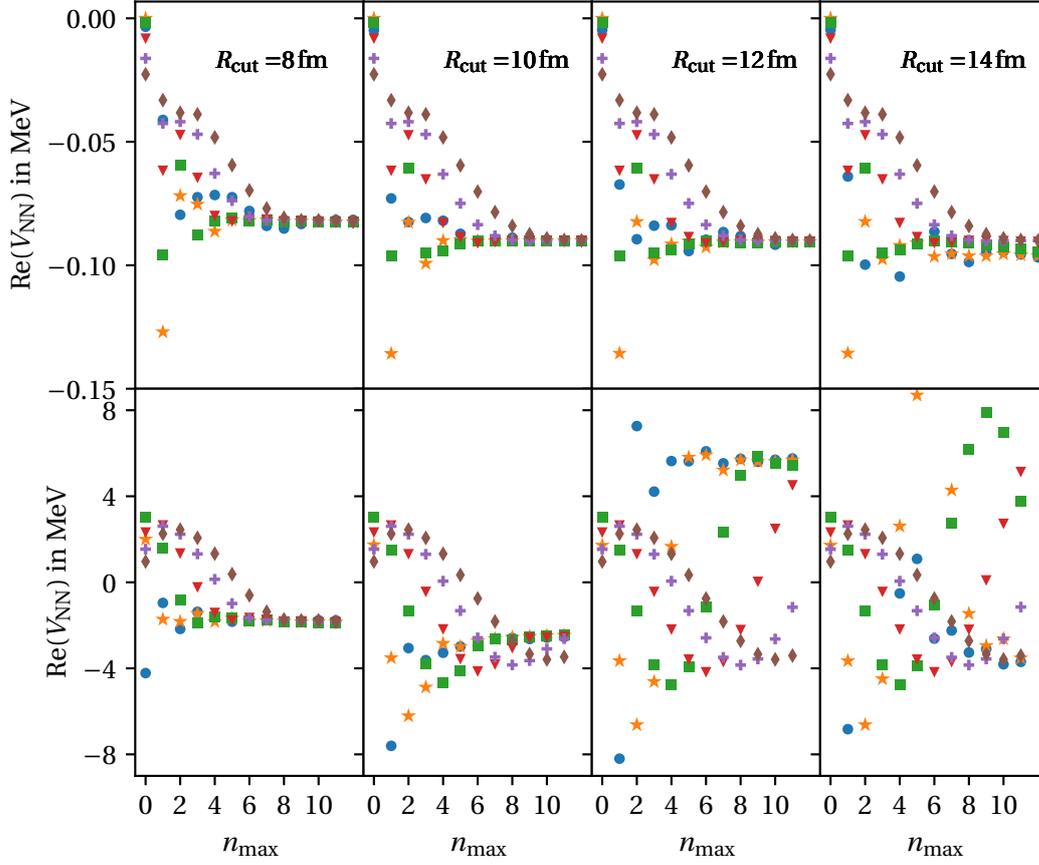
FIGURE 6.4.: Convergence of the expanded diagonal interaction matrix elements in dependence on the HO expansion parameter n, the radial integral cutoff R_{cut} and the HO frequencies 4 MeV (●), 8 MeV (★), 12 MeV (■), 16 MeV (▼), 20 MeV (✚) and 24 MeV (◆). The rows show the matrix elements defined in equation (6.6) and (6.7), respectively.

Since it is impossible to analyze the convergence of every single interaction matrix element, we take a look at two diagonal matrix elements first in order to investigate the R_{cut} dependence in figure 6.4. For the first row we use the single-particle scattering state

$$\alpha = \beta = \gamma = \delta = \left\{ 4, 0, \frac{1}{2}, -\frac{1}{2} \right\}, \ J = M_J = 0 \tag{6.6}$$

and for the second row we use the single-particle resonance state

$$\alpha = \beta = \gamma = \delta = \left\{ 0, 2, \frac{3}{2}, -\frac{1}{2} \right\}, \; J = M_J = 0, \tag{6.7}$$

which are shown in figure 6.1.

For $R_{\mathrm{cut}} = 8 \, \mathrm{fm}$ the values for both matrix elements converge towards the same value for all HO frequencies. Similarly, for $R_{\mathrm{cut}} = 10 \, \mathrm{fm}$ the values converge to the same value for all HO frequencies in the first row. However, the converged value does not coincide with the converged value for the cutoff of $R_{\mathrm{cut}} = 8 \, \mathrm{fm}$. This means that the interaction has a contribution even at these distances. For the matrix element in the second row, the two largest HO frequencies are not converged at $n_{\max} = 11$.

If we increase the radial cutoff to $R_{\mathrm{cut}} = 12 \, \mathrm{fm}$, the matrix element in the first row converges to the same value as the previous cutoff. This does not hold for the matrix element in the second row. The expansion of the matrix elements becomes unstable and yields different results for almost every frequency. This effect becomes also visible for the matrix element in the first row at $R_{\mathrm{cut}} = 14 \, \mathrm{fm}$. The origin of these unstable convergence patterns are the following: First, the calculation of the HO expansion coefficients becomes unstable if the radial wave functions of the HO fall off towards zero. Second, the deviation of expanded wave functions from the exact wave function increases for short distances if we use larger radial cutoffs.

Since we expect that the interaction matrix element are mainly effected by the short-range part of the wave function, this also decreases the quality of the matrix element expansion. Hence, we have to make sure that the cutoff value is large enough such that we do not exclude parts of the interaction and small enough such that the expansion still converges to the same value for all frequencies. In the following, the default value for the cutoff radius is $R_{\mathrm{cut}} = 10 \, \mathrm{fm}$. From the analysis of the second row, we also know that we should not use HO frequencies that are larger than $\hbar\Omega = 16 \, \mathrm{MeV}$ for this Gamow basis. We investigate the uncertainty of the final many-body result generated by the matrix element expansion in chapter 7. Note, we only use the Gamow basis for the calculation of a reference state for the following natural orbital calculation and the impact on the natural orbitals might be small.

As a further analysis, figure 6.5 shows three off-diagonal matrix elements containing the bound, resonance and scattering states from figure 6.1. From the left to the right, the value of the matrix elements correspond to the off-diagonal matrix element for the bound and
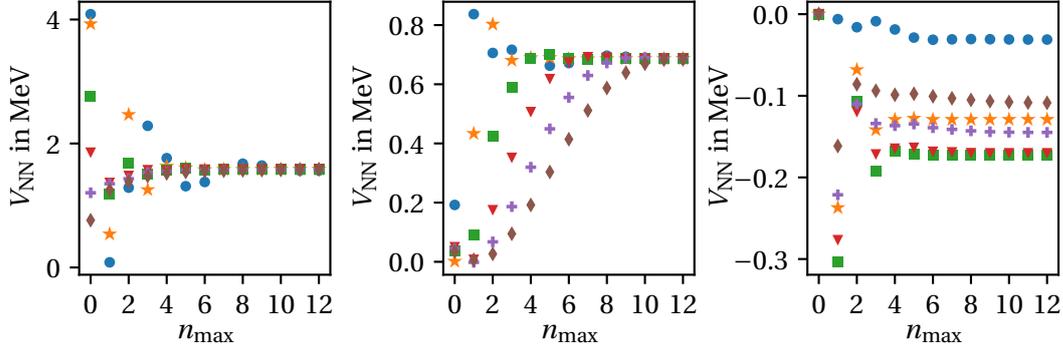
FIGURE 6.5.: Convergence of the approximation of off-diagonal interaction matrix elements in dependence on the HO expansion parameter n and the HO frequencies 4 MeV (●), 8 MeV (●), 12 MeV (●), 16 MeV (▼), 20 MeV (✚) and 24 MeV (♦). For the information on the single-particle states of the matrix elements see the text.

resonance states

$$\alpha = \beta = \left\{ 0, 2, \frac{3}{2}, -\frac{1}{2} \right\}, \ \gamma = \delta = \left\{ 0, 0, \frac{1}{2}, -\frac{1}{2} \right\}, \ J = M_J = 0, \tag{6.8}$$

the resonance and scattering states

$$\alpha = \beta = \left\{ 0, 2, \frac{3}{2}, -\frac{1}{2} \right\}, \ \gamma = \delta = \left\{ 4, 0, \frac{1}{2}, -\frac{1}{2} \right\}, \ J = M_J = 0, \tag{6.9}$$

and the scattering state with two different HO states

$$\alpha = \left\{ 1, 0, \frac{1}{2}, \frac{1}{2} \right\}, \gamma = \left\{ 0, 0, \frac{1}{2}, \frac{1}{2} \right\}, \beta = \delta = \left\{ 4, 0, \frac{1}{2}, -\frac{1}{2} \right\}, J = M_J = 0. \tag{6.10}$$

The first two matrix elements converge to the same value for all HO frequencies similar to the diagonal matrix elements. The last matrix element is a little different and demonstrates an important characteristic of the HO wave functions. First, since the HO wave functions depend on the HO frequency, the matrix element converges to different values. Second, the matrix elements containing HO states are usually converged because the HO wave functions fall off to zero at finite distances. Thus, the matrix elements that cause the most problems are the matrix elements only containing resonance or scattering states. In this case the expansion of the matrix element is regulated by the maximum radial quantum number $n_{\max}$ and can yield results that are not converged.

6.3. Kinetic Energy Matrix Elements

For the calculation of the many-body kinetic energy matrix elements we use the representation of the kinetic energy operator given in equation (1.4). We use different approaches to calculate the two parts of the kinetic energy operator. Since the one-body part contains most of the information and the two-body operator is a correction to the one-body part, we assume that the correction is less important. Thus, we use the same approach of a HO basis approximation as already used for the two-body interaction in the previous section in order to calculate the two-body part of the kinetic energy operator. The one-body part is calculated directly from the results of the R-matrix method as discussed in the following.

One-Body Part   For the R-matrix calculation, we chose the kinetic energy operator to be the one-body part of the many-body kinetic energy. We obtain the one-body part of the many-body kinetic energy using the one-body Schrödinger equation

$$\left(\hat{T} + \hat{V}_{\mathrm{N}} + \hat{V}_{\mathrm{C}}\right)|u_i\rangle = E\,|u_i\rangle \tag{6.11}$$

where $\hat{V}_{\mathrm{N}}$ and $\hat{V}_{\mathrm{C}}$ are the nuclear potential and the Coulomb potential defined in the R-matrix method and E is the energy of the state $|u_i\rangle$. If we rearrange the equation and multiply by a bra state $\langle\tilde{u}_j|$, we obtain

$$\langle\tilde{u}_j|\hat{T}|u_i\rangle = \langle\tilde{u}_j|E - \hat{V}_{\mathrm{N}} - \hat{V}_{\mathrm{C}}|u_i\rangle. \tag{6.12}$$

The right-hand side of the equation can be calculated in coordinate space using the wave functions from the R-matrix

$$\langle\tilde{u}_j|\hat{T}|u_i\rangle = E\,\delta_{ij} - \int_0^R \left(V_{\mathrm{N}}(r) + V_{\mathrm{C}}(r)\right)u_j(r)u_i(r)dr. \tag{6.13}$$

The cutoff value is set to $R = 20\,\mathrm{fm}$, which yields converged results.

Two-Body Part   Since it is not possible to calculate the exact two-body matrix element using the wave functions from the R-matrix method, we use the same approximation to the two-body part of the matrix element as we have used for the interaction matrix elements. The kinetic energy operator is not spatially confined like the interaction. Thus, the calculation of the matrix element is not regulated by the operator. However, we assume that the main part of the kinetic energy information is included in the one-body part of the operator and the two-body matrix elements are a correction to the one-body part. The results for the approximation of two off-diagonal matrix elements of the two-body part of the kinetic energy
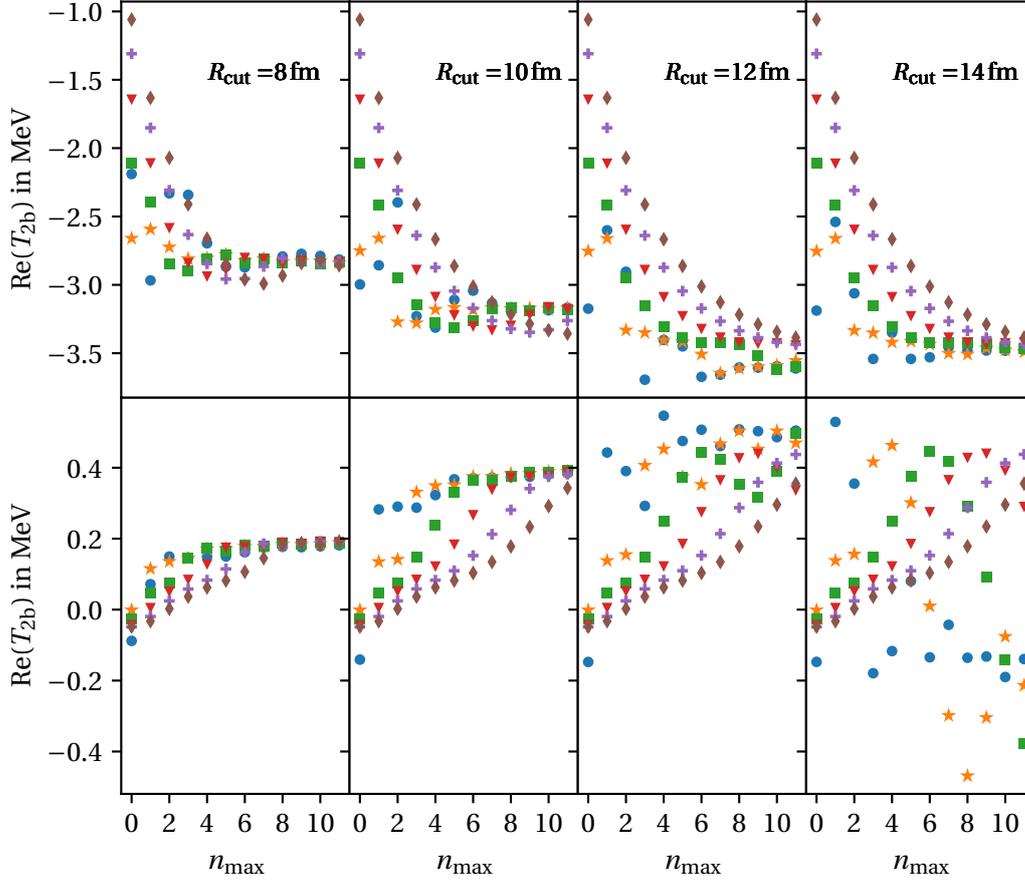
FIGURE 6.6.: Convergence of the approximation of off-diagonal kinetic energy matrix elements in dependence on the HO expansion parameter n, the radial integral cutoff R_{cut} and the HO frequencies 4 MeV (●), 8 MeV (●), 12 MeV (●), 16 MeV (▼), 20 MeV (✚) and 24 MeV (♦). The rows show the matrix elements defined in equation (6.8) and (6.9), respectively.

operator are shown in figure 6.6 in dependence on the cutoff parameter R_{cut}. The first row shows the matrix element for the bound and resonance states

$$\alpha = \beta = \left\{0, 2, \frac{3}{2}, -\frac{1}{2}\right\}, \gamma = \delta = \left\{0, 0, \frac{1}{2}, -\frac{1}{2}\right\}, J = M_J = 0, \tag{6.14}$$

and the second row shows the matrix elements of the scattering and resonance states

$$\alpha = \beta = \left\{0, 2, \frac{3}{2}, -\frac{1}{2}\right\}, \gamma = \delta = \left\{4, 0, \frac{1}{2}, -\frac{1}{2}\right\}, J = M_J = 0, \tag{6.15}$$

shown in figure 6.1. The value of the first matrix element converges for all HO frequencies and radial cutoffs. This is a consequence of the finite bound-state wave function in the matrix element. For the second matrix element, the situation is similar to the interaction matrix element using the resonance state. The results converge towards the same value for all HO frequencies at $R_{\text{cut}} = 8\,\text{fm}$. For $R_{\text{cut}} = 10\,\text{fm}$ the converged values differ for the largest HO frequency. If we increase the radial cutoff even further, the results become unstable.

6.4. Cheat Sheet: Calculation of Nuclear Matrix Elements

The calculation of the nuclear matrix elements generates the first truncations that we are not always able to converge. For the approximation of the interaction matrix elements, we only have access to matrix elements up to $e_{\text{max}} = 24$ in the HO basis. In order to include as much information from the HO matrix elements, but still remain numerically robust, it is necessary to tune and optimize the cutoff of the radial integral in the expansion of the Berggren wave functions and define a set of HO frequencies that yield converged matrix elements. The optimal value for this cutoff and the set of suitable HO frequencies differs for different parameters of the Gamow basis. An important characteristic of the Gamow basis is that it is non-orthonormal which entails a problem for the GNCSM calculation as we will see in the next chapter.

Matrix Elements	Parameters	Truncations
1.) Choose HO frequency	$\hbar\Omega$	
2.) Calculate HO approximation		$R_{\text{cut}} = 10\,\text{fm}$
3.) Calculate matrix elements		$e_{\text{max}} = 24$

7

GAMOW NO-CORE SHELL MODEL

The GNCSM extends the NCSM towards complex single-particle basis sets. The matrix elements calculated in the previous chapter form the essential input we need to perform these calculations. As already stated in the previous part, in the bra-ket notation the NCSM and the GNCSM are identical. However, it is still useful to take a look into the changes occurring using the complex Gamow basis. In the following section, we define the necessary extensions to the standard NCSM needed in order to perform GNCSM calculations. Afterwards, we can perform first calculations and investigate the parameters and truncations from the Gamow basis and the matrix element approximation.

7.1. Extensions towards the GNCSM

The necessary extensions to the GNCSM pull through all parts of the NCSM. Most of the changes only affect the formal definition of the already existing formula in the bra-ket notation. Therefore, we discuss the basic concepts (cf. section 2.1), the model space definition (cf. section 2.2) and the center-of-mass spuriousity (cf. section 2.3) of the standard NCSM again and point out the relevant changes that appear in the GNCSM.

Basic concept As we have already discussed in chapter 3 it is not possible to obtain complex valued observables in a Hilbert space and we have to replace the many-body Hilbert space by a rigged Hilbert space analogous to the one-body case for the Berggren basis. Using a

rigged Hilbert space entails two consequences. The first consequence concerns the formal structure of the many-body basis. The basis of Slater determinants $\{|\Phi\rangle\}$ fulfills the following completeness relation [Pap+13]

$$\hat{\mathbb{1}} = \sum_i |\Phi_i\rangle\langle\tilde{\Phi}_i|, \tag{7.1}$$

which is similar to equation (3.19). The tilde on the bra label wave function reflects the different definition of the scalar product in the rigged Hilbert space, similar to the scalar product for the single-particle Bergren states given in equation (3.16). The expansion coefficients of an eigenstates $|\Psi_n\rangle$ calculated in the GNCSM fulfill

$$\sum_i C_{ni}^2 = 1. \tag{7.2}$$

Note, the expansion coefficients C_{ni} become complex if we include resonances and complex scattering states to the Gamow basis. This behavior originates from the underlying single-particle states of the Gamow basis. The Slater determinant basis in a rigged Hilbert space results in a complex symmetric Hamilton matrix, which leads to the second consequence regarding the numerical algorithm and memory resources. Since the matrix eigenvalue problem becomes complex symmetric, the diagonalization method, i.e., the Lanczos method, has to be adjusted [And+99] and the memory requirements for the storage of the Hamilton matrix are doubled for complex values.

At this point we want to clarify the important change to the standard NCSM that leads to complex energy eigenvalues. It is necessary to use a complex symmetric Hamilton matrix in order to obtain complex energy eigenvalues. If we use a Hermitian matrix instead, we are still working in a standard Hilbert space and the eigenvalues of a Hermitian matrix are real.

Model Space   The standard NCSM is truncated solely by the N_{max} which is motivated by the intrinsic and center-of-mass separation of the many-body wave function. Furthermore, using the N_{max} truncation we expect that states with lower single-particle energies in the HO single-particle basis are more important. For the Berggren partial waves none of these properties hold. The inclusion of resonance and scattering states does not allow the use of the center-of-mass Hamiltonian from equation (2.10) in order to shift center-of-mass part excitations out of the low-energy spectrum. Additionally, the energies of the scattering states are not split equidistantly as for the HO basis such that the use of the N_{max} truncation has no physical motivation.

In the following, we define a new many-body truncation scheme, which truncates the HO partial waves and the Berggren partial waves separately. For the HO partial waves we keep the $N_{\max}$ truncation, which is indicated as $N_{\max}^{\mathrm{HO}}$. In case of the Berggren partial waves we use the number of scattering states occupied in a Slater determinant $S(|\Phi\rangle)$ and define a particle-hole truncation $S_{\max}$, which limits the number of scattering states allowed in the Slater determinants. The final model space definition is an extension from the standard definition in equation (2.8)

$$\mathcal{M}(N_{\max}^{\mathrm{HO}}, S_{\max}, M_J, \pi) = \big\{ |\Phi\rangle : N(|\Phi\rangle) \leq N_{\max}^{\mathrm{HO}},\ S(|\Phi\rangle) \leq S_{\max}, $$
$$M(|\Phi\rangle) = M_J,\ \pi(|\Phi\rangle) = \pi \big\}. \tag{7.3}$$

Note, the two truncations act on disjunct parts of the Gamow basis as $N_{\max}^{\mathrm{HO}}$ only acts on HO partial waves and $S_{\max}$ only acts on Berggren partial waves. Bound and resonance states in Berggren partial waves are always included in the model space.

A problem in the GNCSM is that the inclusion of Berggren partial waves produces an extreme increase of the many-body basis dimension with an increasing number of scattering states compared to the $N_{\max}$ truncation in the standard NCSM. It is necessary to discretize the contour with $v_{\mathrm{s}} \geq 15$ scattering states. Figure 7.1 shows a comparison in the many-body basis dimension for a set of light nuclei for a standard NCSM calculation and a GNCSM calculation, where the Berggren single-particle basis is used in one or two partial waves. The parameter $S_{\max}$ is always chosen at its maximum value such that all nucleons are allowed to occupy a scattering state. For instance, for ^{4}H with the $s_{1/2}^{\mathrm{n}}$ and $p_{3/2}^{\mathrm{n}}$ partial waves for neutrons we use $S_{\max} = 3$, such that all three neutrons can occupy a scattering state. We can see that the many-body basis dimension increases by one to two orders of magnitude in the GNCSM even for $v_{\mathrm{s}} = 20$ scattering points. These large basis dimensions complicate the GNCSM calculations on a few levels. First, the matrix elements are complex and, as a consequence, the memory use is doubled compared to standard NCSM calculations with real matrix elements. Second, the arithmetic of complex numbers is more time-consuming compared to real numbers. Third, since we use the $S_{\max}$ truncation together with the number of single-particle scattering states, the Hamilton matrix is denser compared to the standard NCSM. Consequently, the diagonalization algorithm needs more operations for every iteration and, in general, more iterations. At the moment, it is possible to perform GNCSM calculations for many-body basis dimension of 10^6 to 10^7.

Non-Orthogonal Basis Sets We have already discussed that the inclusion of the Gamow basis requires a complex eigenvalue problem solver. A further property of the Gamow basis
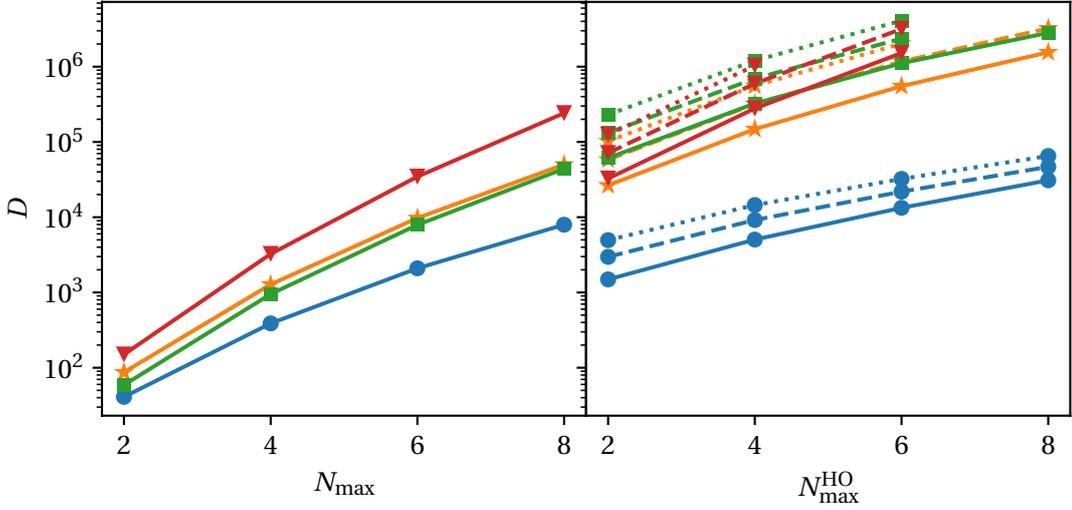
FIGURE 7.1.: Growth of the basis dimension D in dependence on the truncation $N_{\max}^{(\mathrm{HO})}$ for standard NCSM calculations (left) and GNCSM calculations (right) for $^3\mathrm{H}$ (━), $^4\mathrm{H}$ (━), $^4\mathrm{He}$ (━) and $^5\mathrm{He}$ (━). In the GNCSM calculations we use the following partial waves: $s_{1/2}^{\mathrm{n}}$ for $^3\mathrm{H}$, $s_{1/2}^{\mathrm{n}} p_{3/2}^{n}$ for $^4\mathrm{H}$, $p_{3/2}^{\mathrm{pn}}$ for $^4\mathrm{He}$ and $p_{3/2}^{\mathrm{n}}$ for $^5\mathrm{He}$. The contours are discretized with $\nu_{\mathrm{s}} = 12$ (━), 18 (╍), 24 (┄) scattering states. For all calculations we use $l_{\max} = 5$.

is that it is non-orthogonal. This non-orthogonality follows from the expansion in a finite number of HO wave functions, which results in a finite range. Since we usually use around $\nu_{\mathrm{s}} = 18$ scattering states in our calculations, but only use $n_{\max} \leq 12$ HO wave functions to expand the scattering states, the expanded wave functions are guaranteed to be non-orthogonal.

The GNCSM or even the NCSM in general require two main modifications in order to treat non-orthogonal basis sets appropriately. First, we need to solve a generalized eigenvalue problem, which includes an overlap matrix of the basis states. If the basis is orthogonal, this overlap matrix is the identity matrix. The extension towards a generalized eigenvalue solver can be implemented straight forward and can also be solved using the Lanczos algorithm [Lan50]. Second, the calculation of the Hamilton matrix elements has to be redefined. For orthogonal basis sets we use the so called Slater-Condon rules [SO96] to evaluate the matrix elements of an n-body operator in second quantization for Slater determinant. The matrix elements of many-body Slater determinants are expressed in terms of a sum of matrix ele-

ments of n-particle states. This simplification cannot be adopted for non-orthogonal basis sets. Besides the formal extension for the calculation of the many-body matrix elements, it is also important to note that the implementation of such an extension requires a lot of work.

Center-of-Mass Spuriousity   The calculation of the center-of-mass Hamiltonian as it is defined in equation (2.10) is not possible in the GNCSM. The matrix elements of the center-of-mass operator are not defined for resonance and scattering states. Applying the approximation method using HO wave functions as it is used for the interaction matrix elements is not useful since the matrix elements of center-of-mass Hamilton do not converge. A possible solution is a different definition of the center-of-mass Hamiltonian which yields valid matrix elements for resonance and scattering states. It includes the center-of-mass orbital angular momentum $\hat{L}_z$ [Mic+08]

$$\hat{H}_{\mathrm{cm}} \propto \hat{L}_z^2. \tag{7.4}$$

On the other hand, we know that scattering states are translationally invariant outside of the interaction range [Pap+13]. In our case, we do not use a Lawson term in the Hamiltonian since we use the GNCSM to calculate a reference state for the subsequent NAT-GNCSM calculation. In the NAT-GNCSM, we are able to expand the center-of-mass Hamiltonian and use the Lawson term from equation (2.11) once again.

7.2. Overlap Method

For the GNCSM we have to define a new method to identify the many-body bound and resonance eigenstates of interest. The inclusion of continuum degrees of freedom entails that many-body resonances of interest are embedded in the discretized scattering continuum [Mic+08]. Thus, most of the many-body states we calculate are many-body scattering states.

In order to identify the many-body resonances we use the so called overlap method [Mic+03]. For this method we perform a GNCSM calculation for $S_{\mathrm{max}} = 0$. Hence, we only allow HO states as well as bound and resonance states in the Berggren partial waves in the many-body model space. The results of this calculation provide a bound-state approximation since the scattering continuum is not included yet. We assume that most of the information about the full many-body resonance state is already included in this approximation, hence, the inclusion of the discretized scattering continuum generates a small correction to the final many-body resonance. In order to determine the many-body resonance in the final

calculation we calculate the overlap with the bound-state approximation of the target state $\left|\Psi^{\mathrm{ref}}\right\rangle$ with the eigenstates of the full calculation $\left|\Psi_n^{\mathrm{full}}\right\rangle$

$$O_n = \left|\left\langle \Psi^{\mathrm{ref}} \middle| \Psi_n^{\mathrm{full}} \right\rangle\right|. \tag{7.5}$$

The full calculation refers to a calculation including scattering states, i.e., $S_{\mathrm{max}} > 0$. Since we expect that the contribution of the discretized scattering continuum is small, we assume that the overlap of the physical bound or resonance eigenstate in the full calculation is the state with the largest overlap with the reference state.

7.3. Cheat Sheet: GNCSM calculation

The GNCSM calculation yields the first many-body results. We can use these results to investigate and analyze the parameters and truncations of the Gamow basis and the matrix element expansion. During the GNCSM calculation we only face new truncations and no additional parameters. The model space truncations $N_{\mathrm{max}}^{\mathrm{HO}}$ and S_{max} can be increased in an *ab initio* manner in contrast to the simplification of an orthogonal eigenvalue problem solver for a non-orthogonal basis set.

GNCSM	Truncations
1.) Setup reference many-body model space	$N_{\mathrm{max}}^{\mathrm{HO}}$, $S_{\mathrm{max}} = 0$
2.) Setup full many-body model space	$N_{\mathrm{max}}^{\mathrm{HO}}$, $S_{\mathrm{max}} > 0$
3.) Solve eigenvalue problem for both model spaces	orthogonal solver
4.) Determine largest overlap for full calculation	
5.) Analyze parameter and truncation dependence	

7.4. Triton Ground-State Energy

Finally, we are able to perform the first GNCSM calculations and validate our code. For this, we use the ground-state energy of ^{3}H. Since the ground-state of ^{3}H is a bound state, we can compare the results from the GNCSM with results from the standard NCSM. If we only

use scattering states on the real momentum axis, the GNCSM should yield exactly the same results as the standard NCSM. Hence, we can investigate the impact of the single-particle truncations and the matrix element approximation on the final many-body results even without the inclusion of the complex continuum. Furthermore, we can analyze how the non-orthogonality of the Gamow basis effects the results using an eigenvalue problem solver for orthogonal eigenvalue problems.

The single-particle basis is parametrized by the one-body potential for the R-matrix calculation of the partial waves in the Berggren basis, the contour path and the HO frequency for the partial waves in the HO basis

$$
\begin{aligned}
V_{\mathrm{WS}} &= -25\,\mathrm{MeV}, & V_{\mathrm{LS}} &= -30\,\mathrm{MeV}, \\
a_{\mathrm{WS}} &= 0.67\,\mathrm{fm}, & R_{\mathrm{WS}} &= 1.83\,\mathrm{fm}, \\
\hbar\Omega &= 20\,\mathrm{MeV}.
\end{aligned}
\tag{7.6}
$$

This potential produces a bound single-particle state in the $s_{1/2}^{\mathrm{pn}}$ partial waves with an energy of

$$
E_{\mathrm{b}}\left(s_{1/2}^{\mathrm{pn}}\right) = -5.16\,\mathrm{MeV}.
\tag{7.7}
$$

We only include scattering states in the s-wave and, more importantly, no broad resonance in the p-wave. Thus, it is possible to use matrix elements up to HO frequencies of $24\,\mathrm{MeV}$. Recall, the matrix element expansion in figure 6.4 is most problematic for the diagonal matrix element of the single-particle resonance state. For the analysis of truncations of the Gamow basis we use a default set of truncation values

$$
\begin{aligned}
k_{\max} &= 3\,\mathrm{fm}^{-1}, & v_{\mathrm{s}} &= 30, \\
R_{\mathrm{cut}} &= 10\,\mathrm{fm}, & e_{\max} &= 24, \\
l_{\max} &= 5.
\end{aligned}
\tag{7.8}
$$

We use three different Gamow basis sets with different partial wave combinations, i.e., the $s_{1/2}^{\mathrm{p}}$, $s_{1/2}^{\mathrm{n}}$ and $s_{1/2}^{\mathrm{pn}}$ partial waves. The path of the contour leads along the real axis of the complex momentum plane and the scattering points are split equidistantly. The truncation for the maximum number of scattering states allowed in the model space $S_{\max}$ is set large enough to allow all possible nucleons to occupy a scattering state, i.e., $S_{\max} = 1, 2$ and 3 for the three Gamow basis sets, respectively. The results of the calculations are shown in figure 7.2. The ground-state energies are almost converged for all single-particle basis sets and the largest overlaps for the ground state are very large, which is expected for a bound state.
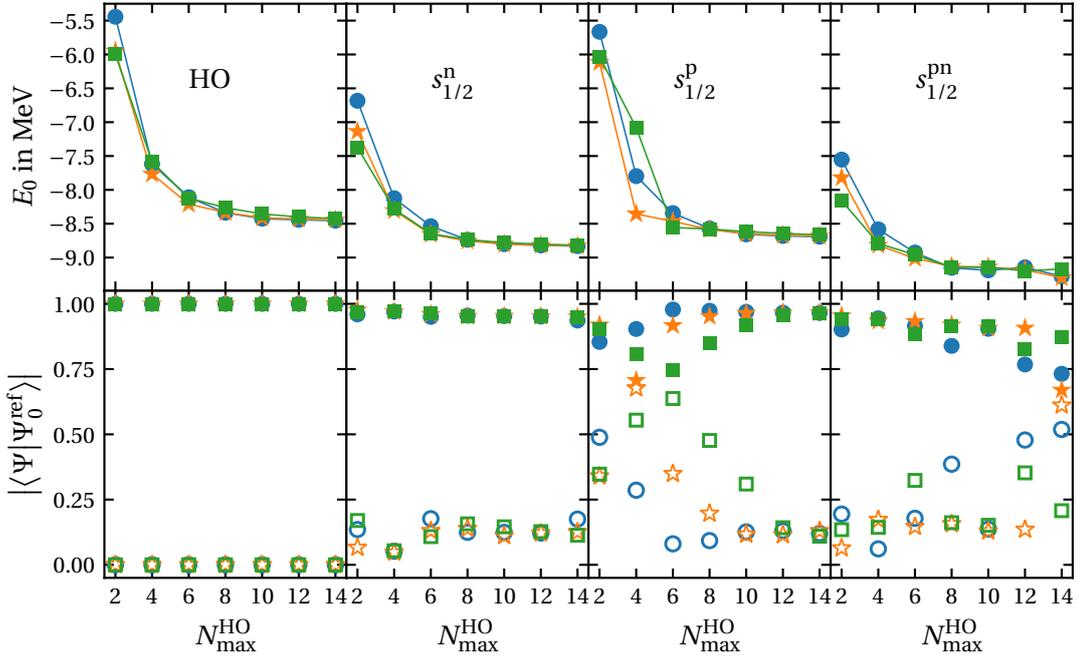
FIGURE 7.2.: Benchmark of the GNCSM for the calculation of the ground-state energy of ^{3}H depending on the many-body truncation $N_{\max}^{\mathrm{HO}}$ and the HO frequencies 16 MeV (●), 20 MeV (★) and 24 MeV (■). The first row shows the energy of the ground state and the second row shows the largest (filled) and second to largest (open) overlaps. The columns show the standard NCSM calculation using the HO single-particle basis as benchmark calculation and three different Gamow basis sets with different partial waves selections. The 30 scattering states are placed on an equidistant grid on the real momentum axis from 0 to $k_{\max} = 3\,\mathrm{fm}^{-1}$. All remaining parameters are defined in equations (7.6) and (7.8).

However, the convergence of the ground-state energy shows two anomalies which need to be discussed further.

First, even though the results are not fully converged we can already see that all GNCSM calculations yield different ground-state energies. During the setup of the GNCSM we utilized three approximations, which can influence the final result in an uncontrolled way. First, for the calculation of the nuclear matrix elements we are limited to a HO single-particle space

of $e_{\text{max}} = 24$ which produces an uncertainty in the matrix elements. Second, the intrinsic and center-of-mass part of the many-body wave function are not decoupled. Third, the Gamow basis is non-orthogonal for the Berggren partial waves after the expansion of the matrix element, but the GNCSM diagonalization does not account for this non-orthogonality. The degree of the non-orthogonality increases with the number of scattering states, because the same number of HO states is used in order to approximate all scattering states. For exact results, the GNCSM has to be extended towards non-orthogonal basis sets.

A different approach to bypass the problem of the non-orthogonal Gamow basis is to use a natural-orbital basis. The set of Gamow natural orbitals has two immediate advantages. First, it is an orthonormal basis and following many-body eigenvalue problem can be solved as such. Second, the number of single-particle states in the Berggren partial waves is lowered to the number of HO single-particle states used for the expansion of the matrix elements, which significantly lowers the dimension of the many-body model spaces.

The second anomaly concerns the pathological convergence behavior, e.g., for the $N_{\text{max}}^{\text{HO}} = 2, 4, 6$ sequence for the $s_{1/2}^{\text{p}}$ Gamow basis and HO frequencies $20\,\text{MeV}$ and $24\,\text{MeV}$. The values for the ground-state energy for $N_{\text{max}}^{\text{HO}} = 4$ seem to be smaller or larger than expected, respectively. That alone is not formally forbidden, however in order to understand what happens at this step in the $N_{\text{max}}^{\text{HO}}$ sequence, we take a closer look at the values of the two largest overlaps corresponding to these HO frequencies in the second row of figure 7.2. For the given example, the largest overlap decreases and the second largest overlap increases for $N_{\text{max}}^{\text{HO}} = 4$. This means that there exist two states that are very similar to the reference state. In our example the value of the ground-state energy for $20\,\text{MeV}$ seems to be too low, whereas the value for $24\,\text{MeV}$ seems to be too large.

The overlaps and energies of the two eigenstates with the largest overlaps are shown in table 7.1. The left-hand table shows that the energy values depend on the HO frequency. The values do not coincide exactly, but it is still apparent that the eigenvalues for the HO frequencies $20\,\text{MeV}$ and $24\,\text{MeV}$ are interchanged. In both cases the values of the largest two overlaps are comparably close together and both values differ from the expected result given by the calculation for the HO frequency $16\,\text{MeV}$. Often times, the degeneracy in the eigenstates is an effect that only appears for one step in the $N_{\text{max}}^{\text{HO}}$ sequence, in this case $N_{\text{max}}^{\text{HO}} = 4$, and the gap between the two largest overlaps is significantly larger for the neighboring $N_{\text{max}}^{\text{HO}}$ values. This behavior is shown in the table 7.1 (B) for the $N_{\text{max}}^{\text{HO}} = 2, 4, 6$ sequence for the HO frequency $20\,\text{MeV}$.

$\hbar\Omega$	n	$\left|\langle\Psi_n|\Psi_0^{\text{ref}}\rangle\right|$	E_n
16 MeV	0	0.90	$-7.80\,\text{MeV}$
	1	0.29	$-6.58\,\text{MeV}$
20 MeV	0	0.71	$-8.35\,\text{MeV}$
	1	0.68	$-7.16\,\text{MeV}$
24 MeV	0	0.81	$-7.08\,\text{MeV}$
	1	0.55	$-8.65\,\text{MeV}$

(A) Variation of $\hbar\Omega$ for $N_{\max}^{\text{HO}} = 4$.

$N_{\max}^{\text{HO}}$	n	$\left|\langle\Psi_n|\Psi_0^{\text{ref}}\rangle\right|$	E_n
2	0	0.92	$-6.11\,\text{MeV}$
	1	0.34	$-8.27\,\text{MeV}$
4	0	0.71	$-8.35\,\text{MeV}$
	1	0.68	$-7.16\,\text{MeV}$
6	0	0.92	$-8.47\,\text{MeV}$
	1	0.35	$-7.72\,\text{MeV}$

(B) Variation of $N_{\max}^{\text{HO}}$ for $\hbar\Omega = 20\,\text{MeV}$.

TABLE 7.1.: Comparison of the eigenvalues E_n of the eigenstates $|\Psi_n\rangle$ with the largest overlaps for different HO frequencies (A) and a sequence of $N_{\max}^{\text{HO}}$ truncations (B). The data corresponds to the data shown in figure 7.2 for the $s_{1/2}^{\text{p}}$ Gamow basis.

7.5. Truncation Dependence of Triton Ground-State Energy

In this section, we investigate the dependence of the many-body results on a variation of the default single-particle truncations defined in equation (7.8). Furthermore, we analyze the dependence on the many-body scattering truncation $S_{\max}$. For all parameters that are not varied explicitly, we use the default single-particle truncation parameters and $S_{\max} = 2$. We use the single-particle basis characterized by the parameters in equation (7.6) and the $s_{1/2}^{\text{n}}$ Gamow basis already used in figure 7.2.

Matrix Element Expansion In chapter 6, we have set the optimal values for the maximum energy of the HO approximation wave functions and the cutoff of the radial integral to

$$e_{\max} = 24,$$
$$R_{\text{cut}} = 10\,\text{fm}.$$

Since the values for the expansion of the matrix elements are not fully converged for scattering matrix elements, we want to analyze the impact of the uncertainty in the matrix element values on the results of the GNCSM. Figure 7.3 shows the dependence of the energy convergence of the ^{3}H ground state on both parameters. The ground-state energies are independent of these two truncations for all $N_{\max}^{\text{HO}}$, i.e., the uncertainty from the calculations of the matrix

(A) Variation of the single-particle energy truncation of the HO basis $e_{max} = 16$ (●), 20 (★) and 24 (■).

(B) Variation of the radial cutoff in the HO approximation $R_{cut} = 6\,fm$ (●), $8\,fm$ (★), $10\,fm$ (■).
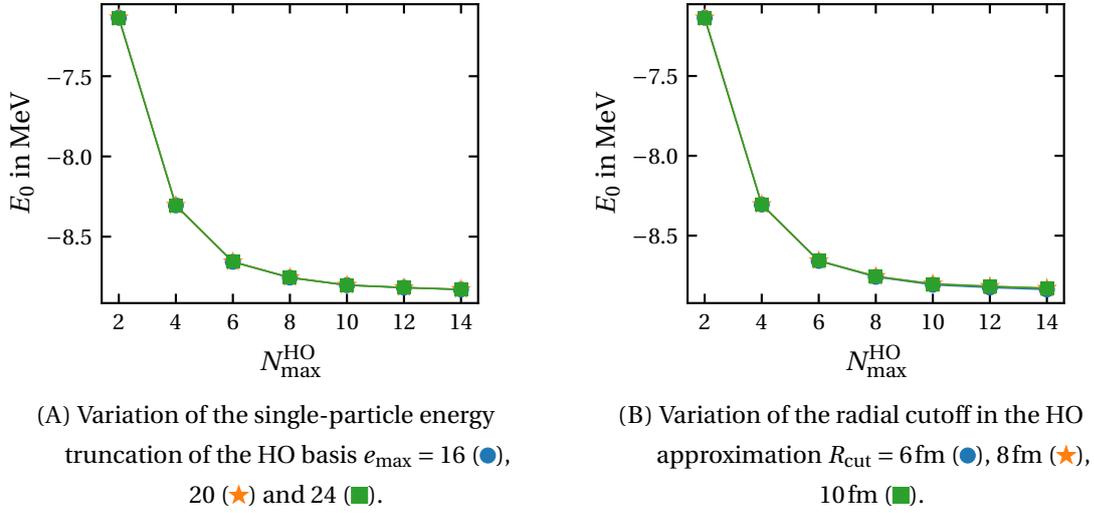
FIGURE 7.3.: Analysis of impact of the matrix element approximations on the convergence behavior of the ground-state energy of ^3H with respect to N_{max}^{HO} in the GNCSM. The plots show the dependence on the maximum single-particle energy in the HO wave function approximation (A) and the radial cutoff in the HO wave function approximation (B). The Gamow basis uses the $s_{1/2}^n$ partial waves in the Berggren basis.

element expansion does not affect the many-body results. This behavior is not guaranteed and might be a consequence of the large overlap of $> 90\,\%$ for the full eigenstate. Thus, Slater determinants that occupy scattering states only contribute with $< 10\,\%$ to the norm of the full eigenstate. This small contribution in combination with the small uncertainties of matrix elements containing scattering states does not generate a visible impact on the ground-state energy.

Single-Particle Basis Truncation   After the analysis of the matrix element truncation, we take a closer look at the single-particle basis truncations that affect the single-particle model space. The variation of these single-particle truncations is shown in figure 7.4.

We start with a discussion of the truncation of the maximum orbital angular momentum. In figure 7.4 (A), we show that the results with respect to the maximum orbital angular momentum are converged for $l_{max} \geq 5$. The next truncation to the single-particle basis is the cutoff of the scattering contour, i.e., the maximum momentum k_{max}. In order to rule out the dependence on the grid spacing of the discretization, we use a constant grid spacing Δk in

(A) Convergence of maximum orbital angular momentum $l_{max} = 3$ (●), 4 (★), 5 (■), 6 (▼).

(B) Convergence of contour cutoff $k_{max} = 2\,\mathrm{fm}^{-1}$ (●), $3\,\mathrm{fm}^{-1}$ (★), $4\,\mathrm{fm}^{-1}$ (■) with $\nu_s = 20$, 30, 40 respectively.

(C) Convergence with number of scattering states $\nu_s = 10$ (●), 20 (★), 30 (■), 40 (▼).
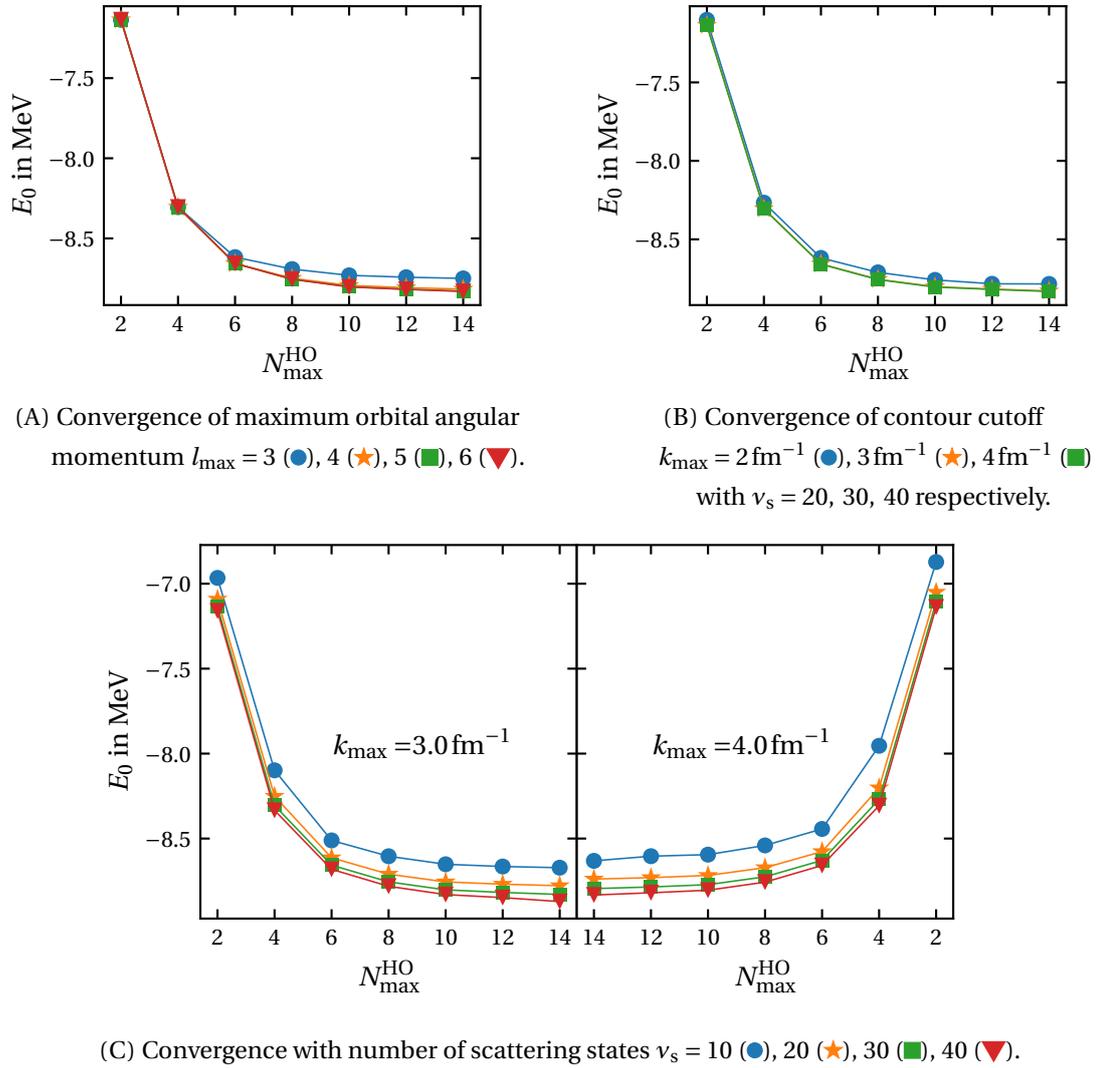
FIGURE 7.4.: Analysis of truncation parameters on the convergence behavior of the ground-state energy of ^{3}H with respect to N_{max}^{HO} in the GNCSM. The plots show the dependence on truncation of the single-particle basis, i.e., the maximum orbital angular momentum (A), the contour cutoff (B) and the step size in the contour discretization (C).

figure 7.4 (B). The results are converged for $k_{max} = 3\,\mathrm{fm}^{-1}$ for $\Delta k = 0.1\,\mathrm{fm}^{-1}$.

Lastly, we take a look at the dependence of the results on the grid spacing of the discretization, which is parametrized by the number of scattering points on the contour. In figure 7.4

(C), we show the results for two momentum cutoffs and different numbers of scattering states, i.e., different grid spacings. The convergence with respect to the number of scattering states is very poor for $\nu_s \geq 20$ for both values of k_{max}. Furthermore, the values are shifted upwards for the larger value of $k_{max} = 4\,\mathrm{fm}^{-1}$. This in combination with the previous observation that the momentum cutoff is converged at $k_{max} = 3\,\mathrm{fm}^{-1}$ shows that two truncations counteract each other. On the one hand, a larger number of scattering states is a more accurate approximation of the scattering contour. On the other hand, the more scattering states we include, the higher does the level of non-orthogonality increase.

For this section, we choose $\nu_s = 30$ for the analysis of ^{3}H, however in following calculations for heavier nuclei we have to use smaller values in order to keep the model space dimension manageable. When we introduce the Gamow natural orbitals in chapter 8, we analyze the dependence of the natural orbitals on the number of scattering states again. As mentioned before, the Gamow natural orbitals are supposed to remedy the problem of a non-orthogonal single-particle basis.

Many-Body Basis Truncation   The last truncation we analyze is the many-body truncation parameter S_{max} which truncates the maximum number of scattering states allowed in the model space. For the Gamow basis using the $s_{1/2}^n$ partial wave this means that at maximum both neutrons in ^{3}H occupy scattering states. Thus, for $S_{max} \geq 2$ this truncation effectively vanishes and only the N_{max}^{HO} truncation remains. Since the model spaces in ^{3}H are very small it is possible to choose $S_{max} = 2$ and converge all calculations with respect to the remaining N_{max}^{HO} truncation. This is not possible for all nuclei with $A > 3$ whose model spaces grow factorially as already shown in figure 7.1 earlier.

In figure 7.5, we show the variation of the scattering truncation for the calculation of the ground-state energy and overlaps of ^{3}H. The calculation for $S_{max} = 0$, which only includes bound and resonance single-particle states, already generates a bound state and the largest overlap is one by definition. If we include scattering states in the model space the results lie $\sim (10\text{ to }15)\,\%$ below the energy for $S_{max} = 0$. This justifies the overlap method which is built on the assumption that the inclusion of single-particle scattering states produces a small correction to the bound-state energy. Another observation regarding the overlaps is the ordering of the largest overlaps for $S_{max} = 1$ and $S_{max} = 2$. Contrary to expectations the overlaps do not increase for larger values of S_{max} even though larger values of S_{max} add Slater determinants with more scattering states occupied to the many-body model space.

One thing that we have not discussed up to now is why scattering states have a contribution
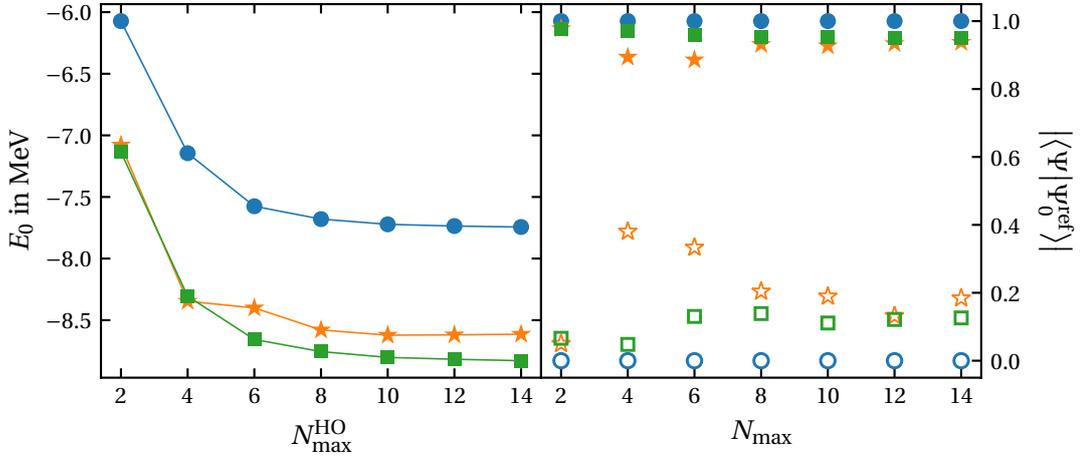
FIGURE 7.5.: Analysis of the model space convergence for the ground-state energy in the first column and the largest (filled) and second to largest (open) overlaps of ^{3}H in the second column. The model spaces are truncated with the scattering truncations $S_{\max} = 0$ (●), 1 (★), 2 (■).

to the bound state of ^{3}H at all. The radial wave function of a bound state is finite. Hence, it cannot include scattering states, which are essentially plane waves in the asymptotic region. However, the only input to the GNCSM calculation are matrix elements and the matrix elements mainly include the short-range part of the scattering wave functions. This means the GNCSM knows the short-range part of the scattering states, but not the asymptotic behavior. Consequently, the bound state of ^{3}H includes Slater determinants that occupy scattering states as well.

7.6. Calculation of the ^{4}H Ground-State Resonance Energy

The previous calculation of the ground-state energy of the bound ^{3}H served as a first approach to GNCSM calculations and the different parameters that need to be considered for a robust many-body result. Since it is a bound state, we do not expect large contributions by the scattering states, which is reflected in large overlaps with the bound-state approximation. In this section, we take a look at the $J^\pi = 2^-$ ground-state resonance of ^{4}H. In this case, the standard NCSM only yields a bound-state approximation to the ground-state energy and the inclusion of the continuum is necessary for a correct description of the ground state. We

expect that the inclusion of single-particle resonance and scattering continuum states has a larger impact on the final wave function compared to the ^{3}H ground state. Similar to the calculation of ^{3}H, we have to analyze the dependence on the basis truncations before we can explore different one-body potentials and contour paths for the GNCSM calculations.

Compared to the previous calculation we use a slightly weaker one-body potential which produces a broader resonance and needs a broader contour path for the calculations

$$
\begin{aligned}
V_{\text{WS}} &= &-20\,\text{MeV}, & \quad V_{\text{LS}} &=& -25\,\text{MeV}, \\
a_{\text{WS}} &= &0.67\,\text{fm}, & \quad R_{\text{WS}} &=& 2.02\,\text{fm}, \\
k_1 &= &(0.3-0.2\text{i})\,\text{fm}^{-1}, & \quad k_2 &=& 0.6\,\text{fm}^{-1}, \\
\hbar\Omega &= &16\,\text{MeV}.
\end{aligned}
\tag{7.9}
$$

We already used this potential during the calculation of the radial wave functions in chapter 5 and matrix elements in chapter 6. This potential produces a bound and a resonance single-particle state in the $s^{\text{n}}_{1/2}\, p^{\text{n}}_{3/2}$ partial waves with energies and resonance momentum of

$$E_{\text{b}}\left(s^{\text{n}}_{1/2}\right) = -3.35\,\text{MeV}, \tag{7.10}$$

$$E_{\text{r}}\left(p^{\text{n}}_{3/2}\right) = (0.98-0.84\text{i})\,\text{MeV}, \tag{7.11}$$

$$k_{\text{r}}\left(p^{\text{n}}_{3/2}\right) = (0.27-0.1\text{i})\,\text{fm}^{-1}. \tag{7.12}$$

The set of suitable HO frequencies is limited to $\hbar\Omega \le 16\,\text{MeV}$ as we have seen in chapter 6. For the analysis of truncations of the Gamow basis, we use almost the same set of optimal truncation values. In order to make the calculations feasible the number of scattering points needs to be smaller

$$
\begin{aligned}
k_{\text{max}} &= &3\,\text{fm}^{-1}, & \quad \nu_{\text{s}} &=& 18, \\
R_{\text{cut}} &= &10\,\text{fm}, & \quad e_{\text{max}} &=& 24, \\
l_{\text{max}} &= &5.
\end{aligned}
\tag{7.13}
$$

The first calculations of the ^{4}H ground-state energy are shown in figure 7.6 for different partial-wave selections and HO frequencies. Since the ground state of ^{4}H has total angular moment $J = 2$, we expect a single neutron in the $p^{\text{n}}_{3/2}$ shell. Therefore, we use two different single-particle Gamow basis sets which include the $p^{\text{n}}_{3/2}$ shell in order to calculate the many-body resonance, i.e., $p^{\text{n}}_{3/2}$ and $s^{\text{n}}_{1/2}\, p^{\text{n}}_{3/2}$.

The real part of the energy has a similar convergence behavior for both partial-wave selections. Furthermore, the overlaps of the ground state are smaller compared to the bound state of ^{3}H, which shows the impact of the continuum to the state. The two partial-wave
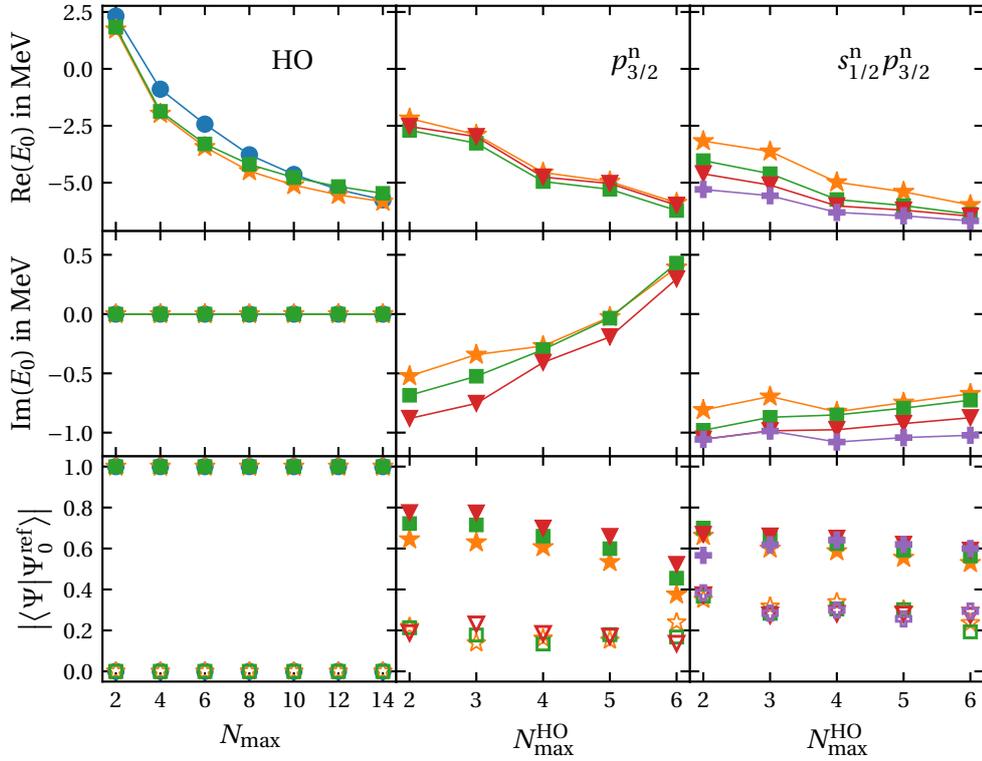
FIGURE 7.6.: Calculation of the ground-state energy of ^{4}H in the GNCSM for different Gamow basis sets (middle, right) and the HO basis in the standard NCSM (left) using the HO frequencies 8 MeV (●), 12 MeV (★), 16 MeV (■), 20 MeV (▼) and 24 MeV (✚). The first and second row show the real and imaginary part of the ground-state energy, respectively. The third row shows the largest (filled) and second to largest (open) overlaps. For every single-particle basis set we show the three HO frequencies with the best convergence behavior for the real part of the energy.

selections differ for the imaginary part of the energy. For small values of $N_{\max}^{\mathrm{HO}}$ we find a many-body resonance state with negative values for the imaginary part of the energy. However, for larger $N_{\max}^{\mathrm{HO}}$ and decreasing real parts the imaginary part of the energy becomes positive if we only use the $p_{3/2}^{\mathrm{n}}$ partial wave in the Berggren basis.

In case of the $s_{1/2}^{\mathrm{n}} p_{3/2}^{\mathrm{n}}$ partial-wave selection the imaginary part of the energy remains almost constant, which indicates that the continuum information from the $s_{1/2}^{\mathrm{n}}$ partial wave

is not negligible. For the following calculations in this section, we use the $s^{\mathrm{n}}_{1/2} p^{\mathrm{n}}_{3/2}$ partial-wave selection. The dependence on the HO frequency is very small for a broad range of frequencies for the standard HO calculation and the calculation using the $p^{\mathrm{n}}_{3/2}$ partial wave. This is not the case if we use the $s^{\mathrm{n}}_{1/2} p^{\mathrm{n}}_{3/2}$ partial-wave selection for which the energy decreases further for increasing HO frequencies.

7.7. Truncation and Parameter Dependence of ^{4}H Ground-State Energy

In this section, we analyze the dependence of many-body results on three types of parameters. First, we analyze the influence of the truncations in the matrix element expansion. Second, we investigate the convergence of the results with respect to the single-particle and many-body basis truncation parameters. Third, we analyze the dependence on the one-body potential and the contour path parameters used for the calculations. If the parameter is not varied specifically, we us the default parameters defined in equations (7.13) and (7.9) and the $s^{\mathrm{n}}_{1/2} p^{\mathrm{n}}_{3/2}$ partial-wave selection with $S_{\max} = 2$.

Matrix Element Expansion We start with the analysis of the matrix-element expansion, which showcases the problems and uncertainties arising in the many-body result of ^{4}H. In section 6.2 we already defined optimal values for R_{cut} and $e_{\max}$ and the benchmark for the ground-state energy of ^{3}H shows that the results are converged for these optimal values. However, for the ground-state energy of ^{4}H it causes an uncertainty since the impact of scattering states is much larger as reflected in smaller overlaps of $\sim 60\,\%$ for the ^{4}H ground state compared to overlaps of $\sim 90\,\%$ for ^{3}H.

Figure 7.7 shows the dependence of the real part of the ground-state energy on R_{cut} and $e_{\max}$. In the left part of the figure, we show that the results for a HO frequency of $16\,\mathrm{MeV}$ depend on R_{cut}. This is not surprising since we have already demonstrated in section 6.2 that for small R_{cut} we cut off some parts of the long-range interaction, whereas for large cutoffs the wave function approximation becomes unstable. Therefore, we have to accept a small uncertainty in the final result of the many-body calculations, which appears if the impact of scattering states increases in the ground-state wave function.

In the right-hand panel of figure 7.7, we show the results for the HO frequency of $24\,\mathrm{MeV}$, which seem to converge for larger R_{cut}. However, as discussed in section 6.2 this is a consequence of the range of the wave functions which is about $10\,\mathrm{fm}$ for $e_{\max} = 24$. The calculation of the HO expansion coefficients becomes unstable and does not change for larger R_{cut} since the wave functions have already fallen off to zero at this point. This example shows how a
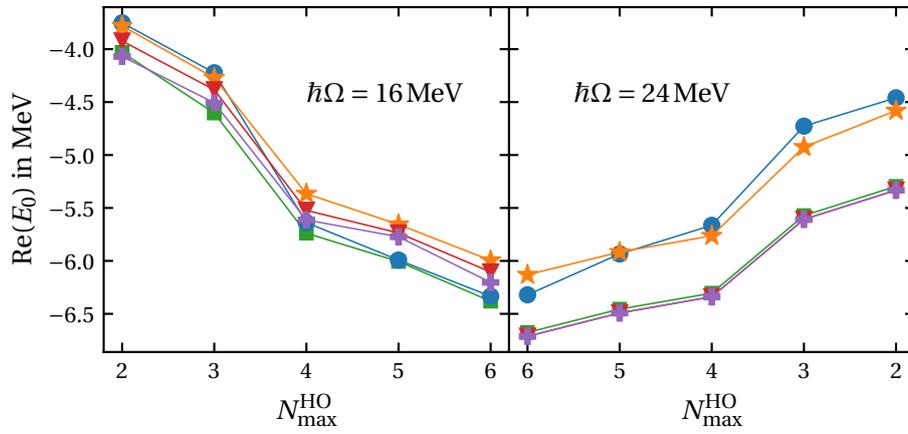
(A) Variation of the radial cutoff in the HO approximation $R_{\text{cut}} = 8\,\text{fm}$ (●),
9 fm (★), 10 fm (■), 11 fm (▼) and 12 fm (✚).
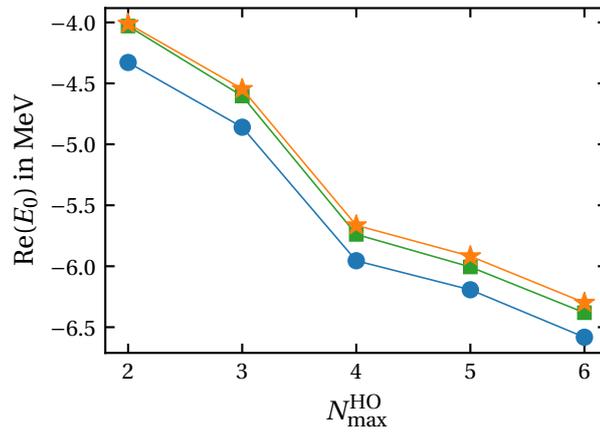
(B) Variation of the single-particle energy truncation of the
HO basis $e_{\text{max}} = 16$ (●), 20 (★) and 24 (■).

FIGURE 7.7.: Analysis of effect of the matrix element approximations on the convergence behavior of the ground-state energy of ^{4}H with respect to $N_{\text{max}}^{\text{HO}}$ in the GNCSM. The plots show the dependence on the radial cutoff (A) and the maximum single-particle energy (B) in the HO wave function approximation.

false convergence can appear in the many-body calculation as consequence of the matrix element that are not converged with respect to e_{max} for HO frequencies larger that 16 MeV.

The second parameter that affects the matrix element expansion is the maximum number

of HO wave functions in the expansion of the wave function which is given by $e_{\max}$. In figure 7.7 (B), we show that the result for the real part of the energy is not completely converged for the maximum value $e_{\max} = 24$. However, the uncertainty is very small compared to the overall uncertainty arising from the many-body calculation.

Even though these uncertainties in the final many-body results seem problematic, it does not have to be a problem for the calculations using Gamow natural orbitals later on. We can expect the uncertainties from R_{cut} and $e_{\max}$ to be negligible because they do not change the physical characteristics of the wave function very much, i.e., the state is always well bound and has a negative imaginary part, which corresponds to a resonance state. Hence, a further development in the calculation of the HO matrix elements in order to reach higher values for $e_{\max}$ does not enhance the results later on.

Model Space Truncations   In the next part of our analysis, we take a look at the convergence with respect to the model space truncations. On the one hand, the number of scattering states ν_s in the Berggren partial waves of the Gamow basis truncates the single-particle basis. On the other hand, the many-body scattering truncation $S_{\max}$ truncates the many-body Slater determinant basis. For both truncations the resulting many-body basis dimension increases rapidly with increasing truncations. Thus, for large values of ν_s and $S_{\max}$ we are limited to small values of $N_{\max}^{\mathrm{HO}}$.

In figure 7.8 we show the real and imaginary part of the ground-state energy of ^{4}H depending on the number of scattering states ν_s and the many-body scattering truncation $S_{\max}$. The convergence of ν_s shows that the calculations are almost converged for the real and imaginary part of the energy for a large number of scattering points. Furthermore, the imaginary part of the energy tends towards a constant if we increase the number of scattering states. The residual variation can result from the non-orthonormality of the single-particle basis as we have already discussed for the ^{3}H ground-state energy in figure 7.4 (C). For the variation of the many-body scattering truncation $S_{\max}$ we are unable to perform calculations for $S_{\max} = 3$ and $N_{\max}^{\mathrm{HO}} > 3$ due to the large many-body model space dimension. However, the results are almost converged for $S_{\max} = 2$ for the real and imaginary part of the energy. Again, the convergence pattern of the imaginary part of the energy tends towards a constant for larger values of $S_{\max}$. Following the argument from the previous paragraph, we expect that the impact of the uncertainty on the results for values of $\nu_s \geq 12$ and $S_{\max} \geq 2$ to be very small in the following calculations with Gamow natural orbitals.

(A) Convergence with number of scattering states $\nu_s = 0$ (●), 6 (★), 12 (■), 18 (▼) and 24 (✚).

(B) Convergence of many-body scattering truncation $S_{\max} = 0$ (●), 1 (★), 2 (■) and 3 (▼).
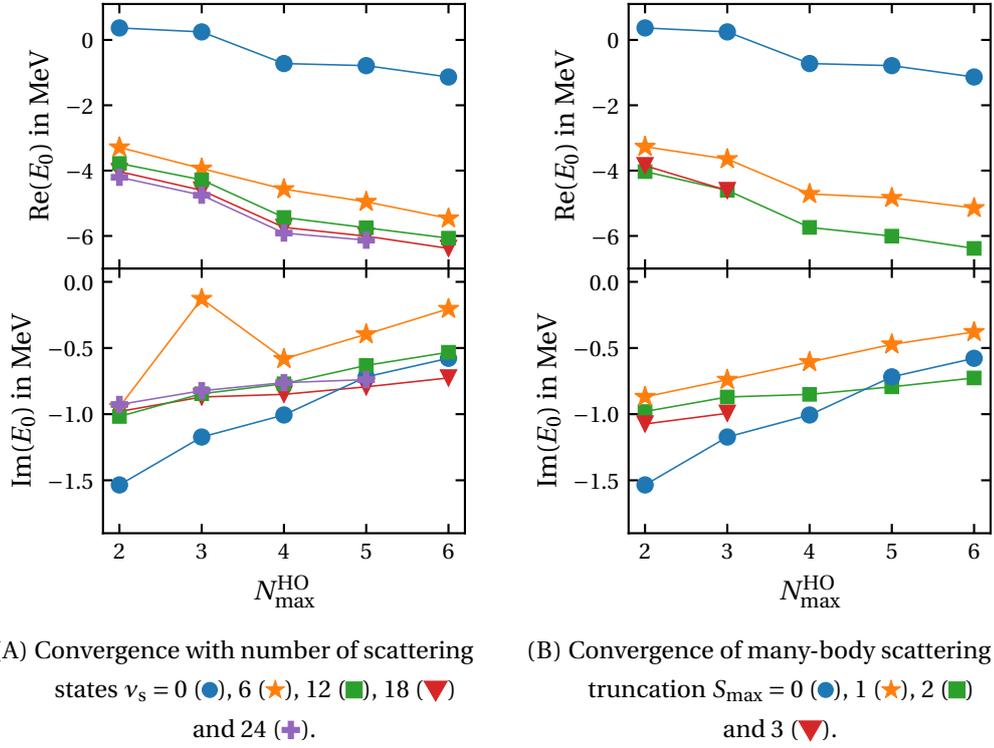
FIGURE 7.8.: Analysis of truncation parameters on the convergence behavior of the ground-state energy of ^{4}H with respect to $N_{\max}^{\mathrm{HO}}$ in the GNCSM. The plots show the dependence on the number of scattering states on the contour (A) and on the many-body scattering truncation (B). The first and second row show the real and imaginary part of the ground-state energy, respectively.

Single-Particle Basis Variation In the previous paragraphs, we analyzed the dependence of different approximations and truncations on the ground-state energy of ^{4}H and the goal was to find truncation values for which the final results are converged. In theory, we would like to achieve the same converged results for different single-particle Gamow basis sets because the result of the many-body calculations should be independent of the single-particle basis. However, we discretize the continuum and restrict ourselves to specific parts of the continuum, e.g., a specific selection of partial waves in the Berggren basis. As a consequence, we obtain a model dependence on the specific one-body potential or contour path used in the Berggren partial waves. In this paragraph, we analyze how the many-body results depend on different single-particle basis sets and contour paths.

potential	V_{WS} in MeV	V_{LS} in MeV	a_{WS} in fm	$E_b\left(s_{1/2}^n\right)$ in MeV	$E_r\left(p_{3/2}^n\right)$ in MeV
I	-20	-25	0.67	-3.35	$0.98 - 0.84i$
II	-19	-25	0.67	-2.93	$1.05 - 1.0i$
III	-21	-25	0.67	-3.78	$0.89 - 0.69i$
IV	-15	-20	1.2	-2.02	$0.42 - 0.39i$
V	-25	-30	0.67	-5.64	$0.47 - 0.22i$

TABLE 7.2.: List of five different one-body potentials with different potential parameters for the calculation of a Gamow basis of ^4H. It includes the energy of the bound and resonance state in the $s_{1/2}^n$ and $p_{3/2}^n$ partial wave, respectively.

For the variation of one-body potentials we use a set of one-body potentials characterized in table 7.2. The default one-body potential is potential I. The potentials II and III only differ in a small decrease and increase of the Woods-Saxon potential depth, respectively. Thus, the energies of the bound and resonance states do not vary much. A larger variation in the one-body potential definition is given for the potentials IV and V which also include changes in the other potential parameters. This also produces different energies for the bound and resonance states.

The results for the variation of the five one-body potentials are shown in figure 7.9 (A). The small shifts in the Woods-Saxon potential depth in potentials II and III generates a shift in both parts of the complex energy, but the overall shape of the convergence pattern stays unchanged.

For the potential IV, the Gamow basis still produces a resonance state with an imaginary energy in the order of the first three potentials, but the real part of the energy lies almost $2\,\text{MeV}$ below the first three potentials throughout the N_{max}^{HO} sequence. For this potential, the non-orthonormality of the Gamow basis and approximation of the matrix elements generates large uncertainties on the final results. This does not exclude this calculation for a following natural-orbital calculation, but needs to be treated with care. We will analyze the influence of the one-body potentials again for the natural-orbital calculations later on.

Finally, potential V does not produce a many-body resonance state at all which might become a problem in the upcoming natural-orbital calculations. In fact, this potential produces multiple states with very similar overlaps, which also explains the kink in the
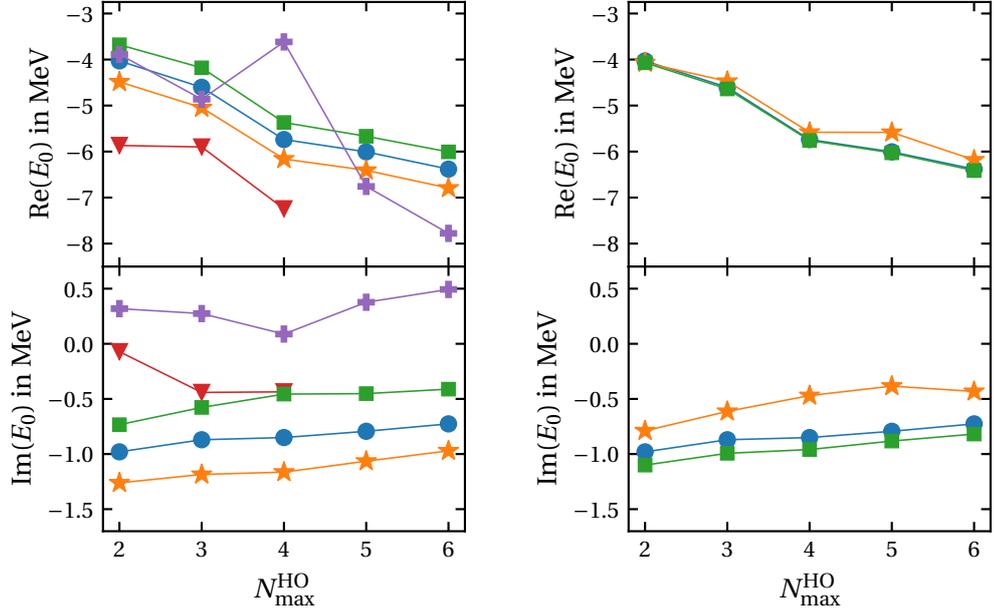
(A) Variation of one-body potentials I (●), II (★), III (■), IV (▼) and V (✚).

(B) Variation of contour path $k_1 = (0.3 - 0.2i)\,\text{fm}^{-1}$ (●), $(0.3 - 0.3i)\,\text{fm}^{-1}$ (★) and $(0.3 - 0.15i)\,\text{fm}^{-1}$ (■).

FIGURE 7.9.: Analysis of different one-body potentials (A) and contour paths (B) on the convergence behavior of the ground-state energy of ^{4}H with respect to $N_{\max}^{\text{HO}}$ in the GNCSM. The first and second row show the real and imaginary part of the ground-state energy, respectively.

convergence pattern at $N_{\max}^{\text{HO}} = 4$.

As our final analysis, we take a look at the impact of different contour paths on the final result. In figure 7.9 (B) we compare two different contour paths to the default path. For simplicity, we only vary the imaginary part of the contour point k_1. The real part of the energy stays almost unchanged except for one pathological point for the broad contour $k_1 = (0.3 - 0.3i)\,\text{fm}^{-1}$ at $N_{\max}^{\text{HO}} = 5$. The imaginary part of the energy is shifted for both variations compared to the default parameter.

This section has shown that the results of the many-body calculations are heavily affected by the underlying Gamow basis. It is necessary to choose a suitable one-body potential in order to obtain reasonable many-body results. If the one-body potential does not yield the

necessary parts of the continuum, we are unable to generate a many-body resonance state. Furthermore, we suggest contour paths that stay rather close to the resonance as given by equation (5.10).

8

GAMOW NO-CORE SHELL MODEL WITH NATURAL ORBITALS

The GNCSM with the natural-orbital single-particle basis (NAT-GNCSM) is an extension to the GNCSM. We use the natural orbitals in order to solve two problems. First, we want to decrease the model space size in order to speed up the convergence. Second, we want to build an orthonormal single-particle basis, such that we can calculate matrix elements and obtain an orthogonal many-body eigenvalue problem. This Gamow natural orbitals have already been applied successfully in the GNCSM framework [Fos+17; Li+19]. Similar to the natural orbitals in the standard NCSM [Con+17; TMR19], it enhances the model space convergence in the many-body calculation.

8.1. Gamow Natural Orbitals

By definition, the natural-orbital basis is the eigenbasis of an one-body density matrix given in equation (2.12). In our case, we use a GNCSM eigenstate as the reference state. Thus, the one-body density matrix elements for every partial wave read

$$
\begin{aligned}
\rho_{nn'}^{(ljm_jm_t)} &= \langle \Psi_{\text{ref}}| \left(\hat{a}_n^{(ljm_jm_t)} \right)^\dagger \hat{a}_{n'}^{(ljm_jm_t)} |\Psi_{\text{ref}}\rangle \\
&= \sum_{i,j} C_i^* C_j \langle \Phi_i| \left(\hat{a}_n^{(ljm_jm_t)} \right)^\dagger \hat{a}_{n'}^{(ljm_jm_t)} |\Phi_j\rangle ,
\end{aligned}
\tag{8.1}
$$

where we used the basis expansion of the NCSM eigenstate from equation (2.2). The creation and annihilation operators are represented in the HO basis. For the computation of the action of these operators on Berggren states in the reference state, we use the same HO expansion as we used for the matrix element calculation before. The resulting one-body density matrix has a block structure and is calculated for every block of the diagonal l, j, m_j, and m_t quantum numbers. Hence, the natural-orbital states for the radial quantum number $\tilde{n}$

$$\left| \tilde{n} l j m_t \right\rangle_{\text{NAT}} = \sum_{n=0}^{n_{\text{max}}} C_{\tilde{n} n}^{(l j m_t)} \left| n l j m_t \right\rangle_{\text{HO}} \tag{8.2}$$

only mix the radial quantum number n of the HO basis. The number of natural-orbital states $\tilde{n}_{\text{max}}$ for every partial wave is

$$\tilde{n}_{\text{max}} = \begin{cases} \frac{e_{\text{max}} - l}{2}, & \text{if Berggren partial wave} \\ n_{\text{max}}, & \text{if HO partial wave} \end{cases} \tag{8.3}$$

The $\tilde{n}$ quantum number orders the natural orbitals states by their occupation probability in the reference state. The occupation probability is given by the eigenvalues $p_{\tilde{n}}$ of the density matrix entries. We order the radial quantum number of the natural orbitals with decreasing probability such that

$$\tilde{n} < \tilde{n}' \Longrightarrow p_{\tilde{n}} \geq p_{\tilde{n}'}. \tag{8.4}$$

This ordering is important for the definition of a new many-body model space truncation for the upcoming NAT-GNCSM calculation because we cannot apply the S_{max} truncation anymore.

Since we use a GNCSM reference state, the one-body density matrix inherits information about the continuum from the reference state. These admixtures are transferred into the complex eigenbasis of the one-body density matrix. The natural-orbital basis has two properties that can improve the GNCSM calculation compared to the Gamow basis. First, the natural-orbital basis is orthonormal. We can expand the nuclear matrix elements in the natural orbitals as it is done for the standard NCSM [TMR19] and can use an orthogonal eigenvalue problem solver. Second, the natural-orbital basis has a smaller basis dimension than the previous Berggren basis.

At this point, we note one possible problem of the natural orbitals. The information about the continuum is solely inherited by the reference state, which is not converged in the GNCSM calculation. Thus, it does not contain the full information about the continuum

and the generated natural orbitals are only an approximation to the one-body continuum. Hence, we trade off a decrease in the model space dimension and an orthonormal basis set for an approximation of the one-body continuum. We will investigate the impact of this approximation to the many-body results later.

8.2. Extensions towards NAT-GNCSM

Similar to the previous chapter, we discuss the necessary changes to the GNCSM in order to perform the calculations using a natural-orbital basis. First, we have to define a new model-space truncation, since the scattering truncation S_{max} is no longer applicable. Second, since the natural-orbital wave functions have a finite range, the center-of-mass Hamiltonian $\hat{H}_{\mathrm{cm}}$ can be expanded in this basis set as well. The basic concept of the NAT-GNCSM compared to the GNCSM using the Gamow basis stays unchanged.

Model Space As mentioned before, we have to define a new many-body truncation scheme because we do not have scattering states in the natural-orbital basis. The radial quantum number of the natural orbitals orders the single-particle states with respect to their occupation probability in the reference state in equation (8.1). Similar to the use of the natural orbitals in the standard NCSM, we expect the single-particle states with higher occupation probability to be more important [Con+17; TMR19]. Hence, we also use an N_{max}-type truncation with

$$N = 2\tilde{n} + l. \tag{8.5}$$

This truncation is similar to the truncation in the standard NCSM with the HO basis or the truncation for the HO partial waves in the GNCSM. However, the number N does not count the HO excitation quanta anymore. The definition of the model space now reads

$$\mathcal{M}(N_{\mathrm{max}}, M_J, \pi) = \left\{|\Phi\rangle \,:\, N(|\Phi\rangle) \leq N_{\mathrm{max}}, M(|\Phi\rangle) = M_J, \, \pi(|\Phi\rangle) = \pi\right\}, \tag{8.6}$$

which is the same definition as for the NAT-NCSM.

Remember, even though we use an N_{max}-type truncation here, we cannot use the advantages of the N_{max} truncation in the standard NCSM with the HO basis, e.g., the exact separation of the intrinsic and center-of-mass wave functions.

Center-of-Mass Spuriousity For the natural-orbital basis it is possible to expand the matrix elements of the center-of-mass Hamiltonian. Since we do not use the HO basis it can be problematic to use the center-of-mass Hamiltonian as Lawson term as defined in (2.11)

in order to shift eigenstates, which have an excited center-of-mass state, towards higher energies in the spectrum. We use the expectation value of the center-of-mass Hamiltonian to determine the physical many-body resonance states. We expect it to be small for the physical many-body resonance states compared to other discretized many-body scattering states [Pap+13]. In order to verify that this approach works accurately, we have to investigate the expectation value of the center-of-mass Hamiltonian later.

8.3. Determination of the ^{4}H Ground-State Resonance

As a first calculation in the NAT-GNCSM, we pick up the ground-state resonance of ^{4}H, which we already used for the GNCSM at the end of the previous chapter. For the NAT-GNCSM calculation, we have to analyze a few things: First, we have to decide which reference state we use. Second, we have to determine the physical resonances. Third, we have to analyze how the NAT-GNCSM results depend on the parameters and truncations of the reference state.

In the GNCSM calculation we found the one-body potential given in equation (7.9) and the truncation parameters given in equation (7.13) for the optimal calculation. For the partial-wave selection $s_{1/2}^n p_{3/2}^n$, the many-body state is a resonance and for the partial-wave selection $p_{3/2}^n$, the resonance characteristics vanished for larger values of N_{max}^{HO}. These GNCSM calculations are the first, intuitive choice for a reference state for the following NAT-GNCSM calculation. Thus, we use the eigenstate of the ground-state for $N_{max}^{HO} = 3$ and $S_{max} = 2$ for both partial-wave selections as reference state. Note, the partial waves of the Gamow basis, which are not occupied in the reference state, remain HO partial waves effectively. Thus, the natural-orbital basis depends on the HO frequency as well.

After we performed the NAT-GNCSM calculation, we have to determine the physical resonances. The calculation of an overlap with the bound-state approximation requires some additional efforts. Instead, we compute the expectation value of the center-of-mass Hamiltonian. We use the real part of the expectation value of the center-of-mass Hamiltonian since we assume physical resonances to have a small center-of-mass contributions compared to discretized many-body scattering states. In the following, we first investigate the expectation value of the center-of-mass Hamiltonian of the physical resonances in the NAT-GNCSM, and afterwards, compare the results of the GNCSM and NAT-GNCSM calculations.

In figure 8.1, we show the first results for the partial-wave selections $p_{3/2}^n$ and $s_{1/2}^n p_{3/2}^n$. The figure shows the eigenvalues and the real part of the expectation value of the center-of-mass Hamiltonian of the first two eigenstates. The ordering refers to the real part of the expectation
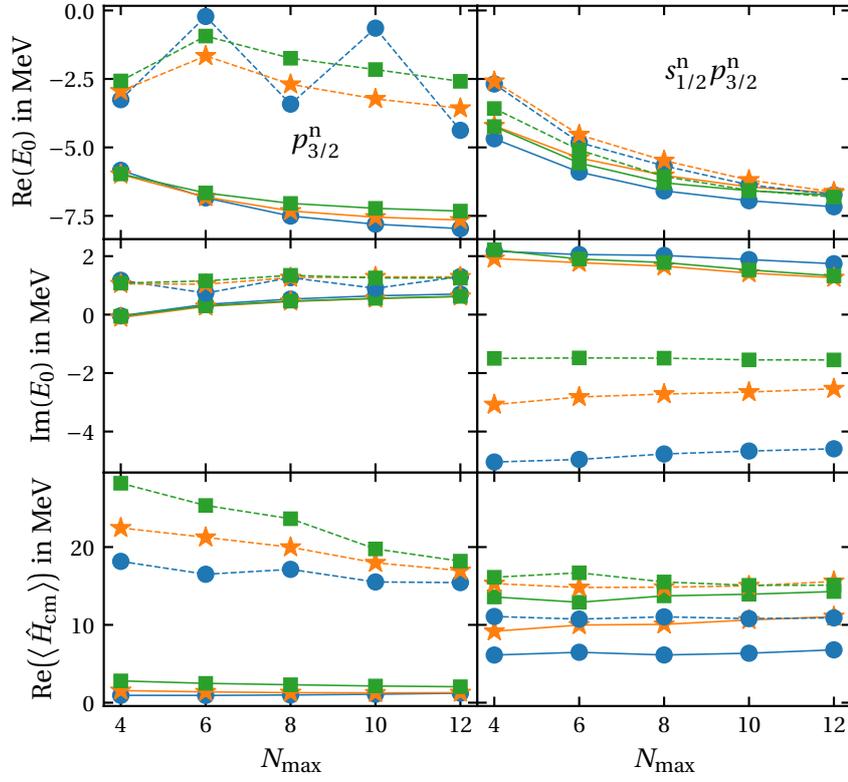
FIGURE 8.1.: Calculation of the energies of the first (━━) and second (━ ━) eigenstates of ^{4}H using the NAT-GNCSM and HO frequencies 12 MeV (●), 14 MeV (★) and 16 MeV (■). The Lawson parameter is $\lambda_{cm} = 0.2$. The two columns use different partial-wave selections in the reference state of the natural orbitals. For more information on the reference state see the text.

value of the center-of-mass Hamiltonian since we expect it to be small for physical resonances. For the $p_{3/2}^n$ partial-wave selection, we see that the real part of the expectation values of the center-of-mass Hamiltonian of the first eigenstate is small compared to the second eigenstate. Hence, we assume that the first state is the physical resonance. The real part of the energy of the first eigenstate shows the expected convergence behavior. The alternating convergence behavior of the second state can be explained as follows. There exist multiple eigenstates with a very similar expectation value of the center-of-mass Hamiltonian, such that it is not possible to determine a unique second eigenstate and the second state may alter for every step in the N_{max} sequence. The imaginary part of the corresponding eigenvalue converges

towards a positive value which coincides with the energy of reference state in the GNCSM calculation. This reference state excludes a part of the continuum, which is relevant to describe the resonance state.

If we take a look at the calculation using the $s_{1/2}^{\mathrm{n}} p_{3/2}^{n}$ partial-wave selection in the right-hand side of figure 8.1, the determination of the physical resonance becomes more complicated or rather impossible. The real part of the eigenvalue as well as the expectation value of the center-of-mass Hamiltonian are very close and overlap for different HO frequencies. In contrary to the $p_{3/2}^{\mathrm{n}}$ partial-wave selection, the convergence of the real part of the energy is very smooth and has the expected convergence behavior. One possible explanation is that these states are degenerate similar to states with similar overlaps in the previous GNCSM calculations. Regarding the imaginary part of the energy, the first state is a non-resonant state and the second state has a HO frequency-dependent negative imaginary part. It is important to note, that a negative imaginary part of the energy does not necessarily mean that it is a physical resonance. Especially, in this case where the imaginary part is heavily dependent on the HO frequency and there exists a second state with a similar or even smaller expectation value of the center-of-mass Hamiltonian, the eigenstate should be treated with caution.

For the previous figure 8.1, we already used a Lawson term as it is introduced in equation (2.11). Since the inclusion of a Lawson term alters the eigenvalue problem in the case of the NAT-GNCSM, we have to analyze the dependence of the results on the Lawson parameter carefully. The idea behind the inclusion of the Lawson term is to try to lift the degeneracy and obtain an eigenstate with a small expectation value of the center-of-mass Hamiltonian compared to the other eigenstates.

The impact of a Lawson term on the energy eigenvalues and the expectation value of the center-of-mass operator is shown in figure 8.2. The calculation without a Lawson term shows an increase of the expectation value of the center-of-mass Hamiltonian for increasing $N_{\max}$. Furthermore, we can see that the convergence behavior of the real part of the energy shows some calculations with a very large center-of-mass contamination. These contaminations are decreased if we include the Lawson term with $\lambda_{\mathrm{cm}} \le 0.2$. This also flattens the expectation value of the center-of-mass Hamiltonian with respect to $N_{\max}$. For larger values of the Lawson parameter, we can see that the eigenvalues start to shift upwards, but the expectation value of the center-of-mass Hamiltonian only changes very slightly. At this point, it is important to remember that the inclusion of a Lawson term alters the eigenvalue problem, and as a consequence, it can alter the eigenvalues since we do not have a center-of-mass separation of the many-body wave function. Therefore, we have to be careful using Lawson parameters
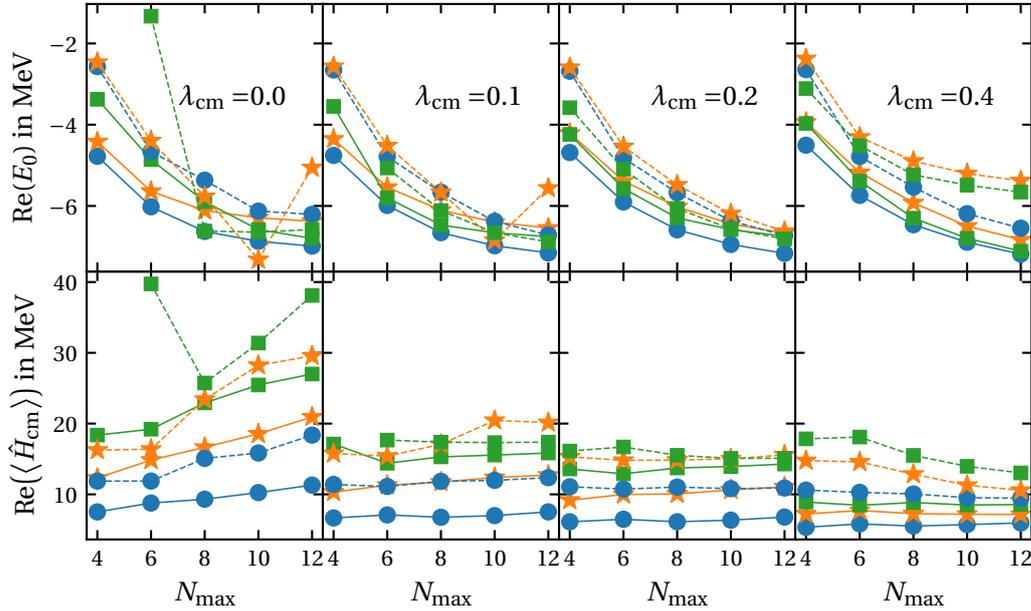
FIGURE 8.2.: Calculation of the energies of the first (━━) and second (━ ━) eigenstates of ^{4}H using the NAT-GNCSM and HO frequencies 12 MeV (●), 14 MeV (★) and 16 MeV (■). The different columns use different Lawson parameters in the Hamiltonian. The reference state uses the $s^n_{1/2}p3/2^n$ partial-wave selection.

which are to large.

In addition to the analysis of the expectation value of the center-of-mass Hamiltonian, we can compare the results of the NAT-GNCSM with the GNCSM using the Berggren basis as depicted in figure 8.3 for both partial wave combinations. For the $p^n_{3/2}$ partial-wave selection, the real and imaginary part of the energy is not completely converged for the GNCSM, but especially the imaginary part yields similar values compared to the NAT-GNCSM calculation. Hence, the natural orbitals fulfill their primary goal of enhancing the convergence rate.

If we take a look at the right-hand side of figure 8.3 for the $s^n_{1/2}p^n_{3/2}$ partial-wave selection, we observe a similar convergence pattern for the real part of the energy. However, the imaginary part of the NAT-GNCSM calculation yields different results compared to the GNCSM calculation using the Berggren basis for both states. This can have two reasons. First, the natural-orbital basis is unable to reflect the continuum information of the reference state. Second, the two states with a comparably large expectation value of the center-of-mass
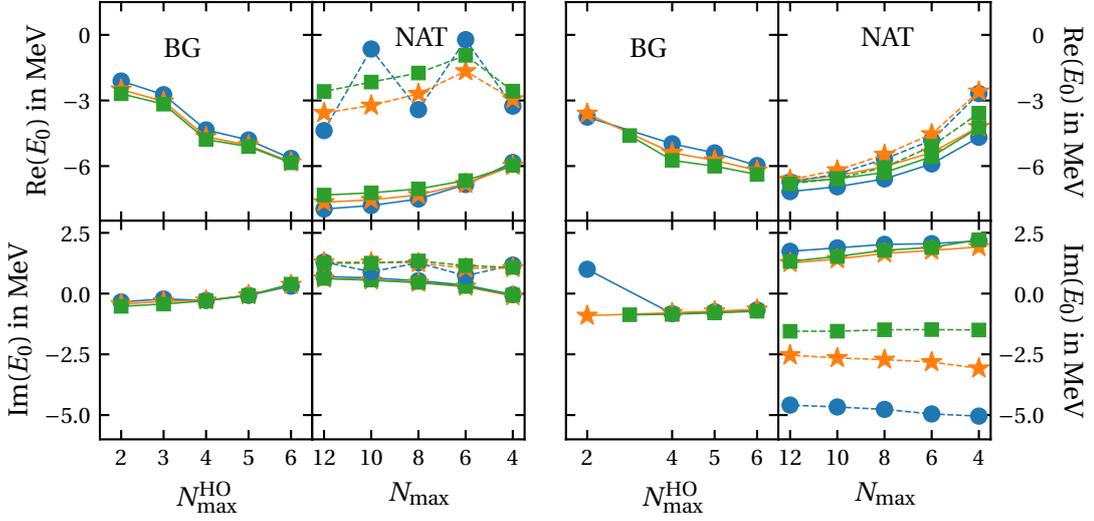
FIGURE 8.3.: Comparison of the eigenvalues of the ground-state energy of ^{4}H using the GNCSM (BG) and the NAT-GNCSM (NAT) for the $p^{\mathrm{n}}_{3/2}$ (left) and $s^{\mathrm{n}}_{1/2}p^{\mathrm{n}}_{3/2}$ (right) partial-wave selections. The HO frequencies are 12 MeV (●), 14 MeV (★) and 16 MeV (■). The NAT-GNCSM uses $\lambda_{\mathrm{cm}} = 0.2$. For further information on the Gamow basis and the reference state for the NAT-GNCSM calculation see the text.

Hamiltonian are somehow degenerate. We observed a similar behavior for the GNCSM when we found two eigenstates with similar overlap values.

Ultimately, we need to define a procedure to determine the correct physical resonances of the spectrum from the NAT-GNCSM calculation. Some points in this guideline are based on experience and caution in order to avoid problems in the results even though this might restrict the range of applicability of the GNCSM framework. Some of the following arguments are also strengthened in the next section when we investigate the dependence on the truncations of the reference state and the Gamow basis. A physical many-body eigenstate has to fulfill the following conditions.

I. The expectation value of the center-of-mass Hamiltonian of the state is positive and smaller than $\hbar\Omega$.

II. The expectation value of the center-of-mass Hamiltonian is small compared to other eigenstates in the same energy region.

III. The dependence on the HO frequency is of the same order of magnitude for the real and imaginary part of the energy.

With point I, we require the center-of-mass excitation of the intrinsic state to be rather small, similar to applications of alternative single-particle basis sets in the standard NCSM [TMR19]. Point II is motivated by the calculations using the $s_{1/2}^n p_{3/2}^n$ partial-wave selection shown in figure 8.1. The application becomes more complicated if there exist two intrinsic eigenstates with similar energies. In this case, we need the same number of eigenstates with small expectation values of the center-of-mass Hamiltonian. The third point, originates from the independence of the results on the HO frequency in standard NCSM calculations. We expect a similar behavior for a range of HO frequencies around the optimal HO frequency for the NAT-GNCSM even though the impact of the HO frequency is more complex in the GNCSM framework as we will discuss in the next section. Furthermore, point III is often times not fulfilled if II is not fulfilled as well, as can be seen for the imaginary part of the second eigenstate of the $s_{1/2}^n p_{3/2}^n$ partial-wave selection shown in figure 8.1.

8.4. Analysis of Reference State Truncations

The reference state of the natural-orbital basis we used for the previous calculations had one specific set of truncations. In general, it is not possible to determine an optimal reference state. As already discussed in the previous chapters, the reference state depends on the choice of the one-body potential in the setup of the Gamow basis as well as the model space truncations of the single-particle and many-body basis. The former is discussed in the next section and we focus on the model space truncations in this section.

Most of the truncations of the Gamow basis are either converged or we used the optimal values, e.g., the radial cutoff in the matrix element approximation. The only exception is the number of scattering states on the contour. On the one hand, more scattering states represent a better approximation of the continuum. On the other hand, the non-orthonormality of the Gamow basis gets more sever the larger the number of scattering states is. As a compromise between these two extremes, we choose a range of values for the number of scattering by hand, which yield suitable reference states. In addition to the single-particle basis truncations, the many-body model space is truncated via the $S_{\max}$ and the $N_{\max}^{\mathrm{HO}}$ truncation which already adds up to three truncations, which we have to discuss.

A rather unobvious parameter that effects the reference state is the HO frequency. On the one hand, the HO frequency is a free parameter that alters the single-particle basis and

should not affect the converged results in the many-body calculation. On the other hand, there are a lot of steps during the calculation which are affected by the HO frequency. It starts at the calculation of the nuclear matrix elements and continues in the HO partial waves of the Gamow basis. Since we use a reference state whose eigenvalues are not converged yet, the reference state and its coupling to the continuum depends on the HO frequency. Lastly, in the NAT-GNCSM calculation the HO frequency remains in the HO partial waves that were not included in the model space of the reference state. In the previous chapter, we have already seen that the convergence patterns can differ for different HO frequencies, but if the eigenstate of interest, e.g., the ground state, is determined uniquely by the expectation value of the center-of-mass Hamiltonian the dependence on the HO frequency becomes small.

We start the analysis with the reference states using the $p_{3/2}^{\mathrm{n}}$ partial wave in the reference state. Here, we are always able to find a unique ground-state in the NAT-GNCSM. Afterwards, we perform a similar analysis for the $s_{1/2}^{\mathrm{n}} p_{3/2}^{\mathrm{n}}$ partial wave selection in the reference state, where we were not able to determine a unique ground-state in the NAT-GNCSM.

Figure 8.4 shows a comparison of the ground-state energy of ^{4}H in the NAT-GNCSM for different $N_{\max}^{\mathrm{HO}}$ truncations of the reference state. For the two smaller values of the $N_{\max}^{\mathrm{HO}}$ truncation, the energies seem to converge towards different energies for different HO frequencies. In itself this is not a problem, because we do not know how the interplay between the real part and the imaginary part works. Nevertheless, it shows that the reference states are not converged, and consequently, HO frequency dependent. This dependence seems to be reduced for $N_{\max}^{\mathrm{HO}} = 4$, where the reference states are more converged. Besides the dependence on the HO frequency, the energies tend towards lower real parts and larger imaginary parts with increasing $N_{\max}^{\mathrm{HO}}$.

The second truncation parameter we need to investigate for the $p_{3/2}^{\mathrm{n}}$ partial wave is the scattering truncation $S_{\max}$. Similar to the previous figure, figure 8.5 shows the variation of the scattering truncation for the same HO frequencies. The first observation is that the energies differ for $S_{\max} = 1$ compared to the other values of $S_{\max}$. Similar to before, the energies also depend on the HO frequency, which again shows that the reference states are not converged. If we increase the scattering truncation, the energies increase slightly and the HO frequency dependence is decreased. The step from $S_{\max} = 1$ to $S_{\max} = 2$ has the largest impact in the description of the reference state and the energies do not change a lot for the subsequent step towards $S_{\max} = 3$. We have already seen this behavior for the $s_{1/2}^{\mathrm{n}} p_{3/2}^{\mathrm{n}}$ selection in the GNCSM calculation in figure 7.8, where the energies seem to be converged at $S_{\max} = 2$.

The final truncation we have to discuss is the number of scattering states in the Gamow
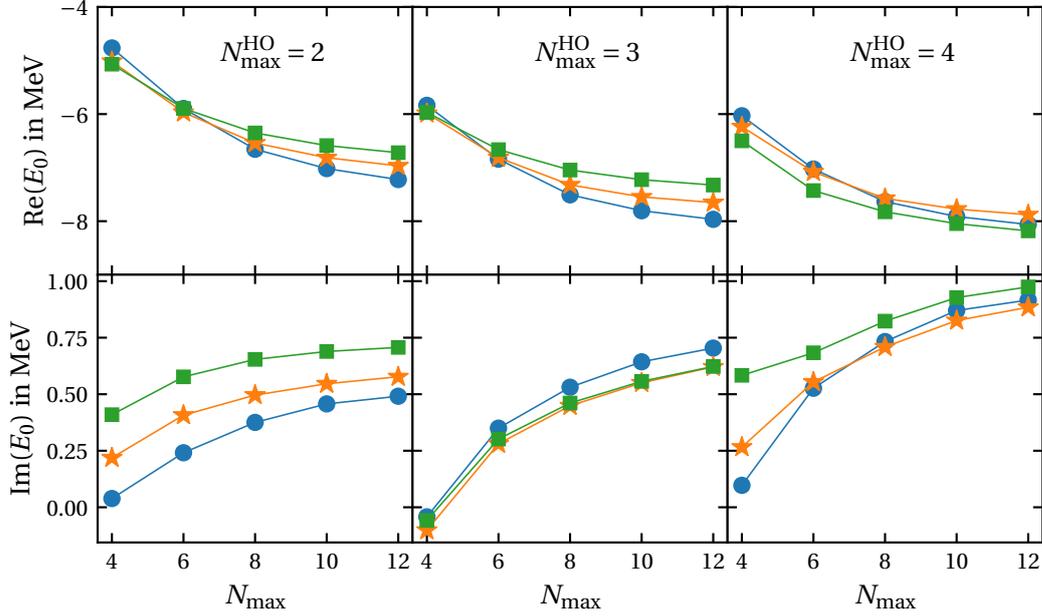
FIGURE 8.4.: Comparison of the ground-state energy and expectation value of the center-of-mass Hamiltonian of ^{4}H for HO frequencies $12\,\text{MeV}$ (●), $14\,\text{MeV}$ (★) and $16\,\text{MeV}$ (■) and the $p^{\text{n}}_{3/2}$ partial-wave selection. The columns refer to different $N^{\text{HO}}_{\text{max}}$ truncations of the reference state. The remaining truncations are $S_{\text{max}} = 2$ and $\nu_{\text{s}} = 18$. The Lawson parameter is set to $\lambda_{\text{cm}} = 0.2$.

basis, which is shown in figure 8.6. The convergence patterns for the real part fo the energy are similar for all values for the number of scattering states, but the ordering of the HO frequency changes, i.e., different HO frequencies converge towards the lowest values for the real part of the energy. The imaginary part of the energy becomes smaller and tends towards zero if we increase the number of scattering states. For this range of scattering states, none of the two aforementioned problems regarding too large or too small values for the number of scattering states plays a role here. We use $\nu_{\text{s}} = 18$ as suitable value for the upcoming calculations.

Concluding the analysis of the $p^{\text{n}}_{3/2}$ partial-wave selection, we see that the convergence behavior of the energy differs slightly if we use $S_{\text{max}} \geq 2$. Since we are not able to argue which of the combinations of truncation parameters yields the best results, we define a procedure to deduce an extrapolated energy with a corresponding many-body uncertainty based on the results for different combinations of the truncations of the reference state in section 8.6.

If we take a look at the $s^{\text{n}}_{1/2} p^{\text{n}}_{3/2}$ partial-wave selection, the dependence on the truncations
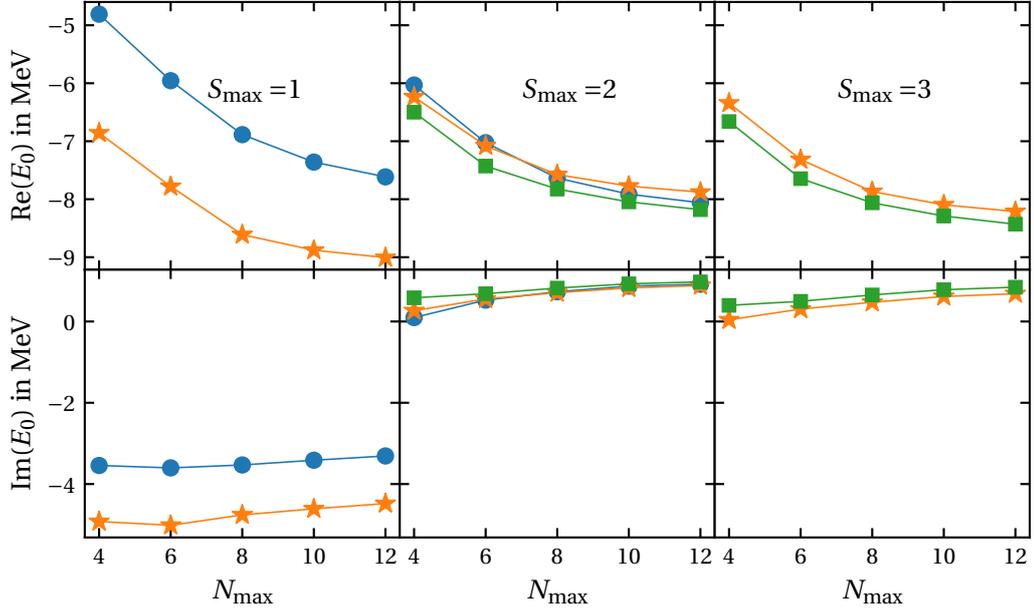
FIGURE 8.5.: Comparison of the ground-state energy and expectation value of the center-of-mass Hamiltonian of ^{4}H for HO frequencies 12 MeV (●), 14 MeV (★) and 16 MeV (■) and the $p_{3/2}^n$ partial-wave selection. The columns refer to different S_{max} truncations of the reference state. The remaining truncations are $N_{max}^{HO} = 4$ and $\nu_s = 18$. The Lawson parameter is set to $\lambda_{cm} = 0.2$.

becomes much more complicated. In the first calculations, we have already seen that the determination of a ground state is rather complicated or even impossible and we do not find a resonance state for the chosen reference state. This reference state was chosen by hand based on the results of the GNCSM calculation with the Berggren basis, i.e., $S_{max} = 2$, $\nu_s = 18$ and $N_{max}^{HO} = 3$.

We start with a variation of the scattering truncation in figure 8.7. As we have seen in the previous section, it is very complicated to determine a unique eigenstate for $S_{max} = 1$. For $S_{max} = 2$ it is slightly easier to determine the ground state with the exception of the last step in the N_{max} sequence for the smallest HO frequency. Arguably the best results are given by the calculation for $S_{max} = 3$. Not only is it possible to determine a unique ground state, but the expectation value of the center-of-mass Hamiltonian becomes very small as well. It might indicate that we need much information from the continuum to derive a good single-particle basis, which results in small center-of-mass expectation values. Keep in mind, the motivation
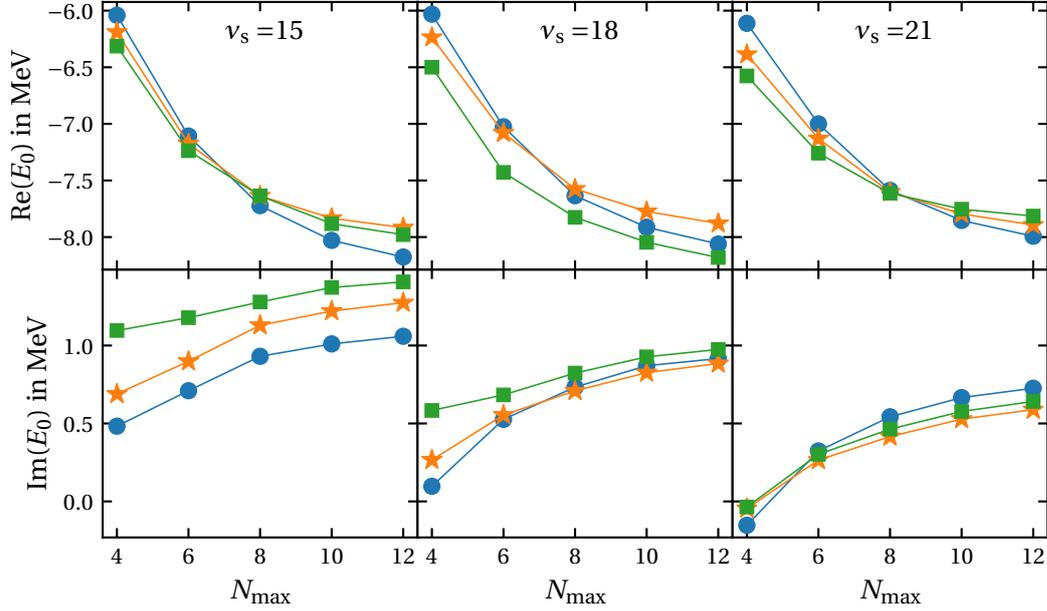
FIGURE 8.6.: Comparison of the ground-state energy and expectation value of the center-of-mass Hamiltonian of ^{4}H for HO frequencies 12 MeV (●), 14 MeV (★) and 16 MeV (■) and the $p_{3/2}^n$ partial-wave selection. The columns refer to different numbers of scattering states in the Gamow basis of the reference state. The remaining truncations are $N_{max}^{HO} = 4$ and $S_{max} = 2$. The Lawson parameter is set to $\lambda_{cm} = 0.2$.

to use the expectation value of the center-of-mass Hamiltonian is based on the HO basis and does not necessarily work in case of the natural-orbital basis. However, since we do not have any other observable to determine the ground states, we assume that smaller expectation values of the center-of-mass Hamiltonian are preferable. For the following calculation, we use $S_{max} = 3$ which also fixes the N_{max}^{HO} truncation to $N_{max}^{HO} = 2$ because of the large model space dimensions.

The variation of the remaining truncation parameter, the number of scattering states, is shown in figure 8.8. The real part of the energies depends not only on the HO frequency but also on the number of scattering states. The most interesting part is the behavior of the imaginary part of the energy. The imaginary part gives two distinct energy values for $v_s = 15$ and $v_s = 21$ compared to $v_s = 18$. This means that the admixtures of the continuum in the reference state differ depending on the number of scattering states. One indication for this, is
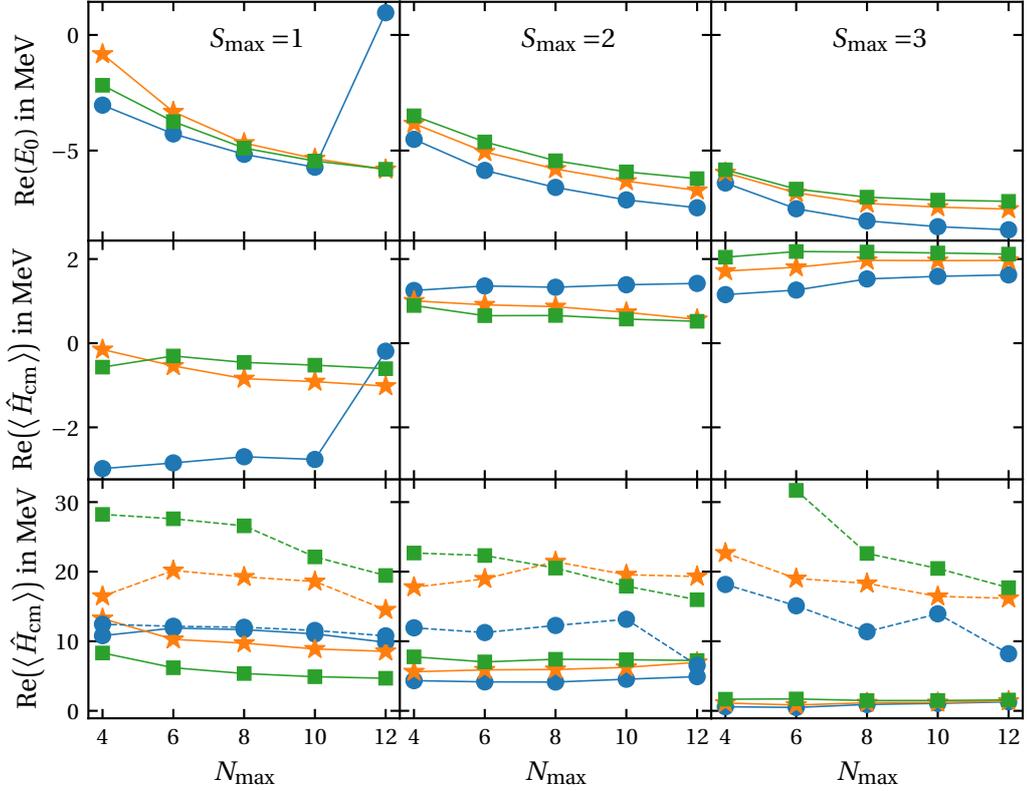
FIGURE 8.7.: Comparison of the ground-state energy and expectation value of the center-of-mass Hamiltonian of ^{4}H for HO frequencies 12 MeV ($\bullet$), 14 MeV ($\star$) and 16 MeV ($\blacksquare$) and the $s^n_{1/2}p^n_{3/2}$ partial-wave selection. The columns refer to different $S_{\max}$ truncations of the reference state. The remaining truncations are $N^{HO}_{\max} = 2$ and $\nu_s = 18$. The Lawson parameter is set to $\lambda_{cm} = 0.2$.

the overlap of the reference state with the bound-state approximation. For $\nu_s = 15, 21$, the overlaps are $\sim 25\%$, whereas the overlap for $\nu_s = 18$ is $\sim 20\%$. Even though this is not a large discrepancy, it might indicate that the reference states could differ significantly, such that the natural-orbital basis sets differ as well.

In conclusion, we demonstrated that the truncations can have a big impact on the results in the NAT-GNCSM. It is necessary to manually optimize the truncations parameters. This introduces a model dependence, but it is unavoidable in some cases. The alternative solution is to discard all calculation which do not have a similar energy convergence behavior over all variations of the truncation parameters of the reference state. In part III, we will show that the
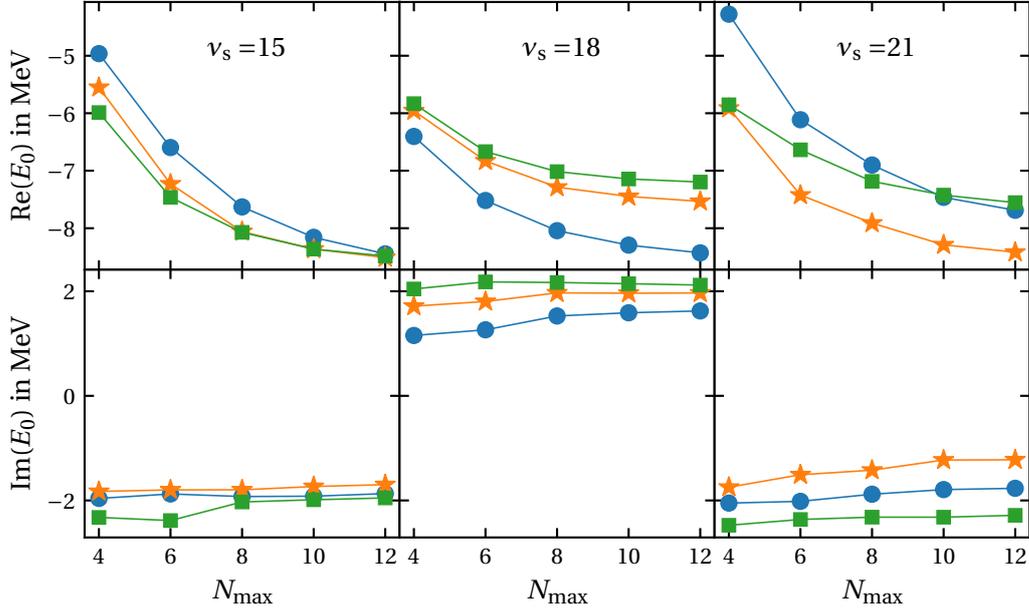
FIGURE 8.8.: Comparison of the ground-state energy and expectation value of the center-of-mass Hamiltonian of ^{4}H for HO frequencies 12 MeV ($\bullet$), 14 MeV ($\star$) and 16 MeV ($\blacksquare$) and the $s^n_{1/2} p^n_{3/2}$ partial wave combination. The columns refer to different number of scattering states in the Gamow basis of the reference state. The remaining truncations are $N^{HO}_{max} = 2$ and $S_{max} = 3$. The Lawson parameter is set to $\lambda_{cm} = 0.2$.

results do not always show these large dependencies on the reference state as we observed here for ^{4}H.

8.5. Analysis of Gamow Basis Parameters

The parameters of the Gamow basis determine the one-body potentials for the Berggren partial waves or the path of the scattering contour. In this section, we briefly discuss the influence of different one-body potentials on the NAT-GNCSM calculation. For a full analysis of the results it is necessary to go through all the steps regarding the truncations of the reference state, which we have discussed in the previous section. However, the aim of this section is not to do the full investigation again for a different one-body potential, but rather to show that there exist more parameters which impact our calculations. The chosen one-

potential number	V_{WS} in MeV	V_{LS} in MeV	a_{WS} in fm	$E_{\mathrm{b}}\left(s_{1/2}^{\mathrm{n}}\right)$ in MeV	$E_{\mathrm{r}}\left(p_{3/2}^{\mathrm{n}}\right)$ in MeV
I	-20	-25	0.67	-3.35	$0.98 - 0.84i$
II	-25	-30	0.67	-5.64	$0.47 - 0.22i$

TABLE 8.1.: List of two one-body potentials with different potential parameters for the calculation of a Gamow basis of ^{4}H. It includes the energy of the bound and resonance state in the $s_{1/2}^{\mathrm{n}}$ and $p_{3/2}^{\mathrm{n}}$ partial wave, respectively.

body potential always introduces a model dependence as we have already discussed in the last paragraph of section 7.7. Every one-body potential includes different aspects of the continuum into the Berggren partial waves. This model dependence is strongly connected to the fact that we are only able to use a small number of partial waves in the Berggren basis.

For this analysis, we only use one additional one-body potential and investigate the dependence on the $N_{\mathrm{max}}^{\mathrm{HO}}$ truncation of the reference state. The potential parameters are shown in table 8.1. The second potential we use here produces a bound and a resonance state with a smaller binding energy compared to the first potential. It was also used in previous calculations for the ^{4}H ground-state energy in the the GNCSM framework [Li+21].

A comparison of the ground-state energy of the two potentials is shown in figure 8.9. The reference state of potential I is obtained for $S_{\mathrm{max}} = 3$, $N_{\mathrm{max}}^{\mathrm{HO}} = 2$ and $v_{\mathrm{s}} = 21$ and the reference state of potential II is obtained for $S_{\mathrm{max}} = 2$, $N_{\mathrm{max}}^{\mathrm{HO}} = 3$ and $v_{\mathrm{s}} = 21$. The ground state can be determined uniquely for both calculations. The largest difference in the two calculations is the real part, which seems to converge to two different energies. For the two largest $N_{\mathrm{max}}^{\mathrm{HO}}$, the energies for potential II are $\sim 2\,\mathrm{MeV}$ larger than for potential I. The possibility that the energies of potential II correspond to an excited state were ruled out. Thus, the difference must be a consequence of the reference state.

One potential explanation for these different ground-state energies is based on empirical and experimental knowledge about the ^{4}H system. We know that the experimental ground-state energy of ^{3}H is $8.48\,\mathrm{MeV}$ [TWH87] and the ground-state energy of ^{4}H is $5.29\,\mathrm{MeV}$ [TWH92], which is $3.19\,\mathrm{MeV}$ above the n+^{3}H threshold. Taking these experimental energies into account, the ground-state energies of potential I seem to converge towards the ground-state energy of ^{3}H and the energies of potential I converge towards the ^{4}H ground-state energy. However, it is unclear whether it is even possible to describe a n+^{3}H system in the GNCSM
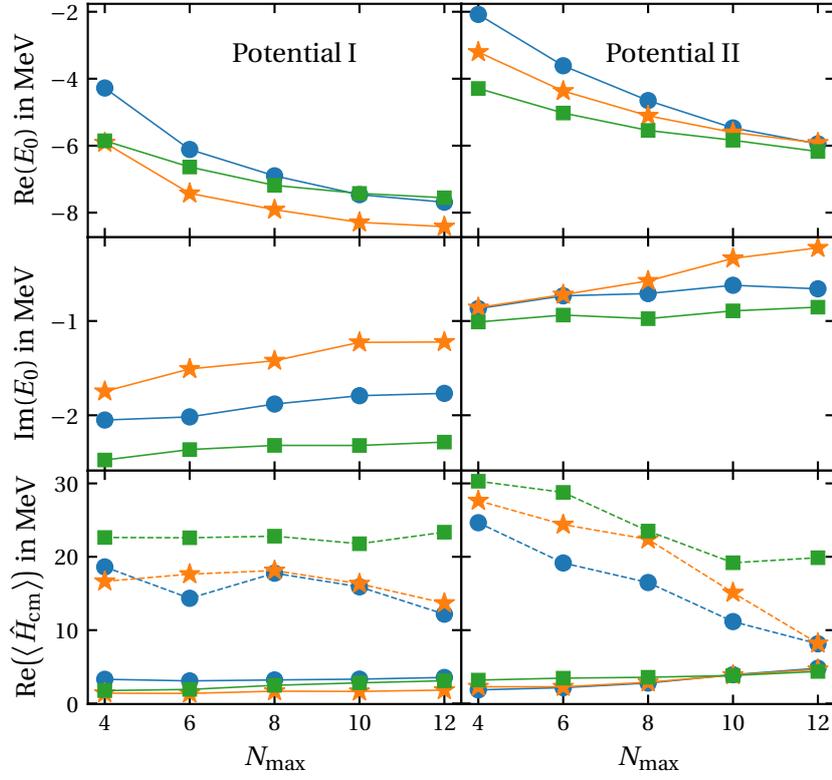
FIGURE 8.9.: Comparison of the ground-state energy and expectation value of the center-of-mass Hamiltonian of ^{4}H for HO frequencies 12 MeV (●), 14 MeV (★) and 16 MeV (■) and the $s^n_{1/2} p^n_{3/2}$ partial wave combination. The columns refer to different one-body potentials. The Lawson parameter is set to $\lambda_{cm} = 0.2$. For the truncation parameters of the reference state see the text.

framework. If this is the case, the neutron must have a vanishing wave function and zero kinetic energy. The possibility of a creation of a n+^{3}H is an interesting application for the future.

As a last analysis in this section, we show the dependence of the ground-state energy of ^{4}H on the N_{max}^{HO} truncation of the reference state for potential II in figure 8.10. This comparison shows that we converge towards the ground-state energy of ^{3}H for potential II if we use a reference state with $N_{max}^{HO} = 2$. This demonstrates that this phenomenon is not solely caused by the one-body potential of the Gamow basis, but also by the model space truncations of the reference state. Note, the results for the HO frequencies 12 MeV and 14 MeV in particular are
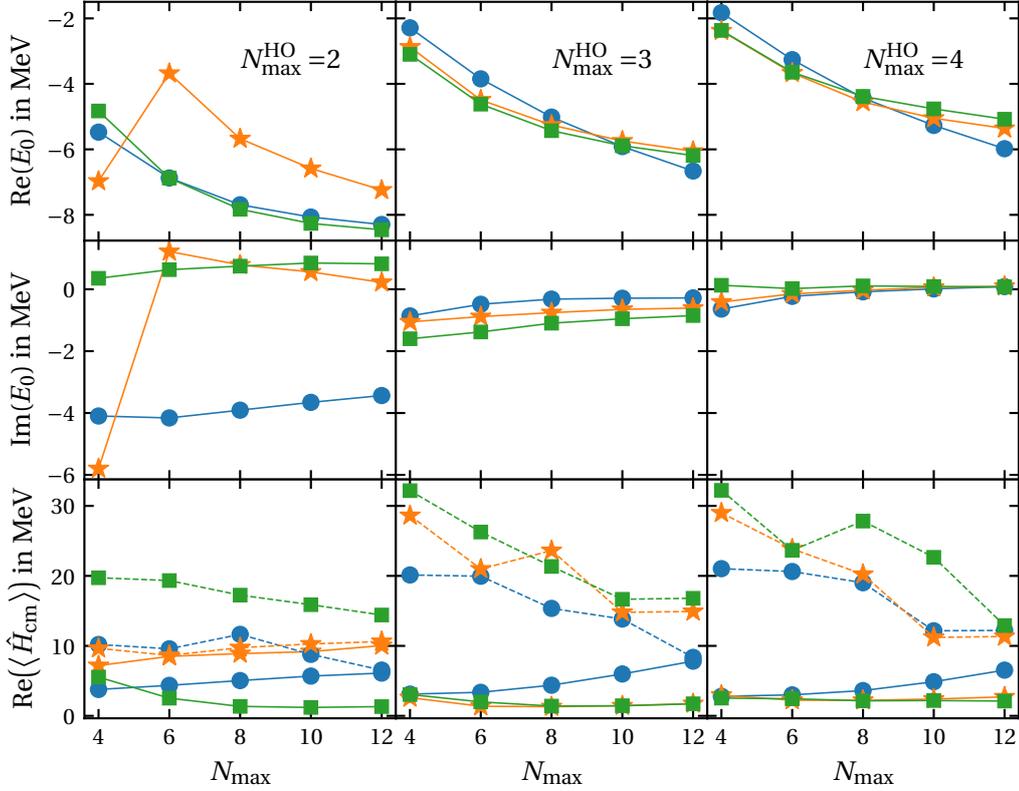
FIGURE 8.10.: Comparison of the ground-state energy and expectation value of the center-of-mass Hamiltonian of ^{4}H for HO frequencies 12 MeV ($\bullet$), 14 MeV ($\star$) and 16 MeV ($\blacksquare$) and the $s_{1/2}^{\mathrm{n}} p_{3/2}^{\mathrm{n}}$ partial wave combination. The Gamow basis is generated using Potential II. The columns refer to different $N_{\max}^{\mathrm{HO}}$ truncations of the reference state. The remaining truncations are $S_{\max} = 2$ and $\nu_{\mathrm{s}} = 18$. The Lawson parameter is set to $\lambda_{\mathrm{cm}} = 0.2$.

not unique. The imaginary part of energy of the state for 16 MeV is positive and small which indicates that it is a bound state.

The energies of the two further reference states with $N_{\max}^{\mathrm{HO}} = 3, 4$ converge towards larger real parts of the energy. The imaginary part of the energy is small and negative for $N_{\max}^{\mathrm{HO}} = 3$ and approximately zero for $N_{\max}^{\mathrm{HO}} = 4$, which corresponds to a narrow resonance and a bound state, respectively. For both calculations, we are able to determine a unique physical eigenstate with the exception of the energy for $N_{\max}^{\mathrm{HO}} = 3$, $\hbar\Omega = 12$ MeV and $N_{\max} = 12$.

In conclusion, the results of the NAT-GNCSM can heavily depend on the one-body potential

used for the Gamow basis of the reference state. This requires some physical motivation for the definition of the one-body potential, and consequently, creates a model dependence for the final energy eigenvalues. In addition to the dependence on the Gamow basis of the reference state, it is also possible that the converged energy eigenvalues differ depending on the reference state. In the next section, we develop a method to extrapolate the energy eigenvalue for the real and imaginary part of the energy and calculate statistical and systematic uncertainties.

8.6. Extrapolation and Uncertainty Quantification

The final step in the development of the GNCSM framework is the extrapolation of the energy eigenvalues for the $N_{\max}$ sequences in the NAT-GNCSM. In addition, we would like to quantify an uncertainty to the extrapolated energy. The extrapolation and uncertainty quantification is not straight forward, since we have seen that we are not able to determine an optimal reference state, which we could use for the following NAT-GNCSM calculation. Therefore, we use a statistical approach to determine a mean extrapolated energy with a standard deviation for a set of $N_{\max}$ sequences that converge towards the same results. Note, the deviations of the results are not a consequence of any statistical method used during the calculations, but strictly speaking, small systematic uncertainties that a generated by different reference state truncations. However, for the calculation of a final result, we treat these small systematic uncertainties as statistical uncertainties. In our approach to calculate an uncertainty, a systematic uncertainty describes calculations that converge towards to different results as we will see later. Those systematic uncertainties are treated separately to the statistical uncertainty. We start this section with the extrapolation of a single $N_{\max}$ sequence. Afterwards, we combine the extrapolated results to determine a mean extrapolated energy, a statistical uncertainty and a systematic uncertainty.

Extrapolation For the extrapolation of an $N_{\max}$ sequence, we treat the real and the imaginary part of the energy separately. For the real part of the energy, we use an exponential function

$$E_{\mathrm{R}}(N_{\max}) = a \cdot \exp(-bN_{\max}) + E_{\mathrm{R}}^{\infty} \tag{8.7}$$

with the parameters a, b and $E_{\mathrm{real}}^{\infty}$. The latter is the extrapolated real part of the eigenvalue for an $N_{\max}$ sequence. This exponential ansatz is frequently used for ground-state energies in the standard NCSM [MVS09] since the energy decreases monotonically and converges

for $N_{\mathrm{max}} \to \infty$. Note, the variational principle and the monotonic decrease of the energy eigenvalues does not formally hold for rigged Hilbert spaces. Nevertheless, all previous calculations have shown such a monotonic decrease of the energy eigenvalues of the ground states.

In case of the imaginary part of the energy, we are unable to detect any convergence patterns. The only observation we can make is that the variation of the imaginary part of the energy with respect to N_{max} is usually smaller than the variation of the real part. Therefore, we use the value of the imaginary part of the energy for the largest N_{max}.

Statistical Mean and Uncertainty   As already mentioned, we are not able to determine an optimal reference state, and consequently, cannot favor one extrapolated value. In order to combine all the extrapolations for all N_{max} sequences for different reference states, we apply a statistical ansatz and use a set of reference states. For this set of reference states, we use fixed parameters of the Gamow basis and only vary the truncations of the GNCSM calculation, i.e., v_{s}, $N_{\mathrm{max}}^{\mathrm{HO}}$, S_{max}, and $\hbar\Omega$. Since we have already seen that the NAT-GNCSM calculations can be very sensitive with respect to these parameters, it is often necessary to manually filter the N_{max} sequences. In the following, we usually use three values for v_{s} and $N_{\mathrm{max}}^{\mathrm{HO}}$ as well as one or two values for S_{max}. The latter is usually the most unstable and often the only calculations that yield suitable results use $S_{\mathrm{max}} = 2$.

The variation of the HO frequency is a little more complicated. It affects the convergence of the GNCSM and the NAT-GNCSM calculations via the HO partial waves. In the standard NCSM, we usually use the HO frequency with the best model space convergence for the extrapolation. We adopt this ansatz for the NAT-GNCSM. The best HO frequency in the NAT-GNCSM has the smallest extrapolated real part of the energy. In order to take the HO frequency dependence of the reference state into account as well, we use the second best HO frequency for our statistical approach, too. The imaginary part is not the included in the procedure to determine the best HO frequencies.

The combination of all truncations ideally results in

$$n_{\mathrm{ref}} = \#v_{\mathrm{s}} \cdot \#N_{\mathrm{max}}^{\mathrm{HO}} \cdot \#S_{\mathrm{max}} \cdot \#\hbar\Omega \qquad (8.8)$$

different reference states. However in practice, typical numbers of suitable and stable reference states are $n_{\mathrm{ref}} \in [5, 15]$. For the final result of the set of NAT-GNCSM calculations, we use the statistical mean energy with the corresponding standard deviation for the real and imaginary part, respectively. Note, since we only use mean and standard deviation for the

calculation of our final result, the exact number of reference states is not very important, such that it is not a problem if we have to discard the calculations for some reference states.

Systematic Uncertainty   It is possible that the calculations converge towards two distinct energy eigenvalues. In this case, it is not useful to calculate a single extrapolated energy using the statistical ansatz from above, but to compute the statistical mean and uncertainty for both distinct energies and define a systematic uncertainty as the difference between the two mean values

$$\Delta E_{\text{R/I}}^{\text{sys}} = \left| \bar{E}_{\text{R/I}}(1) - \bar{E}_{\text{R/I}}(2) \right| \tag{8.9}$$

for the real (R) and imaginary (I) part of the energies, respectively. If we are interested in a combined uncertainty, we can use the Gaussian propagation of statistical and systematic uncertainties.

Application of Extrapolation with Uncertainties   In order to apply the previous definitions of statistical means and uncertainties as well as systematic uncertainties, we return to the ground-state energy of ^{4}H using the Gamow basis constructed with potential II from section 8.5. Since we found that the energy eigenvalues for the reference states with a $N_{\text{max}}^{\text{HO}} = 2$ truncation converged towards the ground-state energy of ^{3}H, we exclude all reference states with $N_{\text{max}}^{\text{HO}} = 2$ for the extrapolation of the ground-state energy of ^{4}H. In addition, we only use $S_{\text{max}} = 2$ because for smaller values of S_{max} the reference state does not include enough information from the continuum and for larger values of S_{max} it was impossible to find a unique eigenstate. Figure 8.11 shows the N_{max} sequences of the NAT-GNCSM calculation using the remaining reference states. For the real part of the energy we can see very clearly that the N_{max} sequences converge towards two different energy eigenvalues. The statistical uncertainty of the real part is much smaller than the systematic uncertainty. This situation changes for the imaginary part of the energy. Especially, the imaginary part of the energy for the first state with a smaller real part of the energy has a large statistical uncertainty. For the second state, the statistical and systematic uncertainties have a similar size.

Similar to the discussion regarding the GNCSM calculations, it is not easy to decide which of these two extrapolated energies is better or more trustworthy at this point.
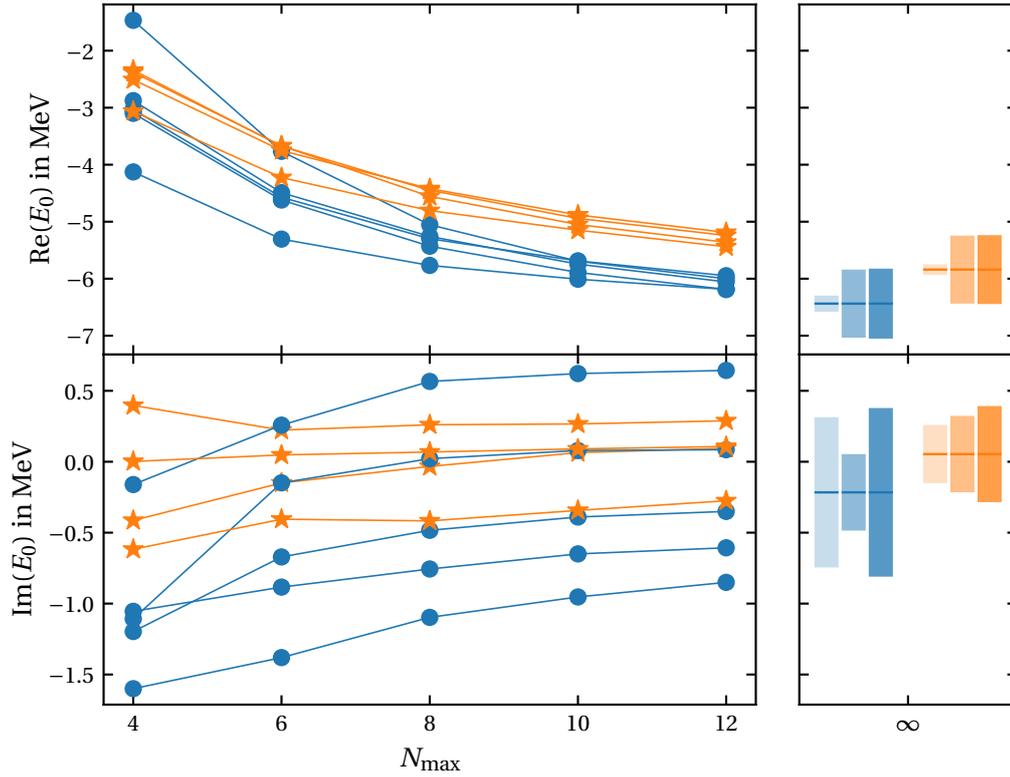
FIGURE 8.11.: Determination of statistical and systematic uncertainties for the ground-state energy of ^{4}H for the first (●) and second (★) eigenstate and a set of GNCSM reference states with $N_{max}^{HO} \in [3,4]$, $\nu_s \in [15,18,21]$ and $S_{max} = 2$. The right column shows the extrapolated eigenvalue (—) with the statistical (▬), systematic (▬) and combined (▬) uncertainties for the respective eigenstate. The Lawson parameter is set to $\lambda_{cm} = 0.2$.

PART III.

RESULTS

9

RESONANCES IN LIGHT NUCLEI

The development of the GNCSM framework is completed and we can start with the applications following the steps of part II. In this section, we will apply the GNCSM framework to investigate light nuclei that have a ground-state or excited-state resonance. Firstly, we calculate the resonance states of $A = 4$ nuclei with $J^\pi = 2^-$. We can compare our results with the GNCSM calculation by Li et al. [Li+21]. In the next step, we analyze the first three excited states of ^{4}He, which are all resonances. As a final application in this chapter, we take a look at the heavier helium isotopes ^{5}He and ^{6}He.

For all calculations in this section, we use a pure NN interaction by Entem, Machleidt and Nosyk [EMN17] with a SRG evolution with a flow parameter $\alpha = 0.08\,\text{fm}^4$ [BFP07; Rot+11]. The inclusion of explicit 3N interactions is straight forward, but produces an increase in the memory and time consumption of the numerical calculations. Furthermore, we will see in chapter 10 that we can assume that the contributions of the 3N interactions are very small.

For the GNCSM calculations (cf. chapter 7), we use the truncations

$$
\begin{aligned}
k_{\max} &= 3\,\text{fm}^{-1}, & R_{\text{cut}} &= 10\,\text{fm}, \\
e_{\max} &= 24, & l_{\max} &= 5.
\end{aligned}
\tag{9.1}
$$

The partial-wave selection, which truncates the continuum in the GNCSM, is adapted individually for each nucleus (cf. section 5.3). The remaining truncations in the GNCSM reference states, ν_s, $N_{\max}^{\text{HO}}$ and $S_{\max}$, are varied in order to determine the mean energy and uncertainty

as discussed in section 8.6. For the basis parameters, we use the two potentials shown in table 8.1 and a set of HO frequencies with an upper bound of 16 MeV as discussed in chapter 6.

9.1. The 2^- States in $A = 4$ Isobars

The first application of the GNCSM framework targets the $A = 4$ isobars ^{4}H, ^{4}Li, and ^{4}He. In particular, we are interested in the first 2^- eigenstate of these nuclei, which is the ground state for ^{4}H and ^{4}Li and an excited state for ^{4}He. The ground-state resonance energies of the former two nuclei are of special interest because the experimental and theoretical results are inconclusive for both nuclei as presented in tables 9.1 and 9.2. In case of ^{4}H, the real part of the ground-state energy varies between 1.60 MeV to 3.19 MeV above the n+^{3}H threshold and the width varies between 0.40 MeV to 5.42 MeV, depending on the experiment or the theoretical calculation [TWH92; Bla+91; Sid+04; Gur+05; LHC19; Li+21]. Similarly for ^{4}Li, the real part of the ground-state energy varies between 2.70 MeV to 4.07 MeV above the p+^{3}He threshold and widths of 0.80 MeV to 6.03 MeV for different experimental and theoretical calculations [TWH92; Bru+90; Bri+90; Li+21]. Note, there are two important things to keep in mind regarding the energies above the threshold. First, the theoretical calculations use different chiral interactions. The calculations by Lazauskas et al. and Li et al. use the interaction by Entem and Machleidt [EM03], whereas we use the interaction by Entem, Machleidt, and Nosyk [EMN17]. Second, the experimental ground-state energy of the ^{3}H can differ from the theoretical calculations.

The ground-state resonance of ^{4}H was already investigated extensively throughout part II. Hence, we use the results already shown in figure 8.11 for potential II and the $s_{1/2}^n p_{3/2}^n$ partial-wave selection. In case of the mirror nucleus ^{4}Li, we followed the same steps using potential I, which, compared to potential II, produces a slightly weaker bound state in the $s_{1/2}$-wave and broader resonance state in the $p_{3/2}$-wave, and the $s_{1/2}^p p_{3/2}^p$ partial-wave selection. We chose this one-body potential since the reference states were more stable and included more admixtures of the continuum.

In case of ^{4}He, the first 2^- state is an excited state, which is more challenging in the GNCSM calculation. It can become complicated to compute physical eigenstates of excited states in the GNCSM, since the spectrum gets filled with discretized many-body scattering states. Therefore, the calculation of the excited state was not possible in the GNCSM and we used the natural orbitals generated by the 0^+ ground state of ^{4}He, which converges towards a bound state. However, in the small model spaces we also observed continuum admixtures in these

	$E_{\mathrm{r}}\left(^{4}\mathrm{H}\right)$ in MeV	$\Gamma_{\mathrm{r}}\left(^{4}\mathrm{H}\right)$ in MeV
Tilley et al. [TWH92] (ex.)	3.19	5.42
Blagus et al. [Bla+91] (ex.)	3.1	2.3
Sidorchuk et al. [Sid+04] (ex.)	3.05(19)	4.2(10)
Gurov et al. [Gur+05] (ex.)	1.6	0.4(1)
Lazauskas et al. [LHC19] (th.)	1.15(5)	3.97(7)
Li et al. [Li+21] (th.)	1.7	0.9
this work	2.02(14)	0.4(10)
	2.78(32)	0.05(39)

TABLE 9.1.: Comparison of the resonance energy of the ground state of ^{4}H for different experimental (ex.) and theoretical (th.) calculations. The resonance energy is given with respect to the n+^{3}H threshold.

	$E_{\mathrm{r}}\left(^{4}\mathrm{Li}\right)$ in MeV	$\Gamma_{\mathrm{r}}\left(^{4}\mathrm{Li}\right)$ in MeV
Tilley et al. [TWH92]	4.07	6.03
Bruno et al. [Bru+90]	3.3	0.8
Brinkmöller et al. [Bri+90]	3.3	1.0
Li et. al. [Li+21]	2.7	2.0
This work	2.94(23)	1.76(22)

TABLE 9.2.: Comparison of the resonance energy of the ground state of ^{4}Li for different experimental (ex.) and theoretical (th.) calculations. The resonance energy is given with respect to the p+^{3}He threshold.

reference states. Thus, we want to investigate to what extent this continuum information can be used to describe an excited state in ^{4}He. The GNCSM calculation for ^{4}He uses potential II and we select the $p_{3/2}^{\mathrm{n}}$ partial wave after we found that the $p_{3/2}^{\mathrm{n}}$, $p_{3/2}^{\mathrm{p}}$, and $p_{3/2}^{\mathrm{pn}}$ partial-wave selections yield similar results and the inclusion of s-wave partial waves leads to unstable results.

In figure 9.1, we show the energy convergence of the first 2⁻ resonance states of the $A = 4$
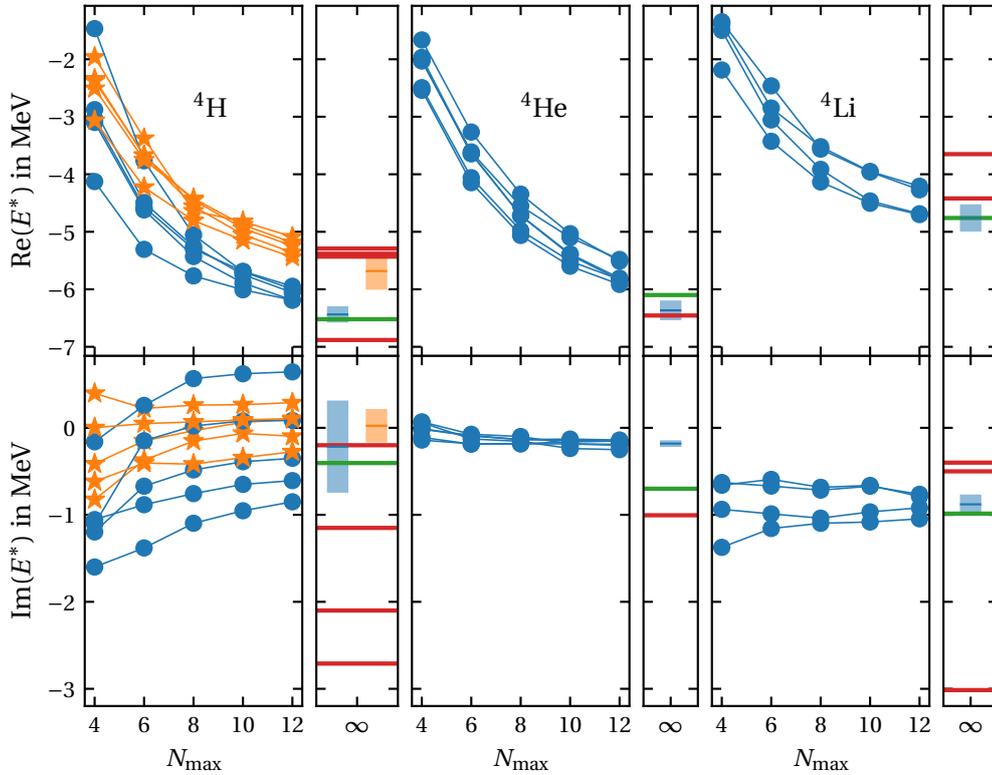
FIGURE 9.1.: Comparison of the energy of the first 2^- states resonances of the $A = 4$ isobars ^{4}H, ^{4}He, and ^{4}Li. The colors show the first (●) and the second (★) possible eigenstates. The extrapolated eigenvalue (▬) and the statistical (▬) uncertainty are depicted next to the energy sequences. The results are compared to the calculations by Li et al. (▬) [Li+21] and the experimental result shown in tables 9.1 and 9.2 as well as Tilley et al. for the excited state in ^{4}He (▬) [TWH92; Bla+91; Sid+04; Gur+05; Bru+90; Bri+90].

isobars. Compared to the energy sequences of ^{4}H, the other two nuclei yield more stable results, especially for the imaginary part. If we compare the mirror nuclei ^{4}H and ^{4}Li, we can observe that the real part of the energy is larger and the imaginary part of the energy is smaller for ^{4}Li. This is an expected consequence of the Coulomb force. For the ground-state energy of ^{4}H, the results are in agreement with the results obtained by Li et al. [Li+21] for both parts of the energy if we use the energy sequence with a smaller extrapolated real part of the energy. Compared to the experimental results, the real part lies in between the experimental

results and the imaginary part is close to the results by Gurov et al. [Gur+05].

In case of the ground-state energy of ^{4}Li, the results also agree with the results by Li et al. The real part of the energy appears to converge towards two different energy values as well, but since the number of robust reference states is very small and the difference in the extrapolated energies is rather small, we have decided to assign them to a single extrapolated energy with a larger statistical uncertainty. In order to improve the uncertainty quantification, it is necessary to increase the number of reference states, e.g., by using a larger variation of ν_s. Compared to the experimental results, our results are close to the results by Bruno et al. [Bru+90] and Brinkmöller et al. [Bri+90].

In case of ^{4}He, the real part is described very well compared to the theoretical [Li+21] and experimental [TWH92] results. In contrast, the imaginary part of the energy is underestimated, which can be a consequence of the reference state we use for the natural orbitals. The bound state of ^{4}He might not include enough information about the continuum of the respective excited states. In order to improve this, we have to extend the calculations of the reference states in the GNCSM, such that it is possible to use the respective excited state from the GNCSM calculation as reference state.

The first applications of the GNCSM framework demonstrate two things. We are able to produce comparable results to other implementations of the GNCSM framework [Li+21] with the addition of a suitable uncertainty quantification. This also indicates that the results are rather independent of the choice of the chiral interaction for these nuclei. Furthermore, it shows the difficult search for reference states, which yield suitable and robust results. This has been most problematic for the calculation of ^{4}Li, where only four calculations yield suitable reference states. In future endeavors, this needs to be improved in order to optimize the extrapolation and uncertainty quantification. One idea is to vary the parameters in the Gamow basis, since we have seen that the stability of the results can heavily depend on the one-body potential.

9.2. The ^{4}He Energy Spectrum

The next application of the GNCSM framework focuses on the spectrum of ^{4}He. In the previous section, we have already discussed the first 2^- state, which is the third excited state in total. Similar to before, we use the $p_{3/2}^n$ partial-wave selection and the bound 0^+ eigenstate as reference state for the natural orbitals.

The first three excited states of ^{4}He are shown in figure 9.2 with increasing energy from left
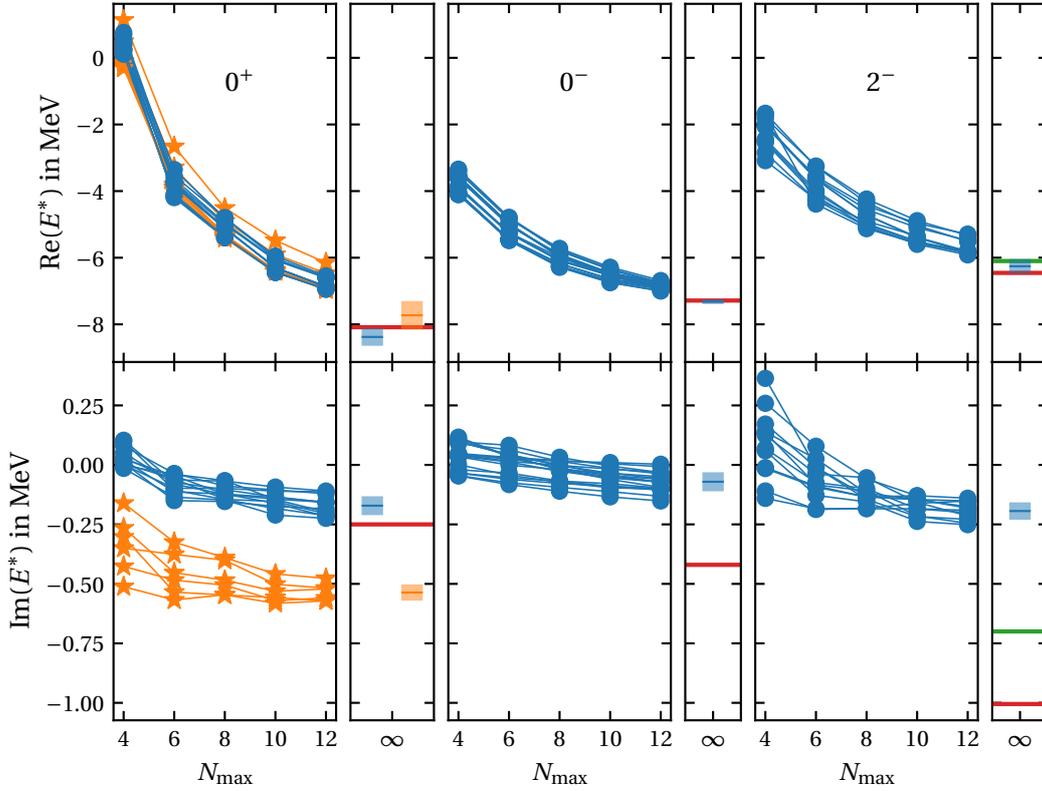
FIGURE 9.2.: Eigenvalues of the first three eigenvalues of the excited states of the ^{4}He energy spectrum. The colors show the first (●) and the second (★) possible eigenstates. The extrapolated eigenvalue (━) with the statistical (▬), systematic (▬) and combined (▬) uncertainties are depicted next to the energy sequences. The results are compared to Li et al. (━) [Li+21] and the experiment (━) [TWH92].

to right, respectively. At first look, the results are very stable compared to the ground state of ^{4}H, which we discussed thoroughly throughout part II. The first excited 0^+ state shows two systematically different imaginary parts of the energy, which we treated separately. If we assume a variational principle here, the mean and uncertainties on the left-hand side should be chosen as best result for this calculation. In this case, the real part slightly underestimates the experiment, whereas the imaginary part overestimates the experimental result. However, we have to keep in mind that we do not include 3N contributions to the interaction.

For the other two excited states, there only exists a single set of energy sequences that

converge towards a similar value. The real part of the energy is described by the NAT-GNCSM results very well compared to the experimental results [TWH92], but the imaginary part is underestimated. This might be a consequence of the reference state of the natural orbitals, which is the bound state of ^{4}He. In addition, the continuum structure of eigenstates with unnatural parity may be completely different, which requires some further investigation using a reference state with unnatural parity as well.

9.3. Heavier Helium Isotopes

The last application of this chapter regards two heavier isotopes of the helium chain, i.e., the ground-state resonance of ^{5}He and the first two excited-state resonances of ^{6}He. Similar to the first application to $A = 4$ isobars, the experimental results of these two heavier helium isotopes are inconclusive as well, which is shown in tables 9.3 and 9.4 for ^{5}He and ^{6}He, respectively. Additionally, we show the results of our calculations and other NCSM frameworks, the GNCSM with the density matrix renormalization group (GNCSM+DMRG) [Pap+13] and the NCSM/RGM [Rom+14], which include the continuum as well. Similar to before, we have to keep in mind that the threshold energy of the ^{4}He ground-state varies for the experiment and the theoretical calculations and that the chiral interactions of the theoretical calculations differ. The theoretical calculations by Papadimitriou et al. [Pap+13] and Romero-Redondo et al. [Rom+14] use the interaction by Entem and Machleidt [EM03], whereas we use the interaction by Entem, Machleidt, and Nosyk [EMN17]. In section 9.1, we found that the specific choice of the chiral interaction does not affect the calculations of the $A = 4$ isobars very much, such that it is interesting to investigate if this holds for the heavier helium isotopes as well.

We start with the ground state of ^{5}He, which is a $\frac{3}{2}^-$ state. We expect the nucleus to consist of a strongly bound ^{4}He core and a loosely bound neutron in the $p_{3/2}$ shell. Thus, we use the $p_{3/2}^n$ partial-wave selection and potential I for the reference states. The energy sequence of the NAT-GNCSM calculation is shown on the left-hand side of figure 9.3 for a set of suitable reference states. Since the model-space dimensions increase rapidly with particle number A, we are limited to $N_{max} \leq 10$. The real part of the ground-state energy is extrapolated to

$$\mathrm{Re}\left[E_0\left(^5\mathrm{He}\right)\right] = -28.47(33)\,\mathrm{MeV}, \tag{9.2}$$

which is

$$E_\mathrm{r}\left(^5\mathrm{He}\right) = 0.59(34)\,\mathrm{MeV} \tag{9.3}$$

Method	$E_{\mathrm{r}}\left(^5\mathrm{He}\right)$ in MeV	$\Gamma_{\mathrm{r}}\left(^5\mathrm{He}\right)$ in MeV
Tilley et al. [Til+02] (ex.)	0.798	0.648
	0.963	0.985
Bond et al. [BF77] (ex.)	0.771	0.644
Papadimitriou et al. [Pap+13] (th.)	1.17	0.4
This work	0.59(33)	0.51(24)

TABLE 9.3.: Comparison of the resonance energy of the ground state of ^{5}He for different experimental (ex.) and theoretical (th.) calculations. The resonance energy is given with respect to the n+^{4}He threshold.

Method	$E_{\mathrm{r_1}}\left(^6\mathrm{He}\right)$ in MeV	$\Gamma_{\mathrm{r_1}}\left(^6\mathrm{He}\right)$ in MeV	$E_{\mathrm{r_2}}\left(^6\mathrm{He}\right)$ in MeV	$\Gamma_{\mathrm{r_2}}\left(^6\mathrm{He}\right)$ in MeV
Jänecke et al. [Jän+96] (ex.)	0.92(17)		4.6(0.3)	12.1(11)
Mougeot et al. [Mou+12] (ex.)	0.824	0.113	1.63(3)	1.6(4)
Romero-Redondo et al. [Rom+14] (th.)	1.24	0.16	2.6	1.17
This work	1.55(0.34)	2.62(1.3)	4.90(44)	1.26(88)

TABLE 9.4.: Comparison of the resonance energy of the first two excited 2^+ states of ^{6}He for different experimental (ex.) and theoretical (th.) calculations. The resonance energy is given with respect to the n+n+^{4}He threshold.

above the n+^{4}He threshold energy of

$$E_0\left(^4\mathrm{He}\right) = -29.06(1)\,\mathrm{MeV}. \tag{9.4}$$

The resonance width is extrapolated to

$$\Gamma_{\mathrm{r}}\left(^5\mathrm{He}\right) = 2\mathrm{Im}\left[E_0\left(^5\mathrm{He}\right)\right] = 0.51(24)\,\mathrm{MeV}. \tag{9.5}$$

These extrapolated energy values are in the same region as the experimental results and another theoretical calculation using the GNCSM+DMRG, which are shown in table 9.3. The many-body uncertainty of our calculation, includes almost all remaining results. The GNCSM+DMRG calculation does not use a natural-orbital basis to optimize the calculation. Instead, it uses the DMRG to efficiently diagonalize the Hamilton matrix [Pap+13].
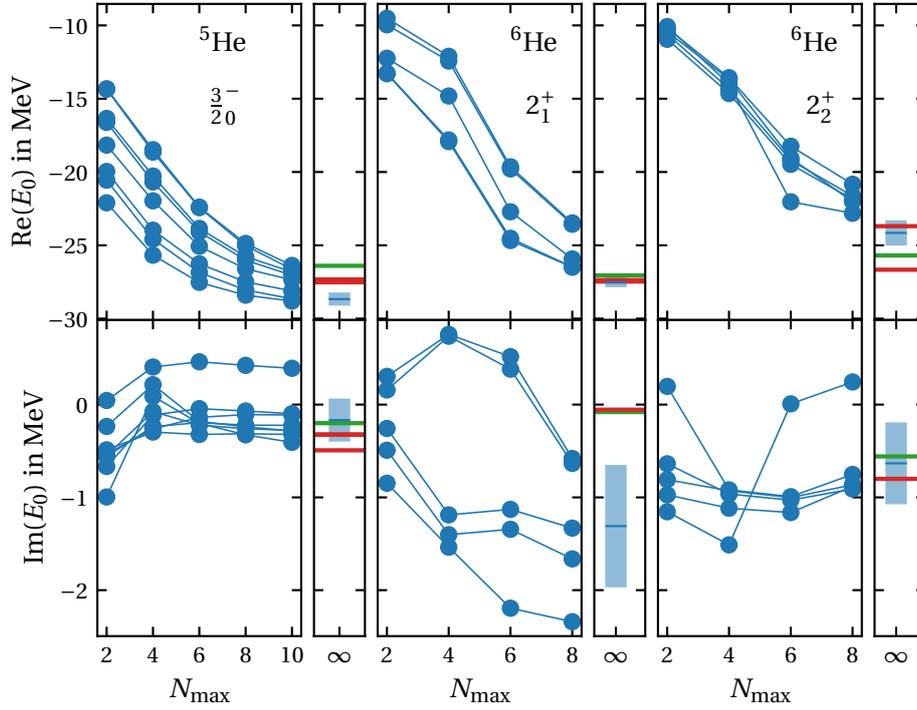
FIGURE 9.3.: The ground-state resonance energies of ^{5}He and the first two excited 2^+ states of ^{6}He for a set of reference states. The extrapolated eigenvalues (——) with the statistical (▬) uncertainties are depicted next to the energy sequences. The results are compared to theoretical (——) [Pap+13; Rom+14] and the experimental (——) [Mou+12; BF77; Til+02] results. The imaginary part of the result by Jänecke et al. [Jän+96] for the second excited state of ^{6}He is outside the scope of the plot.

In case of the first two excited 2^+ state resonances of ^{6}He, we use the $s_{1/2}^n p_{3/2}^n$ partial-wave selection with the one-body potential I for the reference state. Hence, compared to the previous calculation for the ^{5}He ground-state, we have to include the $s_{1/2}^n$ partial wave to the reference state in order to include enough information about the continuum to our reference state. The scattering truncation is set to $S_{max} = 1$ in order to keep the model space dimensions manageable.

The energy sequences for the two excited states are shown on the right-hand side of figure 9.3. For ^{6}He, we are limited to $N_{max} \leq 8$ in the NAT-GNCSM, which is reflected in comparably large uncertainties for the extrapolated eigenvalues. In contrast to the ground-state energy of

^{4}He, which showed a systematic uncertainty for the real part of the energy, the two different extrapolated eigenvalues correspond to two different excited states for ^{6}He. The real parts are extrapolated to

$$\text{Re}\left[E_1\left(^6\text{He}\right)\right] = -27.51(34)\,\text{MeV}, \tag{9.6}$$

$$\text{Re}\left[E_2\left(^6\text{He}\right)\right] = -24.16(86)\,\text{MeV}, \tag{9.7}$$

which is

$$E_{\text{r}_1}\left(^6\text{He}\right) = 1.55(34)\,\text{MeV}, \tag{9.8}$$

$$E_{\text{r}_2}\left(^6\text{He}\right) = 4.90(44)\,\text{MeV} \tag{9.9}$$

above the n+n+^{4}He threshold with a width of

$$\Gamma_{\text{r}_1}\left(^6\text{He}\right) = 2.620(13)\,\text{MeV}, \tag{9.10}$$

$$\Gamma_{\text{r}_2}\left(^6\text{He}\right) = 1.26(88)\,\text{MeV}. \tag{9.11}$$

Compared to other experimental and theoretical results, the real part of the energy is described very good for the first excited state. For the second excited state, the real part is comparable with the results by Jänicke et al. [Jän+96]. The imaginary part is overestimated for the first excited state compared to the other results. Surprisingly, the resonance width of the second excited state is smaller than resonance width of the first excited state, which is uncharacteristic. This could be a consequence of the reference state from the GNCSM, which is the first excited 2^+ state. On the other hand, the width of the first excited state is much larger than other experimental and theoretical results shown in table 9.4, which hints towards a problem in the structure of the reference state for the first excited state as well.

In conclusion, the NAT-GNCSM finds a good description the ground-state resonance of ^{5}He compared to other theoretical and experimental results. For the first two excited-state resonances of ^{6}He, a comparison is challenging and the calculation should be improved in the future. However, the description of the ground state of ^{6}He is already very challenging in the standard NCSM. Thus, the description of the excited-state resonances might be even more challenging. Furthermore, we have to optimize the selection of reference states in order to obtain more robust results.

We have already noticed the factorial scaling of the model space dimensions with respect to the particle number A. In order to be able to calculate one or two additional steps in the N_{max} sequence it might be necessary to apply an importance truncation scheme as it is already done for the standard NCSM [Rot09].

10

INTERACTION ANALYSIS

The nuclear interaction plays a key role in the precise calculation of nuclear observables. We have already discussed the shift from phenomenological interactions towards realistic interactions derived from χEFT, so-called chiral interactions, in chapter 1. So far, we have used a chiral interaction derived by Entem, Machleidt, and Nosyk [EMN17] without discussing any details. This chapter provides a short introduction to the advantages and problems of interactions derived from χEFT.

There exist multiple sets of chiral interactions, which we call different families of interactions. We will use the NAT-GNCSM framework to probe those different interactions for resonance states, which has not been done before. We will analyze different characteristics of the family of chiral interactions derived from Entem, Machleidt, and Nosyk [EMN17] for the first excited 0^+ state of ^{4}He, which we already discussed in section 9.2. For a detailed description of χEFT beyond the short introduction in this chapter, we refer the following reviews [EHM09; ME11; HKK20].

General Aspects of Chiral Interactions The Lagrangian of χEFT consists of an infinite number of contributions [EHM09; ME11; HKK20]. Since it is not possible to derive all contributions of the interaction, it is necessary to find an ordering scheme that allows for a systematic setup and successive improvement of the interaction. The so called power counting orders the interaction terms, or interaction diagrams, by $\left(\frac{Q}{\Lambda_b}\right)^\nu$, with a soft scale $Q \sim$

m_π in the order of the pion mass and the chiral symmetry breaking or hard scale $\Lambda_b \sim 1\,\text{GeV}$, which defines the momentum at which the theory breaks down. The parameter v defines the order of the contributions, namely leading order (LO) for $v = 0$, next-to-leading order (NLO) for $v = 2$, next-to-next-to-leading order (N^2LO) for $v = 3$ and so on. At LO and NLO the interaction consists solely of nucleon-nucleon (NN) terms. Starting from N^2LO and N^3LO, three-nucleon (3N) and four-nucleon (4N) interactions appear, respectively. Furthermore, the number of diagrams increases for every chiral order. The power counting scheme of the chiral interactions is a key advantage of χEFT compared to phenomenological interactions because it allows to systematically improve the interaction and to estimate an interaction uncertainty of higher order contributions.

Regulator Scheme   During the calculation of the different interaction diagrams, we find that some of the diagrams include diverging integrals [EHM09; ME11; HKK20]. In order to regulate these divergences, it is necessary to define a regulator scheme, which consists of a regulator function and a cutoff value Λ. This is a first step in the derivation of a chiral interaction and there is a freedom in the choice of the regulator scheme and the cutoff value. We do not discuss the different regulator schemes in detail here, but mention some chiral interactions with different regulator schemes. The NN interaction from Entem, Machleidt, and Nosyk [EMN17] uses a non-local momentum-space regulator and is complemented by the 3N interaction by Hüther et al. [Hüt+20]. The NN+3N interaction by Ekström et al. [Eks+15], apply a non-local regulator scheme as well for their interaction. The NN+3N chiral interaction by Reinert et al. [RKE18; Mar+21] uses a semilocal momentum-space regulator scheme and the chiral interaction by Epelbaum et al. [Epe+19] uses a semilocal coordinate-space regulator scheme. This collection of different families of interactions already shows the diversity in possible families of interactions. All of the interactions use different regulator schemes and different regulator cutoff values. The goal of all sets of NN+3N interactions is a consistent treatment of all diagrams with the same regulator scheme and cutoff.

Low-Energy Constants   Besides the regulator schemes, there exists a second step which differs for the different families of interactions and regards the choice of the low-energy constants (LECs). The LECs are free parameters and characterize the strength of the interaction diagrams. In order to determine these LECs, we have to fit them to existing experimental data. This introduces the second source of differences in the final interaction. Not only the data, especially for the 3N contributions to the interaction, may differ, but also the fitting procedure can differ. The NN+3N interactions by Maris et al. [Mar+21] as well as Epelbaum et

al. [Epe+19] are to fitted NN data as well as to the ground-state binding energy and β-decay half-life of ^{3}H in the three-body sector. Whereas, the 3N interaction of Hüther et al. [Hüt+20] is fitted to the ground-state energies of ^{4}He and ^{16}O. A different fitting procedure is applied by Ekkström et al. [Eks+15]. First, they use a total of 13 experimental values for the binding energy or charge radius of light and medium-mass nuclei between ^{3}H and ^{25}O in addition to the NN data. Second, they do not fit the NN and 3N interactions separately, but perform an overall optimization of the full NN+3N interaction to the experimental data set.

Investigation with NAT-GNCSM   Now, we investigate the family of NN interactions derived by Entem, Machleidt, and Nosyk [EMN17] in detail. In previous calculations, we already used one of these interactions for a cutoff value of $\Lambda = 500\,\text{MeV}$ at N^{3}LO. We will vary both parameters separately and are particularly interested on the dependence of the imaginary part of the energy on the cutoff value as well as the order-by-order convergence behavior of the imaginary part of the energy. In case of the order-by-order convergence, the impact of higher orders in the interaction should become smaller following the motivation of the power counting scheme. The situation is a little different for the cutoff parameter. In an ideal χEFT, the final observables are cutoff independent. In practical applications, this does not hold for multiple technical reasons, which we do not discuss here and refer the reader to [ME11].

Figure 10.1 shows the order-by-order convergence for a set of reference states including the statistical uncertainties. Thus, we can analyze the impact of the order-by-order convergence on the final extrapolated eigenvalues and their statistical uncertainty. The uncertainties show two different behaviors. First, the uncertainty bands overlap throughout all orders for the real part of the second extrapolated eigenvalue and the imaginary part of the first extrapolated eigenvalue. Second, for the other extrapolated eigenvalues, the extrapolated eigenvalues shift downwards, for the real and imaginary part respectively, but the uncertainty bands still overlap for every successive order. A consequence of this characteristic is that we can exclude 3N contributions to the interaction in our calculation since they first appear at N^{2}LO and the inclusion of this order does not have a significant impact on the final results. However, if we are able to optimize the calculations and minimize the many-body uncertainties in the future, it might be necessary to include the 3N contributions.

Note, the uncertainties we discuss here are just the uncertainties from the many-body method, i.e., the NAT-GNCSM. The calculation of the interaction uncertainties is an additional step, but in our case the total uncertainty is dominated by the many-body uncertainty. In particular for the last two steps in the order-by-order convergence from N^{2}LO to N^{3}LO, the
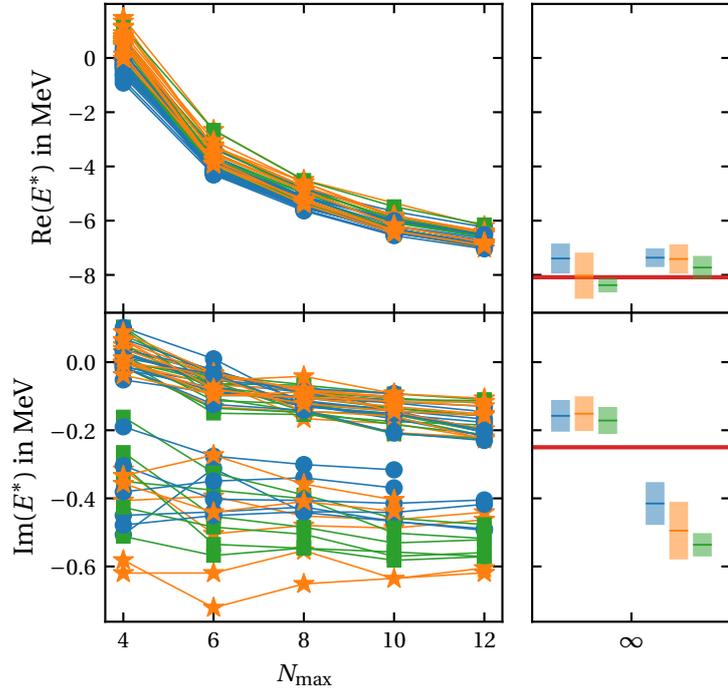
FIGURE 10.1.: Analysis of the dependence of the first excited-state energy of ^{4}He on different orders of the chiral interaction. The interactions correspond to the family of interaction by Entem, Machleidt, and Nosyk [EMN17] at NLO (●), N^{2}LO (★), and N^{3}LO (■) with $\Lambda = 500\,$MeV. In addition to the energy sequences, we show the extrapolated energy with an statistical uncertainty for a set of reference states and the experimental value (━) [TWH92]. The colors of the uncertainty bands correspond to the orders of the interaction.

statistical uncertainty bands mostly overlap or include each other.

Next, we are interested in the dependence of the energy sequences on the cutoff value Λ. A comparison of the extrapolated eigenvalues and their statistical uncertainties for a set of reference states is shown in figure 10.2. It shows that the statistical uncertainties overlap for the real and imaginary parts of the extrapolated eigenvalues for all three cutoff values. A surprising observation is that the many-body uncertainties are smaller for $\Lambda = 500\,$MeV, which might hint towards an effect of the cutoff value.

The analysis of the interaction on the energy eigenvalues, especially the imaginary part
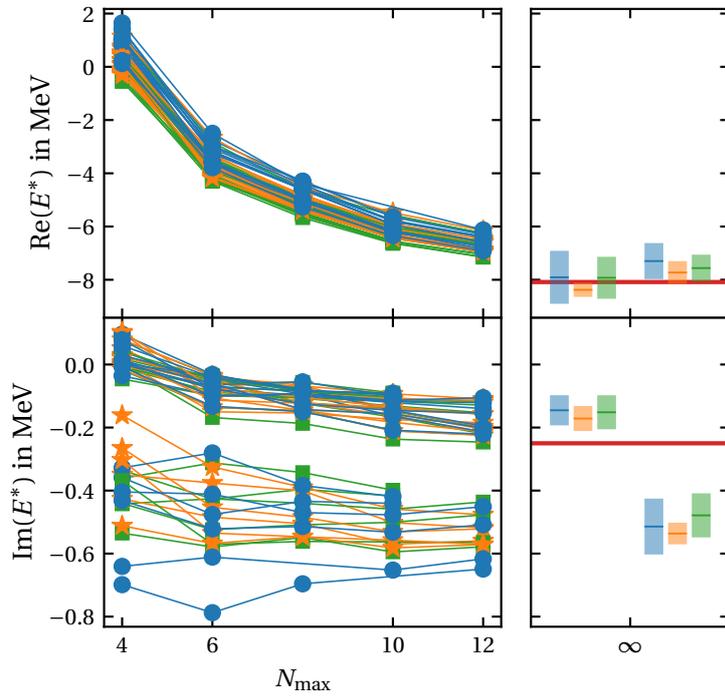
FIGURE 10.2.: Analysis of the dependence of the first excited-state energy of ^{4}He on different cutoff parameters of the chiral interaction. The interactions correspond to the family of interaction by Entem, Machleidt, and Nosyk [EMN17] with a cutoff of $\Lambda = 450\,\mathrm{MeV}(\bullet)$, $500\,\mathrm{MeV}(\star)$, and $550\,\mathrm{MeV}(\blacksquare)$ at N^{3}LO. In addition to the energy sequences, we show the extrapolated energy with an statistical uncertainty for a set of reference states and the experimental value (━━) [TWH92]. The colors of the uncertainty bands correspond to the different cutoff values of the interaction.

of the energy, in the NAT-GNCSM form a new perspective on the quality check of a family of interactions. However, in order to compute an independent interaction uncertainty it is necessary to further improve and optimize the many-body method such that the statistical many-body uncertainties become smaller.

11

THE TETRANEUTRON

The existence of a multi-neutron nucleus is a question that concerns theoretical and experimental physicists for more than 50 years [MC21]. To this day, there is no clear answer to the question whether a bound or resonant multi-neutron system exists. The evidence of such a multi-neutron system would affect many parts of nuclear physics, e.g., the nature of the nuclear forces, the setup of new experiments, the development of theories for such systems, and on the description of neutron stars [MC21]. Before we perform first calculations using the GNCSM framework for one specific multi-neutron system, the tetraneutron, we give a historical introduction to experiments and theoretical models that tried to investigate the existence of a bound or resonance state in the four-neutron system following the review by Marques et al. [MC21].

11.1. Experiment Approaches

All experimental approaches to detect a multi-neutron system face a general and, in a way, simple problem. Since neutrons have no charge, they do not interact with atomic electron clouds, but only with nuclei, which already reduces the detection efficiency of a single neutron significantly. The experiments can be classified into four types, which we mention briefly in the following. In the end, we discuss some of the most recent experimental endeavors in a little more detail.

The first experimental technique uses a double charge-exchange reaction of a pion with a ^{4}He target via the ^{4}He(π^-, π^+)^{4}n reaction. The measurement of the final π^+ allowed a conclusion on the ^{4}n using the missing mass method. The first experiments were performed by Gilly et al. in 1965 [Gil+65] and were followed by similar experiments by Ungar et al. in 1984 [Ung+84] and Gorringe et al. in 1989 [Gor+89]. The ^{208}Pb(π^-, π^+)^{4}n reaction was used by Chultem et al. in 1979 [Chu+79]. In all cases, it was not possible to observe a bound or resonance state for the tetraneutron, which might be a consequence of bad statistics since the reaction cross sections are very small [MC21].

The second experimental approach used a two-step process to prove the existence of the tetraneutron. The first experiment by Schiffer et al. in 1963 [SV63] radiated a nitrogen and aluminum sample with a secondary radioactive beam that was produced by the fission of a uranium beam. If a bound tetraneutron is produced during the fission the ^{14}N(^{4}n, n)^{17}N or ^{27}Al(^{4}n, ^{3}H)^{28}Mg reaction could occur and the subsequent β-decay of ^{17}N or ^{28}Mg would be observed. The approach was reapplied for different reactions by Detraz et al. in 1977 [Det77], Turkevich et al. in 1977 [Tur+77], de Boer et al. in 1980 [De +80], and most recently, by Novatsky et al. in 2012 [Nov+12; NSS14]. Again, all of these experiments were unable to prove the existence of a bound or resonance state in the tetraneutron despite some initial hopes of the evidence of a bound tetraneutron, which were withdrawn three years later due to a problem with the experimental setup [De +80; MC21].

The third experimental approach uses multi-nucleon transfer reactions with a stable primary beam and target. Similar to the double charge exchange reaction using a π^+, the missing mass method is used to characterize the final multi-neutron system. In 1974 Cerny et al. [Cer+74] used a ^{7}Li beam and target in order to produce the tetraneutron via the ^{7}Li(^{7}Li, ^{10}C)^{4}n reaction, but the poor separation from the trineutron channel via the ^{7}Li(^{7}Li, ^{11}C)^{3}n reaction did not allow to find a significant signal. Similar reaction processes were used by Belozyorov et al. in 1988 [Bel+88] that were able to overcome this problem. However, again no evidence of a bound or resonance state in the tetraneutron was found.

The GANIL Experiment The fourth experimental technique became accessible with radioactive secondary beams. Marques et al. [Mar+02] proposed an improvement of the multin-ucleon transfer reactions at the GANIL facility in 2002. The idea is that the tetraneutron is already formed as a sub-cluster in a radioactive secondary beam. They used a ^{14}Be secondary beam and a carbon target in order to investigate the 4n+^{10}Be breakup. In order to determine the mass of the tetraneutron they analyzed the recoil energy of after elastic

scattering of the neutral tetraneutron with a charged particle. The results showed a possible tetraneutron bound or low-energy resonance state with an energy of $E \leq 2\,\mathrm{MeV}$.

This first possible experimental evidence of a bound or resonance state also triggered many theoretical calculations, which we discuss in the next section.

The RIKEN Experiments   The availability of a radioactive secondary beam at the RIKEN facility was first exploited by Kisamori et al. in 2016 [Kis+16]. They used a double charge exchange $^8\mathrm{He}(^4\mathrm{He}, \, ^8\mathrm{Be})^4\mathrm{n}$ reaction to produce a tetraneutron. This reaction allowed the production af a multi-neutron system with vanishing momentum transfer, which should benefit the creation of a bound or resonance state of the tetraneutron. They also applied the missing mass method by measuring the two α particles from the in-flight breakup of $^8\mathrm{Be}$. In total, they were able to detect four events that would correspond to a tetraneutron with an energy of $E(^4\mathrm{n}) = 0.8(13)\,\mathrm{MeV}$ and an upper limit for the width of $\Gamma < 2.6\,\mathrm{MeV}$. Note, the large uncertainty, which mainly results from the missing mass method, also allows a bound tetraneutron.

A second experiment at the RIKEN facility, which searched for the tetraneutron, has been published very recently in 2022 by Duer et al. [Due+22]. They used a quasi-elastic knockout of an α-particle from the $^8\mathrm{He}$ secondary beam using a hydrogen target, i.e. a $^8\mathrm{He}(\mathrm{p}, \mathrm{p}^4\mathrm{He})^4\mathrm{n}$ reaction. They assumed that $^8\mathrm{He}$ consists of a well bound $^4\mathrm{He}$ core and four valence neutrons with a small center-of-mass motion, such that the knockout of the $^4\mathrm{He}$ core would leave a four-neutron system that could form a tetraneutron state. They also applied the missing mass method and found a possible resonant $^4\mathrm{n}$ state at

$$E_\mathrm{r} = 2.37 \pm 0.38(\text{stat.}) \pm 0.44(\text{sys.})\ \mathrm{MeV}, \tag{11.1}$$

$$\Gamma = 1.75 \pm 0.22(\text{stat.}) \pm 0.30(\text{sys.})\ \mathrm{MeV}. \tag{11.2}$$

Note, all experimental approaches measured all reaction constituents except for the four-neutron system. Afterwards, they drew a conclusion on the tetraneutron using the missing mass method or two-step processes. A future experiment at RIKEN is planned which intends to measure the neutrons as well. This would allow the use of the invariant mass method for the final calculation of the energy of the tetraneutron.

11.2. Theoretical Calculations

The development of theoretical models to describe the tetraneutron follows a similar history as the experimental approaches. Often, the possible experimental evidence of a bound or

resonance state of the tetraneutron prompted an increased interest on the theoretical side. However, similar to the experiments, there does not exist a final answer whether a bound or resonance state exists and, if it does, at which energies.

The theoretical calculations of the four-neutron system face a few main difficulties, which we mention here. First of all, it is necessary to find a method that is able to solve the eigenvalue problem in an *ab initio* manner. Nowadays, there exist multiple advanced methods for bound states, e.g., NCSM [Rot09; Var+09], coupled cluster [DH04], Green's function Monte-Carlo [CBN13], and in-medium SRG [Her17]. However, significantly less progress was made for the methods including the continuum, e.g., GNCSM [Li+21; Pap+13; Fos+17], and the Fadeev-Yakubovsky (FY) equations [LHL88; LC05; LC20].

Furthermore, the use of two-body scattering methods is impossible since there does not seem to exist a bound subsystem of the tetraneutron, i.e., a di- or tri-neutron. Hence, it would be necessary to calculate a full four-particle scattering process which is easy to derive, but very complicated to calculate [MC21].

A further problem for the precise calculation of a possible tetraneutron is the development of realistic nuclear interactions from χEFT, which made a lot of progress in the recent decade [EMN17; Epe+19; Mar+21; Hüt+20]. But, as we discussed in chapter 10, the interactions were never probed extensively for methods that include the continuum in the four-body system.

After the GANIL Experiment   Since all historical calculations up to the GANIL experiment involved some modeling of the method or the interaction, we start with the theoretical developments after the experiment at the GANIL facility in 2002 [Mar+02].

In 2003 Pieper [Pie03] applied the Green's function Monte Carlo approache to search for a bound tetraneutron using the NN Argonne V18 interaction [VP11] and the 3N Illinois IL2 interaction [Pie+01]. They found that the production of a bound tetraneutron would require huge changes in the nuclear interaction, which would have many consequences on the remaining nuclear chart. In order to search for a possible resonance, they added an attractive Woods-Saxon potential to their calculation, such that they could produce an artificial bound state. Afterwards, they extrapolated the energy towards a vanishing Woods-Saxon potential strength and predicted a tetraneutron state at an energy of $E \sim 2\,\mathrm{MeV}$. Since the Green's function Mont Carlo approach can only calculate bound-states, it is not possible to deduce an imaginary part for this state.

A similar technique was used by Lazauskas et al. in 2005 [LC05], who used the analytic continuation in the coupling constant (ACCC) [V I89; TSV97] in order to continue FY calculations

into the continuum. With this approach they did not find a bound or resonance state in the tetraneutron.

After the First RIKEN Experiment After the first possible detection of a low-energy resonance at RIKEN in 2016 [Kis+16], the interest of theoretical physicists increased once more. In 2016, Hiyama et al. [Hiy+16] used the FY equation in configuration space [LC05] as well as the variational Gaussian expansion method [Kam88; HK12] in combination with the complex scaling and the ACCC method in order to describe a possible tetraneutron resonance. Again, no evidence for a bound or resonance state of the tetraneutron was found, such that they concluded that the results by Pieper in 2003 [Pie03] must be induced by some residual extrapolation artifacts induced by the Woods-Saxon potential.

In contrast, Shirokov et al. in 2016 [Shi+16a] used the single-state harmonic oscillator representation of scattering equations (SS-HORSE) to compute a ground state of the tetraneutron. The SS-HORSE is an extension of the NCSM, which extends the Hamilton matrix with an infinite kinetic energy matrix in the HO basis [MC21]. Hence, the interaction matrix elements are set to zero for a Slater determinants with $N > N_{\max}$. The eigenvectors of this infinite Hamilton matrix can be calculated if the eigenvalue problem in the $N_{\max}$ space can be calculated, which is a standard NCSM calculation [Shi+16b; Maz+17]. With the eigenvectors of the infinite Hamilton matrix it is possible to derive scattering observables at positive energy, e.g., the scattering phase shift. From this phase shifts they determined a resonance energy of

$$E_{\mathrm{r}} = 0.8 \, \mathrm{MeV}, \tag{11.3}$$

$$\Gamma = 1.4 \, \mathrm{MeV} \tag{11.4}$$

using the JISP16 NN potential [Shi+16a]. This results is in accordance with the results obtained by the first experiment at RIKEN [Kis+16] as well as the results of Pieper [Pie03].

At this point, we mention that all methods except the SS-HORSE method were based on bound-state calculations and used extrapolation techniques in order to obtain results in the continuum. Hence, they assume a continuous transition from bound system towards continuum systems, which might be a strong assumption. In case of the SS-HORSE method, the approximation of the continuum is a consequence of the single-state approximation. One thing all of these calculations concluded was that there does not exist a bound tetraneutron. However regarding the possible existence of a resonance in the tetraneutron the results were inconclusive.

The first methods that were able to perform direct calculations in the continuum and

were applied to the tetraneutron, use some version of a GNCSM ansatz. In 2017, Fossez et al. [Fos+17] used a similar GNCSM framework to search for a tetraneutron resonance. However, for a robust calculation with the NAT-GNCSM in the continuum, they had to scale the interaction and extrapolate towards the correct interaction. In contrast to Pieper [Pie03], they were still able to perform some NAT-GNCSM calculations in the continuum before the calculations became unstable. Furthermore, they were able to perform a robust calculation for the tetraneutron and the unscaled interaction with the GNCSM, but only for $S_{\max} = 2$. The resonance energy for this calculation is

$$E_{\mathrm{r}} \approx 7\,\mathrm{MeV}, \tag{11.5}$$

$$\Gamma \approx 4\,\mathrm{MeV}, \tag{11.6}$$

which seemed to be an upper bound for their other calculations [Fos+17].

In 2019, Li et al. [Li+19] also used a similar GNCSM framework with a NAT-GNCSM calculation for the tetraneutron. In contrast to Fossez et al. [Fos+17], they used an external Woods-Saxon potential instead of a scaled NN potential in order to stabilize their calculations. Their most optimal calculation yields an energy of

$$E_{\mathrm{r}} \approx 2.64\,\mathrm{MeV}, \tag{11.7}$$

$$\Gamma \approx 2.38\,\mathrm{MeV}. \tag{11.8}$$

In conclusion, there already exist a few theoretical calculations for the tetraneutron. They all agree regarding a non-existence of a bound state in the tetraneutron. Regarding the existence of a resonance in the tetraneutron, the results are ambiguous. The methods using the few-body FY equations in combination with the ACCC method do not predict a resonance in the tetraneutron, whereas many-body methods, especially the GNCSM frameworks, predict a low-energy resonance in the tetraneutron, which is in rough agreement with the current experimental results. However, there is still a lot of work to do until a complete *ab initio* description of the tetraneutron will yield conclusive results.

11.3. First Calculations with our NAT-GNCSM

We have already pointed out many of the theoretical problems regarding the description of a tetraneutron. Other GNCSM frameworks already tried to investigate the tetraneutron and faced severe problems regarding the stability of the results without altering the nuclear

potential number	V_{WS} in MeV	V_{LS} in MeV	a_{WS} in fm	R_{WS} in fm	$E_{\text{b}}\left(s_{1/2}^{\text{n}}\right)$ in MeV	$E_{\text{r}}\left(p_{3/2}^{\text{n}}\right)$ in MeV	$E_{\text{r}}\left(p_{1/2}^{\text{n}}\right)$ in MeV
I	-20	-25	0.67	2.02	-3.35	$0.98 - 0.84i$	$0.27 - 4.17i$
II	-25	-30	0.67	2.02	-5.64	$0.47 - 0.22i$	$0.87 - 3.32i$
III	-15	-10	0.67	2.5	-3.11	$0.93 - 0.94i$	$1.09 - 2.04i$

TABLE 11.1.: List of three different one-body potentials with different potential parameters for the calculation of a Gamow basis of ^{4}n. It includes the energies of the bound and resonance state in the $s_{1/2}^{\text{n}}$, $p_{3/2}^{\text{n}}$, and $p_{1/2}^{\text{n}}$ partial wave, respectively.

potential or adding an external potential. Hence, we take a step back and start our analysis of the tetraneutron at the beginning of the GNCSM framework. In chapter 9, we have used physically motivated partial-wave selections as well as one-body potentials. Since the tetraneutron is a very exotic system, it is unclear if any assumptions, e.g., the shell structure, are still correct for this system.

Therefore, we have to start the investigation of tetraneutron with an analysis of the partial-wave selection. We expect the tetraneutron to have many contributions from the continuum, and thus, only use partial-wave selections with at least two partial waves. For the first calculations, we use potential I of table 11.1, which was already used successfully in chapter 9. In case of the $s_{1/2}^{\text{n}} p_{1/2}^{\text{n}}$ partial-wave selection, the sign of V_{LS} is switched such that the $p_{1/2}$ wave is energetically lower than the $p_{3/2}$ partial wave. The variation of the one-body potential will be done in a next step.

In figure 11.1, we show the lowest-lying eigenvalue of the tetraneutron for different partial-wave selections. The energy eigenvalues of the $s_{1/2}^{\text{n}} p_{1/2}^{\text{n}}$ partial-wave selection have a rather stable convergence behavior for the energy of the larger two HO frequencies, but the imaginary part is very small or vanishes. Since the real part of the energy is still positive, we can eliminate the possibility of a bound state. Hence, this partial-wave selection might not include enough information about the continuum in the reference state.

In case of the $p_{3/2}^{\text{n}} p_{1/2}^{\text{n}}$ partial-wave selection, the convergence behavior of the real part of the energy is still stable and the imaginary part of the energy deviates from zero, which hints towards an important contribution of the $p_{3/2}$ continuum. Especially, the calculation for a HO frequency of $4\,\text{MeV}$ seems to produce a resonance state with a stable convergence behavior
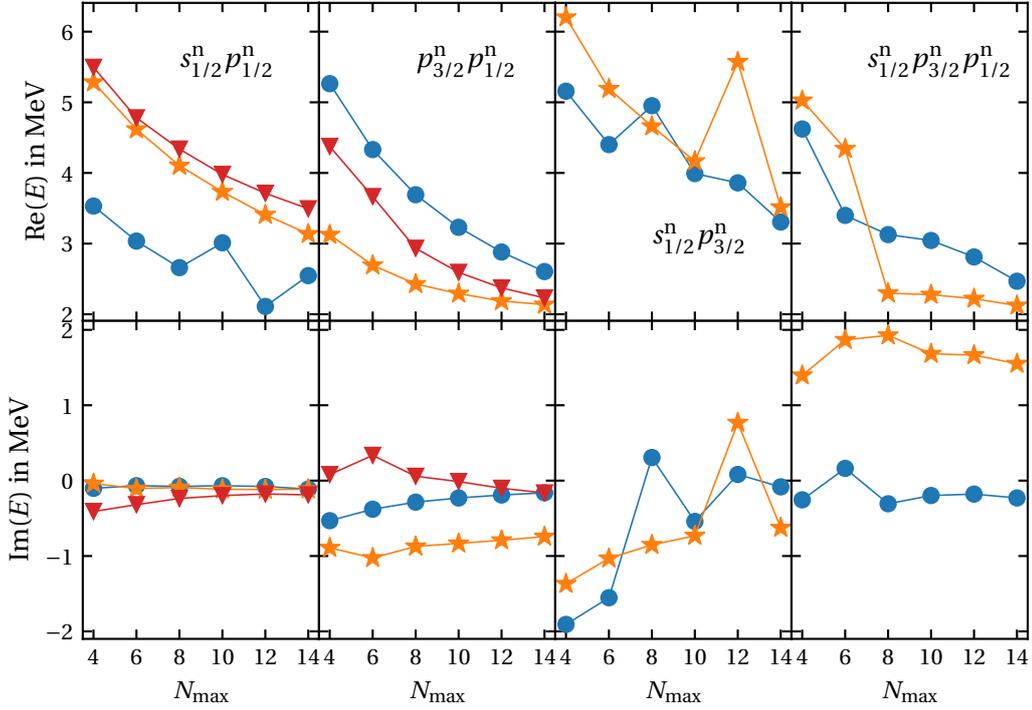
FIGURE 11.1.: Calculations the energies of the first (━) and second (╍) eigenstate of
^{4}n for the HO frequencies 2 MeV (●), 4 MeV (★), 6 MeV (▼). The columns
apply different partial-wave selections in the reference state for the one-
body potential I. For the truncations of the reference state see table 11.2.

of the energy as well as a clear differentiation from the second state in the expectation value
of the center-of-mass Hamiltonian.

The next two partial-wave selections, i.e., $s_{1/2}^n p_{3/2}^n$ and $s_{1/2}^n p_{3/2}^n p_{1/2}^n$, show strong insta-
bilities. This is also reflected in the exclusion of calculations for th HO frequency 6 MeV
because we were unable to obtain a robust energy sequence in that case. For the $s_{1/2}^n p_{3/2}^n$
partial-wave selection, the real part of the energy contains at least one problematic step
in the $N_{\max}$ sequence, for which the ground-state exhibits a comparably large expectation
value of the center-of-mass Hamiltonian. The irregularity of the real part of the energy is also
visible for the imaginary part of the energy. However, similar to the $p_{3/2}^n p_{1/2}^n$ partial-wave
selection, the energies could describe a possible resonance even though this has to be treated
with particular caution as the overall calculations are very unstable. For the $s_{1/2}^n p_{3/2}^n p_{1/2}^n$

Partial-wave selection	$N_{\mathrm{max}}^{\mathrm{HO}}$	S_{max}	ν_{s}
$s_{1/2}^{\mathrm{n}} p_{1/2}^{\mathrm{n}}$	4	2	18
$p_{3/2}^{\mathrm{n}} p_{1/2}^{\mathrm{n}}$	3	2	18
$s_{1/2}^{\mathrm{n}} p_{3/2}^{\mathrm{n}}$	3	2	15
$s_{1/2}^{\mathrm{n}} p_{3/2}^{\mathrm{n}} p_{1/2}^{\mathrm{n}}$	3	2	18

TABLE 11.2.: Reference state truncations for different partial-wave selection depicted in figure 11.1.

partial-wave selection, the energy convergence is slightly more stable and the imaginary parts of the energy become positive for the HO frequency 4 MeV.

Note, we had to apply different reference state truncations for all partial-wave selections, which are shown in table 11.2. This was necessary to obtain stable results in the NAT-GNCSM calculation. It is already a first indication of the challenge to find suitable reference states for the tetraneutron.

We will continue our investigations using the $p_{3/2}^{\mathrm{n}} p_{1/2}^{\mathrm{n}}$ partial-wave selection and move on towards a variation of the three one-body potentials characterized in table 11.1. The first two one-body potentials were already used successfully for different nuclei in chapter 9. The third potential is proposed in order to optimize the Gamow basis for the large extension of the many-body wave function of the tetraneutron.

In figure 11.2, we show the energy convergence for the three different one-body potentials. For all potentials, there exist energy sequences which could correspond to resonance states, but for potential II the calculations are less stable. Thus, the calculations for the larger two HO frequencies 5 MeV and 6 MeV have to be excluded. The energy convergences for potential III are similar to the energy sequence of potential I, but all calculations show a resonance with a significant width. In case of potential I, most of the calculation correspond to either a bound state or a very narrow resonance.

Finally, after we investigated the underlying structure of the Gamow basis using different partial-wave selections and one-body potentials, we can start to analyze the truncations of the reference state. This allows us to investigate the stability of the energy sequences for a set of reference states and possibly a first extrapolation of a ground-state energy of the tetraneutron.
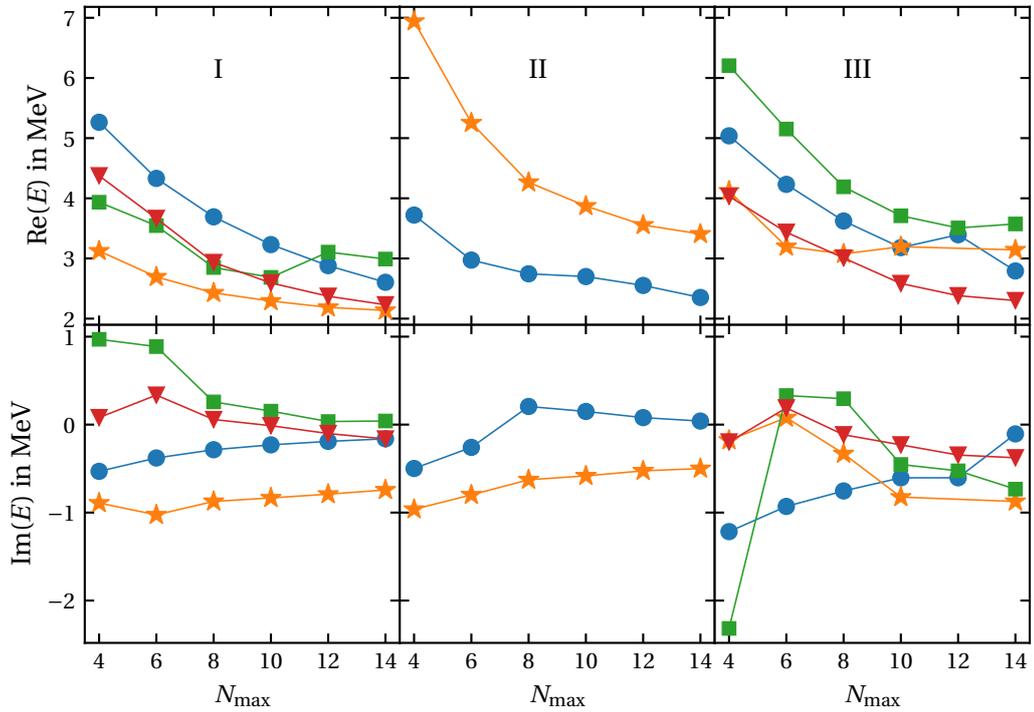
FIGURE 11.2.: Comparison of the ground-state energy of ^{4}n for different one-body potentials from table 11.1 in the Gamow basis and HO frequencies 2 MeV (●), 4 MeV (★), 5 MeV (■), 6 MeV (▼). The Gamow basis of the reference state uses the $p_{3/2}^n p_{1/2}^n$ partial-wave selection. The other truncations are shown in table 11.2.

Figure 11.3 shows the variation of the $N_{\mathrm{max}}^{\mathrm{HO}}$ truncation of the reference state for potential III of table 11.1. The energy sequences for both parts of the energy are comparably stable with respect to a variation of the $N_{\mathrm{max}}^{\mathrm{HO}}$ truncation even for the smallest $N_{\mathrm{max}}^{\mathrm{HO}} = 2$ truncation, which often showed too little admixture of the continuum in chapter 9. Nevertheless, the calculations still show some irregularities in the convergence, which is a consequence of two eigenstates with similar expectation value of the center-of-mass Hamiltonian.

Even though there exist some unstable energy sequences for the ground-state energies of the tetraneutron, we attempt to determine a mean and statistical uncertainty for the ground-state energy. Since some convergence curves do not follow a steady monotonous decrease, we extend our procedure to determine an extrapolated eigenvalue from section 8.6.
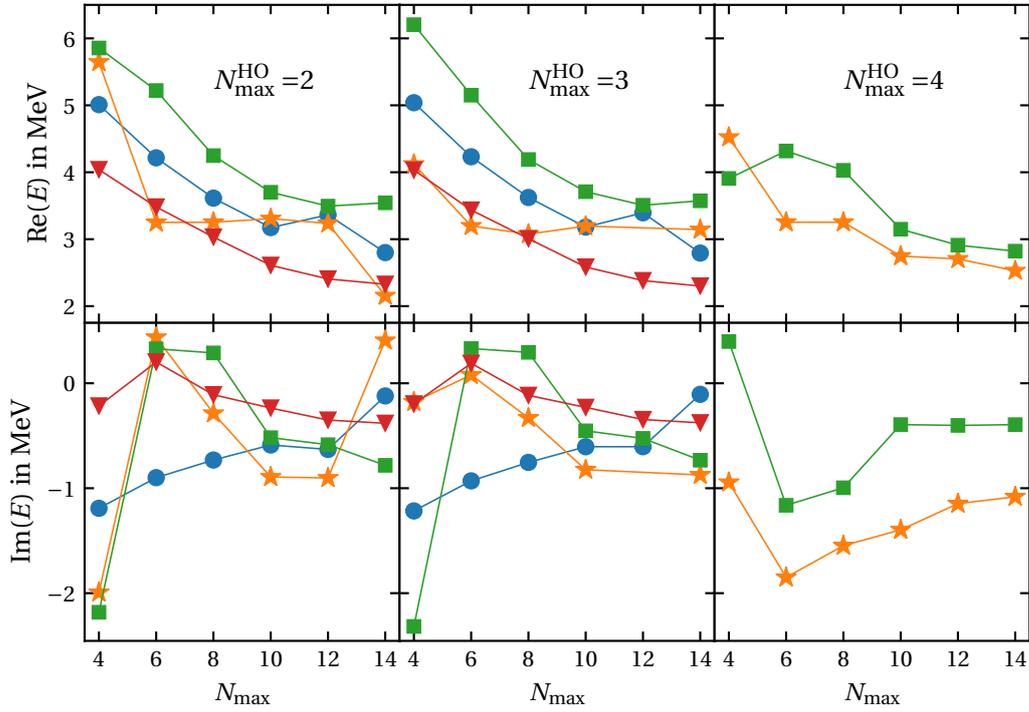
FIGURE 11.3.: Comparison of the ground-state energy of ^{4}n for different N_{max}^{HO} truncations of the reference state and HO frequencies 2 MeV (●), 4 MeV (★), 5 MeV (■), 6 MeV (▼). The Gamow basis uses potential III from table 11.1 and the $p_{3/2}^n p_{1/2}^n$ partial-wave selection. The remaining truncations of the reference state are $\nu_s = 18$ and $S_{max} = 2$.

If an exponential fit is impossible or not appropriate because the real part of the energy has a constant, linear, or slightly alternating convergence pattern, we just use the value of the largest accessible N_{max} of the respective N_{max} sequence. This corresponds to the procedure we use to determine the extrapolated eigenvalue for the imaginary part of the energy.

The energy sequences and the corresponding mean and statistical uncertainty of the extrapolated eigenvalues are shown in figure 11.4 for a set of suitable reference states. The extrapolated eigenvalues yield a resonance energy and the resonance width of

$$E = 3.0(9)\,\text{MeV}, \tag{11.9}$$

$$\Gamma = 2.4(16)\,\text{MeV}, \tag{11.10}$$
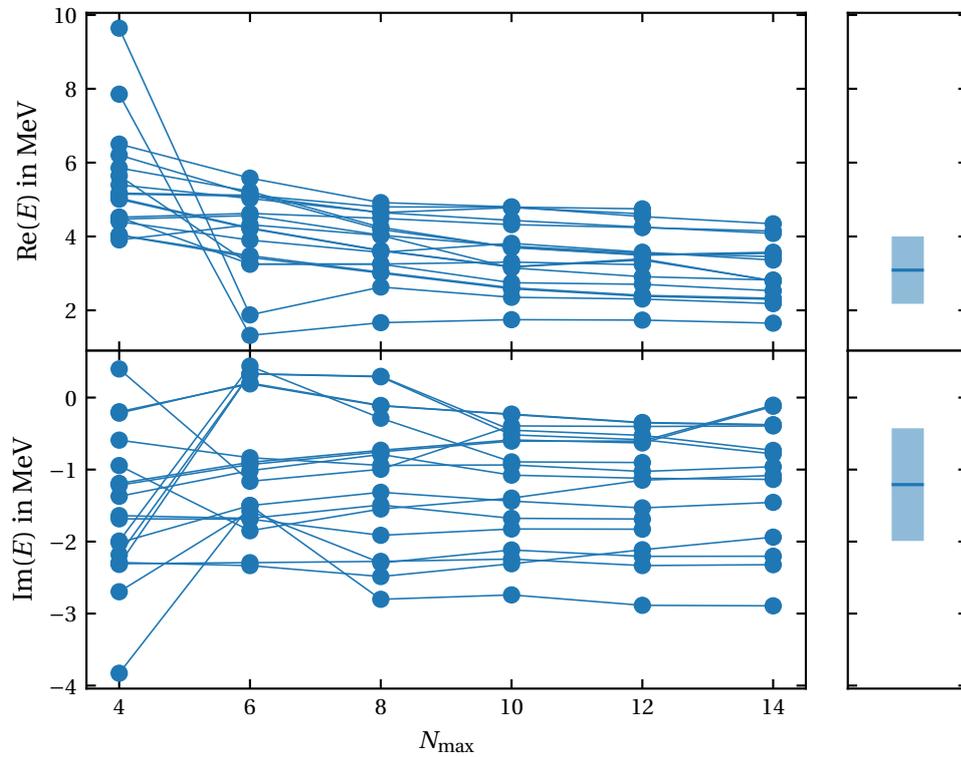
FIGURE 11.4.: Calculation of a mean and statistical uncertainty for the ground-state energy of the ^{4}n for a set of reference states.

which would be in overall agreement with the recent experimental results [Mar+02; Kis+16; Due+22] and other theoretical calculations using the GNCSM framework [Fos+17; Li+19]. However, further work is crucial in order to stabilize the calculations, especially with respect to the partial-wave selection and the underlying one-body potential. The $s_{1/2}^n p_{3/2}^n p_{1/2}^n$ partial-wave selections seems to be an interesting extension of the $p_{3/2}^n p_{1/2}^n$ partial-wave selection if we are able to stabilize the calculations. Regarding the one-body potentials, an extensive survey of one-body potentials for the Gamow basis of the reference states could help to optimize the subsequent NAT-GNCSM calculations. We have already seen that potential II, which is the deepest potenital we used, generates unstable results. Thus, an extension towards weaker potentials with larger potentials widths could be a promising task. Furthermore, we could apply an external potential [Li+19] or scale the NN interaction [Fos+17] in order to artificially bind the tetraneutron and stabilize the calculation in this regime.

Conclusion

In this work, we have developed a complete GNCSM framework for the calculation of nuclear resonances. The GNCSM framework is constructed in four main steps, which are depicted on the left-hand side of figure 11.1. During the development of the GNCSM framework and its application to different nuclei, we were able to establish guidelines for the different steps of the GNCSM framework. For future applications, this guidelines form a starting point for the calculation of nuclear resonances in light nuclei. However, the application to very exotic nuclear systems like the tetraneutron can become a lot more challenging.

As a first step, we set up a Gamow single-particle basis, which contains a Berggren basis for a set of partial waves. The Berggren basis contains single-particle resonance and scattering states, which include information about the continuum. In combination with the HO basis in the remaining partial waves they form the aforementioned Gamow basis. In the applications to light systems, the use of the $s_{1/2}$ and $p_{3/2}$ partial waves, i.e., the lowest two shell model-orbitals, has proven to provide the most important contributions of the continuum.

In the second step, the two-body matrix elements of the asymptotically free resonance and scattering states of the Berggren basis were expanded in HO wave functions. The finite range of the HO wave functions regulates the expansion. Since we are limited to a finite number of HO wave functions, we have defined a range of HO frequencies, for which the calculation of the matrix elements converges. The matrix elements form the relevant input for the GNCSM calculation.

In the third step, we perform a first GNCSM calculation. The use of the Gamow single-particle basis has two consequences on the GNCSM calculation. First, the Hamilton matrix, and consequently the matrix eigenvalue problem, becomes complex symmetric. Second, we
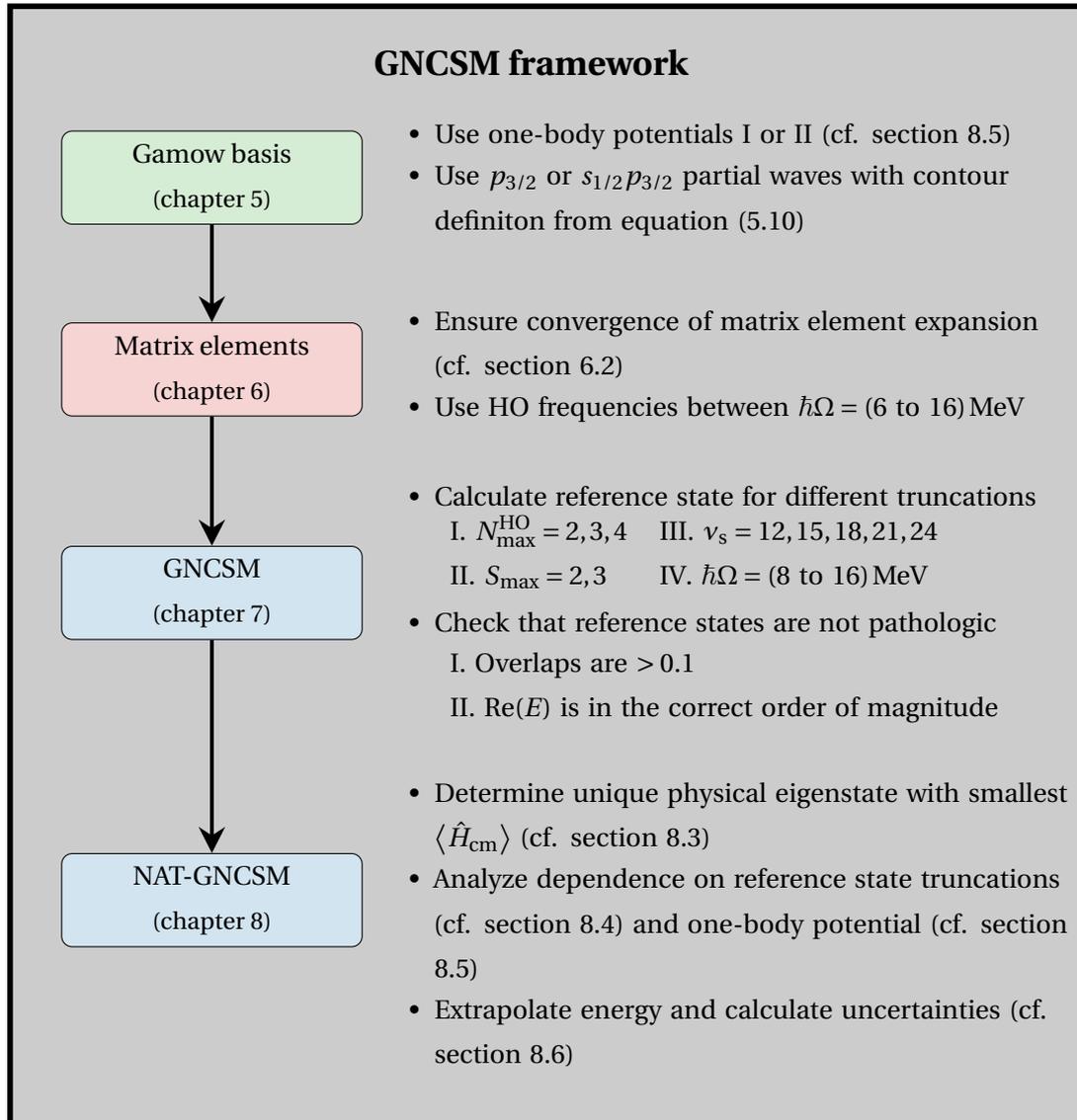
FIGURE 11.1.: Guidelines for the application of the GNCSM framework.

introduce an additional many-body truncation for the partial waves that use the Berggren partial waves. Regarding the choice of the Gamow basis for the GNCSM calculations, it would be desirable to use the Berggren basis for as many partial waves as possible in order to maximize the information about the continuum. In practical applications, the correct selection of partial waves in the Berggren basis is one of the most crucial points of the entire calculation. The selection of the partial waves affects the GNCSM calculation in three

ways. First, if we increase the number of partial waves in the Berggren basis, the GNCSM calculations become less stable and it becomes more challenging to determine suitable resonance states in the GNCSM as the discretized many-body scattering states dominate the calculated spectrum. Second, we use an orthogonal eigenvalue solver, but the Gamow basis is non-orthogonal in the Berggren partial waves. Hence, the solution becomes worse the more Berggren partial waves we include. Third, the single-particle model space of Berggren partial waves is much larger compared to the HO basis which translates to a much larger many-body model space.

In the final step, we use the first GNCSM calculations to obtain a set of reference states, which we use for the calculations of a set of Gamow natural orbitals. The goal of the Gamow natural orbitals is to enhance the convergence rate of the energy eigenvalues and to circumvent the approximation of an orthogonal eigenvalue solver. Due to the approximations and the increased instability of the GNCSM calculation for larger model spaces, it is difficult to determine an optimal reference state for the subsequent NAT-GNCSM calculation. Thus, we perform a NAT-GNCSM calculation for a set of natural-orbitals and use a statistical approach to determine an extrapolated eigenvalue and a many-body uncertainty for the NAT-GNCSM calculations, which takes the results for every suitable reference state into account.

In the first applications of the GNCSM framework, we present ground and excited-state resonances in light nuclei. For the ground-state resonances of ^{4}H, ^{4}Li, and ^{5}He, we compared our results with existing GNCSM calculations [Li+21; Pap+13]. Additionally, we were able to quantify the many-body uncertainties in our calculations. The description of the 2^- ground-states of the ^{4}H and ^{4}Li mirror nuclei is of particular interest since the experimental results are inconclusive up to this point. Even though, the selection of a suitable set of reference states has been challenging, we found an overall agreement for both states with the other GNCSM calculation. The theoretical uncertainties are smaller than the variations of different experimental measurements.

For the ground-state energy of ^{5}He, we were able to compute a very stable result for the real and imaginary part of the energy. This probably is a consequence of the rather simple structure of the ground-state of ^{5}He consisting of a strongly bound ^{4}He core and a loosely bound neutron in the p-shell. The computed ground-state energy agrees with both, another GNCSM calculation and the experimental results, very well.

The calculation of excited-state resonances of ^{4}He and ^{6}He demonstrated two challenges of the current GNCSM framework. The determination of suitable reference states in the GNCSM calculation for ^{4}He is very difficult, such that we had to fall back on the ground state of ^{4}He,

which shows resonance characteristics in the small model spaces of the GNCSM. However, it will become a bound state in large model spaces, and thus, might contain not enough admixtures of the continuum in order to describe the excited-state resonances. It might be necessary to improve the GNCSM calculations for highly excited states in order to obtain stable and suitable reference states for the subsequent NAT-GNCSM calculation.

For the first excited states of ^{6}He, we are able to use a suitable reference state. The comparison to other theoretical calculations and experimental measurements were rather problematic. The real parts of the energies coincide with some other results, whereas the imaginary parts of the energies coincide with other results, such that the correct description of the first excited states of ^{6}He is of strong interest in the future. The most challenging part of the theoretical calculations is the many-body model space dimension, which scale factorially with the particle number, in the GNCSM as well as the NAT-GNCSM, such that we are limited to rather small many-body truncations. A solution might be the introduction of an importance truncation scheme [Rot09], which decreases the model space dimension using an *a priori* estimate on the importance of every Slater determinant.

Besides the calculation of resonance states for different nuclei, we analyzed the dependence of the resonance energy for a family of interactions with different momentum cutoffs and chiral orders from Entem, Machleidt, and Nosyk [EMN17]. For the cutoff variation at N^{3}LO, we found that the uncertainty induced by the many-body method exceeds the deviations for different cutoffs. The order-by-order analysis of the interaction showed a small change in the step from NLO to N^{2}LO, but no significant change for the subsequent order N^{3}LO. However, the uncertainties are still dominated by the many-body uncertainty. The order-by-order behavior also justified that we neglected contributions of 3N forces to the interaction since we obtain very good results for NLO already, which only consists of NN forces.

Finally, we applied the GNCSM framework to the description of the tetraneutron, which is of special interest after the most recent experimental efforts by Duer et al. [Due+22]. Since the tetraneutron is an extreme nuclear system, we had to optimize the basis parameters of the Gamow single-particle basis. We assumed that a possible ground-state resonance of the tetraneutron has a very extended wave function. Thus, we used a weak and broad one-body potential. This allowed us to obtain suitable reference states, which contain enough admixtures of the continuum. In the subsequent NAT-GNCSM calculation, we were able to compute the resonance energy for a possible tetraneutron resonance if we use the p-wave continuum. The calculations have shown that the determination of suitable and stable reference states is very important for such an extreme system.

A possible way to stabilize the overall calculation is used by other applications of the GNCSM [Fos+17; Li+19], which scale the nuclear potential or add an external Woods-Saxon potential to confine the neutron system and increase the binding energy. In future endeavors, this ansatz could be used to include the s-wave continuum into the calculation, which might improve the description of the ground-state.

We have already mentioned some extensions and optimizations of the GNCSM framework for future applications. A very important extension of the GNCSM towards heavier nuclei is the development of an importance truncations scheme, which is already applied in the standard NCSM very successfully [Rot09]. It optimizes the many-body model space *a priori*, such that the final diagonalization is performed in a smaller subspace. A second extension targets the correct treatment of non-orthogonal basis sets. At the moment, we use an orthogonal eigenvalue solver for the diagonalization in the GNCSM, but the Gamow single-particle basis is non-orthogonal. The necessary changes are the correct calculation of the matrix elements of the Hamilton matrix and the use of a non-orthogonal eigenvalue solver.

During the applications of the GNCSM framework, we found the determination of a suitable set of reference state is one of the most crucial steps. This is necessary to determine a many-body uncertainty of the calculation. Something we have not targeted too much during this thesis, is the choice of the one-body potential of the Gamow basis. We have already seen that the stability of the reference states and the result are dependent on the choice of the one-body potential. Hence, an extended survey of one-body potentials can help to stabilize the reference state calculation, and consequently, improve the results.

11

BIBLIOGRAPHY

[Ajz91]   F. Ajzenberg-Selove. "Energy levels of light nuclei A = 13–15". In: *Nuclear Physics A* 523.1 (1991), 1–196. DOI: https://doi.org/10.1016/0375-9474(91)90446-D.

[And+99]   E. Anderson, Z. Bai, C. Bischof, et al. *LAPACK Users' Guide*. Third. Society for Industrial and Applied Mathematics, 1999. DOI: 10.1137/1.9780898719604.

[BNQ13a]   S. Baroni, P. Navrátil, and S. Quaglioni. "Ab Initio Description of the Exotic Unbound 7He Nucleus". In: *Phys. Rev. Lett.* 110.2 (2013), 22505. DOI: 10.1103/PhysRevLett.110.022505.

[BNQ13b]   S. Baroni, P. Navrátil, and S. Quaglioni. "Unified ab initio approach to bound and unbound states: No-core shell model with continuum and its application to He-7." In: *Phys. Rev. C* 87.3 (2013), 34326. DOI: 10.1103/PhysRevC.87.034326.

[BNV13]   B. R. Barrett, P. Navratil, and J. P. Vary. "Ab initio no core shell model". In: *Progress in Particle and Nuclear Physics* 69.1 (2013), 131–181. DOI: 10.1016/j.ppnp.2012.10.003.

[BD83]   D. Baye and P. Descouvemont. "Electromagnetic transitions and radiative capture in the generator-coordinate method". In: *Nuclear Physics A* 407.1 (1983), 77–97. DOI: https://doi.org/10.1016/0375-9474(83)90309-3.

[Bel+88] A. V. Belozyorov, C. Borcea, Z. Dlouhý, et al. "Search for the tri- and tetra-neutron in reactions induced by 11B and 9Be ions on 7Li". In: *Nuclear Physics A* 477.1 (1988), 131–142. DOI: https://doi.org/10.1016/0375-9474(88)90365-X.

[Ber68] T. Berggren. "On the use of resonant states in eigenfunction expansions of scattering and reaction amplitudes". In: *Nuclear Physics A* 109.2 (1968), 265–287. DOI: https://doi.org/10.1016/0375-9474(68)90593-9.

[Bla+91] S. Blagus, D. Miljanić, M. Zadro, et al. "4H nucleus and the 2H(t,tp)n reaction". In: *Physical Review C* 44.1 (1991), 325–328. DOI: 10.1103/PhysRevC.44.325.

[BFP07] S. K. Bogner, R. J. Furnstahl, and R. J. Perry. "Similarity renormalization group for nucleon-nucleon interactions". In: *Physical Review C - Nuclear Physics* 75.6 (2007). DOI: 10.1103/PhysRevC.75.061001.

[BF77] J. E. Bond and F. W. K. Firk. "Determination of R-function and physical-state parameters for n-4He elastic scattering below 21 MeV". In: *Nuclear Physics A* 287.2 (1977), 317–343. DOI: https://doi.org/10.1016/0375-9474(77)90499-7.

[Bri+90] B. Brinkmöller, H. P. Morsch, P. Decowski, et al. "Structure of 4Li and 4Ge observed in the 1H(alpha,3He p)n reaction". In: *Phys. Rev. C* 42.2 (1990), 550–562. DOI: 10.1103/PhysRevC.42.550.

[Bru+90] M. Bruno, F. Cannata, M. D'Agostino, et al. "4Li g.s. formation in the 3He+p+n reaction". In: *Phys. Rev. C* 42.1 (1990), 448–450. DOI: 10.1103/PhysRevC.42.448.

[BV21] A. Burrows and D. Vartanyan. "Core-collapse supernova explosion theory". In: *Nature* 589.7840 (2021), 29–39. DOI: 10.1038/s41586-020-03059-w.

[Cer+74] J. Cerny, R. B. Weisenmiller, N. A. Jelley, et al. "7Li + 7Li reaction studies leading to multi-neutron final states". In: *Physics Letters B* 53.3 (1974), 247–249. DOI: https://doi.org/10.1016/0370-2693(74)90471-7.

[Chu+79] D. Chultem, V. S. Evseev, V. M. Sidorov, et al. "Search for 4n in pi- double charge exchange reactions with heavy nuclei". In: *Nuclear Physics A* 316.3 (1979), 290–294. DOI: https://doi.org/10.1016/0375-9474(79)90038-1.

[CBN13]   A. Cipollone, C. Barbieri, and P. Navratil. "Isotopic chains around oxygen from evolved chiral two- and three-nucleon interactions". In: *Physical Review Letters* 111.6 (2013), 062501. DOI: 10.1103/PhysRevLett.111.062501.

[Con17]   C. Constantinou. "Natural orbitals for the no-core configuration interaction approach". PhD thesis. University of Notre Dame, 2017. DOI: 10.48550/ARXIV.1704.02363.

[Con+17]   C. Constantinou, M. A. Caprio, J. P. Vary, et al. "Natural orbital description of the halo nucleus 6He". In: *Nuclear Science and Techniques* 28.12 (2017), 179. DOI: 10.1007/s41365-017-0332-6.

[De +80]   F. W. N. De Boer, J. J. Van Ruyven, A. W. B. Kalshoven, et al. "The tetraneutron revisited". In: *Nuclear Physics A* 350.1 (1980), 149–156. DOI: https://doi.org/10.1016/0375-9474(80)90393-0.

[DH04]   D. J. Dean and M. Hjorth-Jensen. "Coupled-cluster approach to nuclear physics". In: *Physical Review C - Nuclear Physics* 69.5 (2004), 054320–1. DOI: 10.1103/PhysRevC.69.054320.

[DB10]   P. Descouvemont and D. Baye. "The R-matrix theory". In: *Reports on Progress in Physics* 73.3 (2010), 36301. DOI: 10.1088/0034-4885/73/3/036301.

[Det77]   C. Detraz. "Possible existence of bound neutral nuclei". In: *Physics Letters B* 66.4 (1977), 333–336. DOI: https://doi.org/10.1016/0370-2693(77)90008-9.

[Due+22]   M. Duer, T. Aumann, R. Gernhäuser, et al. "Observation of a correlated free four-neutron system". In: *Nature* 606.7915 (2022), 678–682. DOI: 10.1038/s41586-022-04827-6.

[Eks+15]   A. Ekström, G. R. Jansen, K. A. Wendt, et al. "Accurate nuclear radii and binding energies from a chiral interaction". In: *Phys. Rev. C* 91.5 (2015), 51301. DOI: 10.1103/PhysRevC.91.051301.

[EM03]   D. R. Entem and R. Machleidt. "Accurate charge-dependent nucleon-nucleon potential at fourth order of chiral perturbation theory". In: *Physical Review C* 68.4 (2003), 41001. DOI: 10.1103/PhysRevC.68.041001.

[EMN17]   D. R. Entem, R. Machleidt, and Y. Nosyk. "High-quality two-nucleon potentials up to fifth order of the chiral expansion". In: *Phys. Rev. C* 96.2 (2017), 24004. DOI: 10.1103/PhysRevC.96.024004.

[Epe+19]   E. Epelbaum, J. Golak, K. Hebeler, et al. "Few- and many-nucleon systems with semilocal coordinate-space regularized chiral two- and three-body forces". In: *Phys. Rev. C* 99.2 (2019), 24313. DOI: 10.1103/PhysRevC.99.024313.

[EHM09]   E. Epelbaum, H.-W. Hammer, and U.-G. Meißner. "Modern theory of nuclear forces". In: *Rev. Mod. Phys.* 81.4 (2009), 1773–1825. DOI: 10.1103/RevModPhys.81.1773.

[Fos+17]   K. Fossez, J. Rotureau, N. Michel, et al. "Can Tetraneutron be a Narrow Resonance?" In: *Phys. Rev. Lett.* 119.3 (2017), 32501. DOI: 10.1103/PhysRevLett.119.032501.

[Fur12]   R. J. Furnstahl. "The Renormalization Group in Nuclear Physics". In: *Nuclear Physics B - Proceedings Supplements* 228.1 (2012), 139–175. DOI: 10.1016/j.nuclphysbps.2012.06.005.

[Gam28]   G. Gamow. "Zur Quantentheorie des Atomkernes". In: *Zeitschrift für Physik* 51.3 (1928), 204–212. DOI: 10.1007/BF01343196.

[GCR16]   E. Gebrerufael, A. Calci, and R. Roth. "Open-shell nuclei and excited states from multireference normal-ordered Hamiltonians". In: *Phys. Rev. C* 93.3 (2016), 31301. DOI: 10.1103/PhysRevC.93.031301.

[Geb+17]   E. Gebrerufael, K. Vobig, H. Hergert, et al. "Ab Initio Description of Open-Shell Nuclei: Merging No-Core Shell Model and In-Medium Similarity Renormalization Group". In: *Physical Review Letters* 118 (2017). DOI: 10.1103/PhysRevLett.118.152503.

[GV64]   I. M. Gelfand and N. Vilenkin. "Chapter I - The Kernel Theorem. Nuclear Spaces. Rigged Hilbert Space". In: *Applications of Harmonic Analysis*. Ed. by I. M. Gelfand and N. Vilenkin. Academic Press, 1964, 1–134. DOI: https://doi.org/10.1016/B978-1-4832-2974-4.50006-8.

[Gil+65]   L. Gilly, M. Jean, R. Meunier, et al. "Double charge exchange with negative pions search for tetraneutron". In: *Physics Letters* 19.4 (1965), 335–338. DOI: https://doi.org/10.1016/0031-9163(65)91012-7.

[Gor+89]   T. P. Gorringe, S. Ahmad, D. S. Armstrong, et al. "Search for the tetraneutron using the reaction 4He(pi-, pi+)4n". In: *Phys. Rev. C* 40.5 (1989), 2390–2393. DOI: 10.1103/PhysRevC.40.2390.

[Gre+20]   S. K. Greif, K. Hebeler, J. M. Lattimer, et al. "Equation of State Constraints from Nuclear Physics, Neutron Star Masses, and Future Moment of Inertia Measurements". In: *The Astrophysical Journal* 901.2 (2020), 155. DOI: 10.3847/1538-4357/abaf55.

[Gur+05]   Y. B. Gurov, M. N. Behr, D. V. Aleshkin, et al. "Spectroscopy of superheavy hydrogen isotopes 4H and 5H". In: *The European Physical Journal A - Hadrons and Nuclei* 24.2 (2005), 231–236. DOI: 10.1140/epja/i2004-10139-0.

[GV71]   B. Gyarmati and T. Vertse. "On the normalization of Gamow functions". In: *Nuclear Physics A* 160.3 (1971), 523–528. DOI: https://doi.org/10.1016/0375-9474(71)90095-9.

[Hag+07]   G. Hagen, D. J. Dean, M. Hjorth-Jensen, et al. "Complex coupled-cluster approach to an ab-initio description of open quantum systems". In: *Physics Letters B* 656.4 (2007), 169–173. DOI: https://doi.org/10.1016/j.physletb.2007.07.072.

[HHM06]   G. Hagen, M. Hjorth-Jensen, and N. Michel. "Gamow shell model and realistic nucleon-nucleon interactions". In: *Phys. Rev. C* 73.6 (2006), 64307. DOI: 10.1103/PhysRevC.73.064307.

[HKK20]   H.-W. Hammer, S. König, and U. van Kolck. "Nuclear effective field theory: Status and perspectives". In: *Rev. Mod. Phys.* 92.2 (2020), 25004. DOI: 10.1103/RevModPhys.92.025004.

[HK17a]   H.-W. Hammer and S. König. "General Aspects of Effective Field Theories and Few-Body Applications". In: *An Advanced Course in Computational Nuclear Physics: Bridging the Scales from Quarks to Neutron Stars*. Ed. by M. Hjorth-Jensen, M. P. Lombardo, and U. van Kolck. Cham: Springer International Publishing, 2017, 93–153. DOI: 10.1007/978-3-319-53336-0_4.

[HR09]   H. Hergert and R. Roth. "Treatment of the intrinsic Hamiltonian in particle-number nonconserving theories". In: *Physics Letters B* 682.1 (2009), 27–32. DOI: https://doi.org/10.1016/j.physletb.2009.10.100.

[Her17]   H. Hergert. "In-medium similarity renormalization group for closed and open-shell nuclei". In: *Physica Scripta* 92.2 (2017), 023002. DOI: 10.1088/1402-4896/92/2/023002.

[Her+13]   H. Hergert, S. K. Bogner, S. Binder, et al. "In-medium similarity renormalization group with chiral two-plus three-nucleon interactions". In: *Physical Review C - Nuclear Physics* (2013). DOI: 10.1103/PhysRevC.87.034307.

[HK12]   E. Hiyama and M. Kamimura. "Variational calculation of 4He tetramer ground and excited states using a realistic pair potential". In: *Phys. Rev. A* 85.2 (2012), 22502. DOI: 10.1103/PhysRevA.85.022502.

[Hiy+16]   E. Hiyama, R. Lazauskas, J. Carbonell, et al. "Possibility of generating a 4-neutron resonance with a T=3/2 isospin 3-neutron force". In: *Phys. Rev. C* 93.4 (2016), 44004. DOI: 10.1103/PhysRevC.93.044004.

[HK17b]   J. W. Holt and N. Kaiser. "Equation of state of nuclear and neutron matter at third-order in perturbation theory from chiral effective field theory". In: *Phys. Rev. C* 95.3 (2017), 34326. DOI: 10.1103/PhysRevC.95.034326.

[Hop+21]   J. Hoppe, A. Tichai, M. Heinz, et al. "Natural orbitals for many-body expansion methods". In: *Phys. Rev. C* 103.1 (2021), 14321. DOI: 10.1103/PhysRevC.103.014321.

[Hu+19]   B. S. Hu, Q. Wu, Z. H. Sun, et al. "Ab initio Gamow in-medium similarity renormalization group with resonance and continuum". In: *Phys. Rev. C* 99.6 (2019), 61302. DOI: 10.1103/PhysRevC.99.061302.

[HWS21]   S. Huth, C. Wellenhofer, and A. Schwenk. "New equations of state constrained by nuclear physics, observations, and QCD calculations of high-density nuclear matter". In: *Phys. Rev. C* 103.2 (2021), 25803. DOI: 10.1103/PhysRevC.103.025803.

[Hüt+20]   T. Hüther, K. Vobig, K. Hebeler, et al. "Family of chiral two- plus three-nucleon interactions for accurate nuclear structure studies". In: *Physics Letters B* 808 (2020), 135651. DOI: https://doi.org/10.1016/j.physletb.2020.135651.

[IÁA19]   O. Ivanytskyi, M. Ángeles Pérez-García, and C. Albertus. "Tetraneutron condensation in neutron rich matter". In: *The European Physical Journal A* 55.10 (2019), 184. DOI: 10.1140/epja/i2019-12900-6.

[Jän+96]   J. Jänecke, T. Annakkage, G. P. A. Berg, et al. "Structure of the neutron-halo nucleus 6He". In: *Phys. Rev. C* 54.3 (1996), 1070–1083. DOI: 10.1103/PhysRevC.54.1070.

[Kam88] M. Kamimura. "Nonadiabatic coupled-rearrangement-channel approach to muonic molecules". In: *Phys. Rev. A* 38.2 (1988), 621–624. DOI: `10.1103/PhysRevA.38.621`.

[Kis+16] K. Kisamori, S. Shimoura, H. Miya, et al. "Candidate Resonant Tetraneutron State Populated by the 4He(8He,8Be) Reaction". In: *Phys. Rev. Lett.* 116.5 (2016), 52501. DOI: `10.1103/PhysRevLett.116.052501`.

[Knö+23] M. Knöll, T. Wolfgruber, M. L. Agel, et al. "Machine learning for the prediction of converged energies from ab initio nuclear structure calculations". In: *Physics Letters B* 839 (2023), 137781. DOI: `https://doi.org/10.1016/j.physletb.2023.137781`.

[Kur+22] T. Kuroda, T. Fischer, T. Takiwaki, et al. "Core-collapse Supernova Simulations and the Formation of Neutron Stars, Hybrid Stars, and Black Holes". In: *The Astrophysical Journal* 924.1 (2022), 38. DOI: `10.3847/1538-4357/ac31a8`.

[Lan50] C. Lanczos. "An iteration method for the solution of the eigenvalue problem of linear differential and integral operators". In: *Journal of Research of the National Bureau of Standards* 45.4 (1950). DOI: `10.6028/jres.045.026`.

[LT58] A. M. Lane and R. G. Thomas. "R-Matrix Theory of Nuclear Reactions". In: *Rev. Mod. Phys.* 30.2 (1958), 257–353. DOI: `10.1103/RevModPhys.30.257`.

[Lan14] J. Langhammer. "Chiral Three-Nucleon Interactions in Ab-Initio Nuclear Structure and Reactions". PhD thesis. Darmstadt: Technische Universität, 2014.

[LP01] J. M. Lattimer and M. Prakash. "Neutron Star Structure and the Equation of State". In: *The Astrophysical Journal* 550.1 (2001), 426. DOI: `10.1086/319702`.

[LHC19] R. Lazauskas, E. Hiyama, and J. Carbonell. "Ab initio calculations of 5H resonant states". In: *Physics Letters B* 791 (2019), 335–341. DOI: `https://doi.org/10.1016/j.physletb.2019.02.047`.

[LC05] R. Lazauskas and J. Carbonell. "Is a physically observable tetraneutron resonance compatible with realistic nuclear interactions?" In: *Phys. Rev. C* 72.3 (2005), 34003. DOI: `10.1103/PhysRevC.72.034003`.

[LC20] R. Lazauskas and J. Carbonell. "Description of Four- and Five-Nucleon Systems by Solving Faddeev-Yakubovsky Equations in Configuration Space". In: *Frontiers in Physics* 7 (2020). DOI: `10.3389/fphy.2019.00251`.

[Li+19]   J. G. Li, N. Michel, B. S. Hu, et al. "Ab initio no-core Gamow shell-model cal-
          culations of multineutron systems". In: *Phys. Rev. C* 100.5 (2019), 54313. DOI:
          10.1103/PhysRevC.100.054313.

[Li+21]   J. G. Li, N. Michel, W. Zuo, et al. "Resonances of A=4 T=1 isospin triplet states
          within the ab initio no-core Gamow shell model". In: *Phys. Rev. C* 104.2 (2021),
          24319. DOI: 10.1103/PhysRevC.104.024319.

[Lin93]   P. Lind. "Completeness relations and resonant state expansions". In: *Phys. Rev. C*
          47.5 (1993), 1903–1920. DOI: 10.1103/PhysRevC.47.1903.

[LHL88]   F. Q. Liu, X. J. Hou, and T. K. Lim. "Faddeev-Yakubovsky theory for four-body
          systems with three-body forces and its one-dimensional integral equations from
          the hyperspherical-harmonics expansion in momentum space". In: *Few-Body
          Systems* 4.2 (1988), 89–101. DOI: 10.1007/BF01076331.

[Mac01]   R. Machleidt. "High-precision, charge-dependent Bonn nucleon-nucleon poten-
          tial". In: *Phys. Rev. C* 63.2 (2001), 24001. DOI: 10.1103/PhysRevC.63.024001.

[ME11]   R. Machleidt and D. R. Entem. "Chiral effective field theory and nuclear forces".
          In: *Physics Reports* 503.1 (2011), 1–75. DOI: 10.1016/j.physrep.2011.02.001.

[Man20]   A. Mann. "The golden age of neutron-star physics has arrived." In: *Nature*
          579.7797 (2020), 20–22. DOI: 10.1038/d41586-020-00590-8.

[MVS09]   P. Maris, J. P. Vary, and A. M. Shirokov. "Ab initio no-core full configuration
          calculations of light nuclei". In: *Phys. Rev. C* 79.1 (2009), 14308. DOI: 10.1103/
          PhysRevC.79.014308.

[Mar+21] P. Maris, E. Epelbaum, R. J. Furnstahl, et al. "Light nuclei with semilocal
          momentum-space regularized chiral interactions up to third order". In: *Physical
          Review C* 103.5 (2021), 54001. DOI: 10.1103/PhysRevC.103.054001.

[Mar+02] F. M. Marqués, M. Labiche, N. A. Orr, et al. "Detection of neutron clusters". In:
          Phys. Rev. C 65.4 (2002), 44006. DOI: 10.1103/PhysRevC.65.044006.

[MC21]   F. M. Marqués and J. Carbonell. "The quest for light multineutron systems". In:
          The European Physical Journal A 57.3 (2021), 105. DOI: 10.1140/epja/s10050-
          021-00417-8.

[Maz+17]   I. A. Mazur, A. M. Shirokov, A. I. Mazur, et al. "Description of resonant states in the shell model". In: *Physics of Particles and Nuclei* 48.1 (2017), 84–89. DOI: 10.1134/S1063779617010142.

[Mic+02]   N. Michel, W. Nazarewicz, M. Płoszajczak, et al. "Gamow Shell Model Description of Neutron-Rich Nuclei". In: *Phys. Rev. Lett.* 89.4 (2002), 42502. DOI: 10.1103/PhysRevLett.89.042502.

[Mic+03]   N. Michel, W. Nazarewicz, M. Płoszajczak, et al. "Gamow shell model description of weakly bound nuclei and unbound nuclear states". In: *Phys. Rev. C* 67.5 (2003), 54311. DOI: 10.1103/PhysRevC.67.054311.

[Mic+08]   N. Michel, W. Nazarewicz, M. Płoszajczak, et al. "Shell model in the complex energy plane". In: *Journal of Physics G: Nuclear and Particle Physics* 36.1 (2008), 13101. DOI: 10.1088/0954-3899/36/1/013101.

[Mou+12]   X. Mougeot, V. Lapoux, W. Mittig, et al. "New excited states in the halo nucleus 6He". In: *Physics Letters B* 718.2 (2012), 441–446. DOI: https://doi.org/10.1016/j.physletb.2012.10.054.

[Nav+16]   P. Navrátil, S. Quaglioni, G. Hupin, et al. "Unified ab initio approaches to nuclear structure and reactions". In: *Physica Scripta* 91.5 (2016), 53002. DOI: 10.1088/0031-8949/91/5/053002.

[Nav+09]   P. Navrátil, S. Quaglioni, I. Stetcu, et al. "Recent developments in no-core shell-model calculations". In: *Journal of Physics G: Nuclear and Particle Physics* 36.8 (2009), 83101. DOI: 10.1088/0954-3899/36/8/083101.

[NRQ10]   P. Navrátil, R. Roth, and S. Quaglioni. "Ab initio many-body calculations of nucleon scattering on 4He, 7Li, 7Be, 12C and 16O." In: *Phys. Rev. C* 82.3 (2010), 34609. DOI: 10.1103/PhysRevC.82.034609.

[Nov+20]   S. J. Novario, G. Hagen, G. R. Jansen, et al. "Charge radii of exotic neon and magnesium isotopes". In: *Phys. Rev. C* 102.5 (2020), 51303. DOI: 10.1103/PhysRevC.102.051303.

[Nov+12]   B. G. Novatsky, E. Y. Nikolsky, S. B. Sakuta, et al. "Possible observation of light neutron nuclei in the alpha-particle-induced fission of 238U". In: *JETP Letters* 96.5 (2012), 280–284. DOI: 10.1134/S0021364012170110.

[NSS14]   B. G. Novatsky, S. B. Sakuta, and D. N. Stepanov. "Detection of light neutron nuclei in the alpha-particle-induced fission of 238U by the activation method with 27Al". In: *JETP Letters* 98.11 (2014), 656–660. DOI: 10.1134/S002136401324017X.

[Nun+20]   F. M. Nunes, G. Potel, T. Poxon-Pearson, et al. "Nuclear Reactions in Astrophysics: A Review of Useful Probes for Extracting Reaction Rates". In: *Annual Review of Nuclear and Particle Science* 70.1 (2020), 147–170. DOI: 10.1146/annurev-nucl-020620-063734.

[OHS14]   T. Oishi, K. Hagino, and H. Sagawa. "Role of diproton correlation in two-proton-emission decay of the 6Be nucleus". In: *Phys. Rev. C* 90.3 (2014), 34303. DOI: 10.1103/PhysRevC.90.034303.

[Olv+22]   F. W. J. Olver, A. B. Olde Daalhuis, D. W. Lozier, et al. *NIST Digital Library of Mathematical Functions.* 2022. URL: http://dlmf.nist.gov/.

[Pap+13]   G. Papadimitriou, J. Rotureau, N. Michel, et al. "Ab initio no-core Gamow shell model calculations with realistic interactions". In: *Phys. Rev. C* 88.4 (2013), 44318. DOI: 10.1103/PhysRevC.88.044318.

[Pie03]   S. C. Pieper. "Can Modern Nuclear Hamiltonians Tolerate a Bound Tetraneutron?" In: *Phys. Rev. Lett.* 90.25 (2003), 252501. DOI: 10.1103/PhysRevLett.90.252501.

[Pie+01]   S. C. Pieper, V. R. Pandharipande, R. B. Wiringa, et al. "Realistic models of pion-exchange three-nucleon interactions". In: *Phys. Rev. C* 64.1 (2001), 14001. DOI: 10.1103/PhysRevC.64.014001.

[QN08]   S. Quaglioni and P. Navrátil. "Ab initio many-body calculations of n-3H, n-4He, p-(3,4)He, and n-10Be scattering". In: *Physical review letters* 101 (2008), 92501. DOI: 10.1103/PhysRevLett.101.092501.

[QN09]   S. Quaglioni and P. Navrátil. "Ab initio many-body calculations of nucleon-nucleus scattering". In: *Phys. Rev. C* 79.4 (2009), 44606. DOI: 10.1103/PhysRevC.79.044606.

[RKE18]   P. Reinert, H. Krebs, and E. Epelbaum. "Semilocal momentum-space regularized chiral two-nucleon potentials up to fifth order". In: *The European Physical Journal A* 54.5 (2018), 86. DOI: 10.1140/epja/i2018-12516-4.

[RS80]   P. Ring and P. Schuck. *The nuclear many-body problem.* 1st ed. Springer Berlin, Heidelberg, 1980.

[Rom+14]   C. Romero-Redondo, S. Quaglioni, P. Navrátil, et al. "4He+n+n Continuum within an Ab initio Framework". In: *Phys. Rev. Lett.* 113.3 (2014), 32503. DOI: 10.1103/PhysRevLett.113.032503.

[RRH08]   R. Roth, S. Reinhardt, and H. Hergert. "Unitary correlation operator method and similarity renormalization group: Connections and differences". In: *Physical Review C - Nuclear Physics* 77.6 (2008). DOI: 10.1103/PhysRevC.77.064003.

[Rot09]   R. Roth. "Importance truncation for large-scale configuration interaction approaches". In: *Physical Review C - Nuclear Physics* 79.6 (2009). DOI: 10.1103/PhysRevC.79.064324.

[RGP09]   R. Roth, J. R. Gour, and P. Piecuch. "Center-of-mass problem in truncated configuration interaction and coupled-cluster calculations". In: *Physics Letters B* 679.4 (2009), 334–339. DOI: https://doi.org/10.1016/j.physletb.2009.07.071.

[Rot+11]   R. Roth, J. Langhammer, A. Calci, et al. "Similarity-Transformed Chiral NN+3N Interactions for the Ab Initio Description of 12C and 16O". In: *Phys. Rev. Lett.* 107.7 (2011), 72501. DOI: 10.1103/PhysRevLett.107.072501.

[SV63]   J. P. Schiffer and R. Vandenbosch. "Search for a particle-stable tetra neutron". In: *Physics Letters* 5 (1963), 292–293. DOI: https://doi.org/10.1016/S0375-9601(63)96134-6.

[Shi+16a] A. M. Shirokov, G. Papadimitriou, A. I. Mazur, et al. "Prediction for a Four-Neutron Resonance". In: *Phys. Rev. Lett.* 117.18 (2016), 182502. DOI: 10.1103/PhysRevLett.117.182502.

[Shi+16b] A. M. Shirokov, A. I. Mazur, I. A. Mazur, et al. "Shell model states in the continuum". In: *Physical Review C* 94.6 (2016). DOI: 10.1103/PhysRevC.94.064320.

[Sid+04]   S. I. Sidorchuk, D. D. Bogdanov, A. S. Fomichev, et al. "Experimental study of 4H in the reactions 2H(t,p) and 3H(t,d)". In: *Physics Letters B* 594.1 (2004), 54–60. DOI: https://doi.org/10.1016/j.physletb.2004.05.007.

[Sie39]   A. J. F. Siegert. "On the Derivation of the Dispersion Formula for Nuclear Reactions". In: *Phys. Rev.* 56.8 (1939), 750–752. DOI: 10.1103/PhysRev.56.750.

[SO96]   A. Szabo and N. S. Ostlund. *Modern Quantum Chemistry: Introduction to Advanced Electronic Structure Theory*. Dover Publications, 1996, 480.

[TSV97]   N. Tanaka, Y. Suzuki, and K. Varga. "Exploration of resonances by analytic continuation in the coupling constant". In: *Phys. Rev. C* 56.1 (1997), 562–565. DOI: 10.1103/PhysRevC.56.562.

[Tic+18]   A. Tichai, E. Gebrerufael, K. Vobig, et al. "Open-shell nuclei from No-Core Shell Model with perturbative improvement". In: *Physics Letters B* 786 (2018), 448–452. DOI: https://doi.org/10.1016/j.physletb.2018.10.029.

[TMR19]   A. Tichai, J. Müller, and R. Roth. "Natural orbitals forab initiono-core shell model calculations". In: *Physical Review C* 99.034321 (2019). DOI: 10.1103/PhysRevC.99.034321.

[Til+02]   D. R. Tilley, C. M. Cheves, J. L. Godwin, et al. "Energy levels of light nuclei A=5, 6, 7". In: *Nuclear Physics A* 708.1 (2002), 3–163. DOI: https://doi.org/10.1016/S0375-9474(02)00597-3.

[TWH92]   D. R. Tilley, H. R. Weller, and G. M. Hale. "Energy levels of light nuclei A = 4". In: *Nuclear Physics A* 541.1 (1992), 1–104. DOI: https://doi.org/10.1016/0375-9474(92)90635-W.

[TWH87]   D. R. Tilley, H. R. Weller, and H. H. Hasan. "Energy levels of light nuclei A = 3". In: *Nuclear Physics A* 474.1 (1987), 1–60. DOI: https://doi.org/10.1016/0375-9474(87)90193-X.

[Tur+77]   A. Turkevich, J. R. Cadieux, J. Warren, et al. "Search for the production of particle-stable neutral nuclei at multi-GeV energies". In: *Physics Letters B* 72.2 (1977), 163–165. DOI: https://doi.org/10.1016/0370-2693(77)90691-8.

[Ung+84]   J. E. Ungar, R. D. McKeown, D. F. Geesaman, et al. "Search for the tetraneutron by the double-charge-exchange of negative pions". In: *Physics Letters B* 144.5 (1984), 333–336. DOI: https://doi.org/10.1016/0370-2693(84)91272-3.

[V I89]   J. H. V. I. Kukulin, V. M. Krasnopol'sky. *Theory of Resonances - Principles and Applications*. Springer Dordrecht, 1989, 347. DOI: https://doi.org/10.1007/978-94-015-7817-2.

[Var+09]   J. P. Vary, P. Maris, E. Ng, et al. "Ab initio nuclear structure – the large sparse matrix eigenvalue problem". In: *Journal of Physics: Conference Series* 180 (2009), 12083. DOI: 10.1088/1742-6596/180/1/012083.

[VP11]   S. Veerasamy and W. N. Polyzou. "Momentum-space Argonne V18 interaction". In: *Phys. Rev. C* 84.3 (2011), 34003. DOI: 10.1103/PhysRevC.84.034003.

[Vob20]   K. Vobig. "Electromagnetic Observables and Open-Shell Nuclei from the In-Medium No-Core Shell Model". PhD thesis. Darmstadt: Technische Universität, 2020. DOI: https://doi.org/10.25534/tuprints-00011375.

[Vol09]   A. Volya. "Time-dependent approach to the continuum shell model". In: *Phys. Rev. C* 79.4 (2009), 44308. DOI: 10.1103/PhysRevC.79.044308.

[WE47]   E. P. Wigner and L. Eisenbud. "Higher Angular Momenta and Long Range Interaction in Resonance Reactions". In: *Phys. Rev.* 72.1 (1947), 29–41. DOI: 10.1103/PhysRev.72.29.

[Wig46]   E. P. Wigner. "Resonance Reactions". In: *Phys. Rev.* 70.9-10 (1946), 606–618. DOI: 10.1103/PhysRev.70.606.

[WSS95]   R. B. Wiringa, V. G. J. Stoks, and R. Schiavilla. "Accurate nucleon-nucleon potential with charge-independence breaking". In: *Phys. Rev. C* 51.1 (1995), 38–51. DOI: 10.1103/PhysRevC.51.38.

[Yvo57]   J. Yvon. "Une méthode d'étude des corrélations dans les fluides quantiques en équilibre". In: *Nuclear Physics* 4 (1957), 1–20. DOI: https://doi.org/10.1016/0029-5582(87)90002-2.

ERKLÄRUNGEN LAUT PROMOTIONSORDNUNG

§8 Abs. 1 lit. c PromO

Ich versichere hiermit, dass die elektronische Version meiner Dissertation mit der schriftlichen Version übereinstimmt.

§8 Abs. 1 lit. d PromO

Ich versichere hiermit, dass zu einem vorherigen Zeitpunkt noch keine Promotion versucht wurde. In diesem Fall sind nähere Angaben über Zeitpunkt, Hochschule, Dissertationsthema und Ergebnis dieses Versuchs mitzuteilen.

§9 Abs. 1 PromO

Ich versichere hiermit, dass die vorliegende Dissertation selbstständig und nur unter Verwendung der angegebenen Quellen verfasst wurde.

§ Abs. 2 PromO

Die Arbeit hat bisher noch nicht zu Prüfungszwecken gedient.

Darmstadt, den 24.01.2023

Julius Müller

DANKSAGUNG

Es gibt viele Menschen, die zur erfolgreichen Beendigung meines Studiums, der darauf folgenden Promotion und der finalen Anfertigung dieser Arbeit beigetragen haben und ich möchte mich bei alle diesen Menschen herzlich bedanken.

Bei meiner Freundin, Christina Xanthopoulou, bedanke ich mich für die Unterstützung und Motivation in den letzten und durch die Coronapandemie sehr anspruchsvollen und nervenzehrenden Jahren. Ohne sie an meiner Seite würde diese Arbeit nicht mit diesem Inhalt und zu diesem Zeitpunkt niedergeschrieben sein.

Ein besonderer Dank gilt meinem Doktorvater Prof. Robert Roth, der mich nicht nur während der Promotion sondern auch schon die Jahre zuvor seit dem dritten Semester meines Studiums begleitet hat. Er gab mir die Möglichkeit seiner Arbeitsgruppe im Rahmen meiner Bachelor- und Masterarbeit beizutreten und motivierte mich zur anschließenden Promotion und diese Arbeit. Auch er hat mich aus einigen Motivationstiefs hervorgeholt und stand mir mit seinem Wissen, seinen Ideen und seinen Vorschlägen immer zur Seite.

Bei Prof. Hans-Werner Hammer möchte ich mich für die Übernahme des Zweitgutachtens bedanken. Ich bedanke mich auch für unsere Diskussionen im Zuge der PhD Committee Meetings, durch die viele wertvolle Erkenntnisse entstanden sind.

Meinen ehemaligen Arbeitskollegen Alexander Tichai, Stefan Schulz, Christina Stumpf, Roland Wirth, Klaus Vobig, Stefan Alexa, Thomas Hüther und Tobias Mongelli danke ich für die Zusammenarbeit und die gemeinsamen Diskussionen vor allem zu Beginn meiner Laufbahn in der Arbeitsgruppe. Roland Wirth und Klaus Vobig danke ich besonderns für ihr Durchhaltevermögen in unzähligen Spät- und Nachtschichten im Büro.

Meinen aktuellen Arbeitskollgen, Marco Knöll, Tobias Wolfgruber, Laura Mertes, Lisa

LEBENSLAUF

Bildungsweg

2002-2006	**Grundschule,** Freiherr-vom-Stein Schule, Hünfelden
2006-2010	**Gymnasium,** Tilemannschule, Limburg an der Lahn
2010-2014	**Gymnasium,** Heinrich-von-Gagern Gymnasium, Frankfurt am Main
2014-2017	**Bachelorstudium Physik,** TU Darmstadt, Darmstadt
2017-2019	**Masterstudium Physik,** TU Darmstadt, Darmstadt
2019-2023	**Promotionsstudium Physik,** TU Darmstadt, Darmstadt